

Abstract

Topological defects predicted by extensions of general relativity can manifest in gravitational-wave observations on Earth. Future broadband gravitational-wave observations show promise of constraining such models. Analytical models can in the ultimate consequence access certain parameter spaces and dynamical ranges that are prohibitively expensive to simulate.

As a toy example, we present symmetron domain walls formed at redshift ~ 2 (around ten billion years ago) with structural ripples and investigate how gravitational radiation carries information about the symmetry-breaking theory. We derive the dynamics in the thin-wall limit from the Nambu–Goto action, and analytically solve the equation of motion for a small perturbation to planar walls *during* phase transition, when the surface energy density is time-dependent. These results are compared to the full field theory with deterministic simulations.

We find good qualitative correspondence between the thin-wall approximation and cosmological simulations. The wall positions from the two theories have average difference $\sim 7\%$ of initial perturbation magnitude when this is $\lesssim 10\%$ of the simulation box size. Lack of analytical summary statistics for the prototype makes comparative gravitational-wave analyses complicated, but we provide a superficial presentation of the results and discuss specifics of potential ways forward.

We present a protocol for reducing scalar-field oscillations to perform controlled toy-model simulations.

Contents

Acknowledgements	xi
Notation	xiii
1 Introduction	1
1.1 Physics overview	3
1.1.1 Key literature	3
1.2 Preliminaries	4
1.2.1 Special relativity	4
1.2.2 Classical field theory	4
1.2.3 Mathematical tools	5
1.2.4 Cosmic scales	5
1.2.5 Cosmological simulations	6
 I Background	 7
2 General Relativity	9
2.1 Differential geometry	9
2.1.1 Hypersurfaces	10
2.1.2 Conformal geometry	11
2.2 Einstein's equation	12
2.2.1 Energy–momentum tensor	12
2.2.2 Linearised gravity	13
2.3 Modern cosmology	13
2.3.1 Cosmological perturbation theory	15
2.4 Gravitational waves	15
2.4.1 Expanding universe	16
3 Symmetry-Breaking Dark Energy	19
3.1 Cosmological defects	19
3.1.1 The stationary \mathbb{Z}_2 kink	20
3.1.2 Domain walls	21
3.1.3 Defect formation	21
3.2 Scalar-field theories	22
3.2.1 General framework	22
3.2.2 Asymmetron model	23

II Methodology	27
4 Imperfect Defects	29
4.1 Formal treatment of defect dynamics	29
4.1.1 Linearised perturbations	31
4.1.2 Energy and momentum	31
4.2 Domain-wall dynamics.	31
4.2.1 Planar walls in expanding spacetime	32
4.2.2 Time-dependent surface tension.	33
4.3 Symmetron walls.	33
4.3.1 Solution in matter-dominated universe	33
4.4 From domain wall wiggles to spacetime ripples	36
4.4.1 Gravitational waves in expanding universe	36
4.4.2 Fourier-space stress–energy tensor	36
5 Cosmic Phase Transitions	39
5.1 \mathbb{Z}_2 -symmetry breaking.	39
5.1.1 Quasi-static limit	40
5.1.2 Asymptotic limit	40
5.2 Dynamic modelling	41
5.2.1 Equations	41
5.3 Pilot design	42
5.3.1 Initial configuration	42
5.3.2 Energy and momentum	43
5.3.3 Ripples in matter-dominated spacetime	44
5.3.4 Code output and interpretation	45
5.4 Simulation setups	45
5.4.1 Toy-model catalogue	46
III Findings	49
6 Pilot Testing	51
6.1 Symmetron field	51
6.1.1 Review	53
6.2 Domain-wall dynamics.	54
6.2.1 Review	56
6.3 Gravitational waves	56
6.3.1 Gravitational radiation	57
6.3.2 Comparison with analytical results	57
6.3.3 Review	59
6.4 Hindsight.	61
7 In-Depth Analysis	63
7.1 Project reflection	63
7.2 Continued assessment	64
7.2.1 Inter-wall force	64
7.2.2 Gravitational waves.	64
7.2.3 Supplementary experiments	65
7.3 Limitations and possibilities	66
7.3.1 Improvements.	66
7.4 Open questions	68

Summary	69
8 Conclusion and Outlook	71
Bibliography	75
Appendices	77
A Cylinder Functions	79
A.1 Explicit formulas	80
A.1.1 Integer order	80
A.1.2 Half-integer order	80
A.2 Properties	80
A.2.1 Some notable identities	80
A.2.2 Asymptotic behaviour	81
B Stable Symmetron	83
B.1 Idealised path	83
B.2 Field initialisation	85
C Symmetron Walls in Expanding Spacetime	87
C.1 Surface tension	87
C.1.1 Adjusting the limits	88
C.2 Wall dynamics	88
C.2.1 Full solution	89
C.3 Stress-energy tensor	89
C.3.1 Fourier-space SE tensor	90
C.3.2 Spin-2 projection	90
C.4 Stress-energy tensor: alternative scenarios	91
C.4.1 Cosine case	91
C.4.2 General case	91
D Miscellanea	93
D.1 Simulation 6	93
D.2 On the continuous/discrete Fourier-comparison	94

Contents

List of Figures

1.1	Sensitivity curves for present and future gravitational-wave experiments, created with gwplotter.com (Nov. 2024). The black curves represent the sensitivity curves for present detectors European Pulsar Timing Arrays (EPTA), Laser Interferometer Gravitational-wave Observatory (LIGO) and Advanced LIGO O1 (aLIGO (O1)), and future detectors Square Kilometer Array (SKA), evolving Laser Interferometer Space Antenna (eLISA), Decihertz Interferometer Gravitational-wave Observatory (DECIGO), aLIGO design (aLIGO), Einstein Telescope (ET) and Cosmic Explorer (CE).	1
3.1	Demonstration of the \mathbb{Z}_2 kink and its energy content for $\eta = 1$ and $\lambda = 2$. The green dotted graph is a Gaussian around $x = x_0$ with standard deviation $w/\sqrt{2}$. Inspiration from Vachaspati [54].	21
3.2	The evolution of the (a)symmetron effective potential in (dashed red) solid blue. <i>Panel I</i> : The potential before SSB, <i>panel II</i> : at SSB, and <i>panels III–VI</i> : after SSB, with diluting density.	24
3.3	Schematic of the symmetron screening mechanism. It is clear that the vacuum expectation value goes to zero in dense regions. This example assumes a symmetron with Compton length scale $L_c \sim \mathcal{O}(\text{kpc})$ [10]. Illustration based on Christiansen [13].	25
4.1	Demonstration of how the analytical solution to the equation of motion for $\varepsilon(s)$ was obtained. The numerical solution is included, both in the case with constant (“naive”) and time-varying (numerical) surface tension.	35
5.1	Demonstration of the periodicity of $\chi(a_i, z)$ on the lattice. The shaded region represents the box coordinates.	43
5.2	Visual representation of initial configurations listed in Table 5.1.	47
6.1	The evolution of the symmetron field in the asymptotic limit. The symmetron parameters are the fiducial ones. The simulation results are from the simulation with no walls. We see χ_+ in solid grey, $\check{\chi} _{\text{opt.}}$ in solid blue, $\langle \check{\chi} \rangle$ in solid red and $\check{\chi}^{\text{ideal}}$ in dashed yellow.	51
6.2	Background quantities as functions of scale factor a for different simulations. We show the maximum and box-averaged values of the symmetron field χ and its derivative $q = a^2 \dot{\chi}$	52
6.3	The asymptotic symmetron field $\check{\chi}$ and its time derivative $\dot{\check{\chi}}$	53
6.4	Demonstration of the interpretation of the results from simulation 1.	54

List of Figures

6.5	Functions of the scaled time parameter $t_\omega = \omega(s-1) = p(\tau - \tau_*)$. <i>Top panel:</i> The wall extremal position normalised to the initial amplitude, $e = \varepsilon/\varepsilon_*$. <i>Bottom panel:</i> The absolute difference between the wall position from calculations and simulations, $\Delta e = \varepsilon^{\text{NG}} - \varepsilon^\phi /\varepsilon_*$	55
6.6	The box-averaged gravitational-wave radiation, normalised to the critical density today. Note the logarithmic y -axes. <i>Left panel:</i> ρ_{gw} as function of $s = \tau/\tau_*$. <i>Right panel:</i> ρ_{gw} as function of $t_\omega = \omega(s-1) = p(\tau - \tau_*)$	57
6.7	Monochromatic plus-waves evolving over conformal time $s = \tau/\tau_*$, normalised to unity ($h_+ / \max h_+ $). The upper-left/lower-right panel is explanatory for all panels: Green dash-dotted graphs represent \tilde{h}_+^{NG} , orange solid ones represent \tilde{h}_+^ϕ and in blue are \tilde{h}_+ . The wave vector is given in the lower left corner of each plot, as (v, w) . The secondary above x -axis represents scaled time $t_\omega = p(\tau - \tau_*)$	59
6.8	The strain squared $\tilde{h}^2 = 2\tilde{h}_+^2$ as functions of angle ϑ , normalised to unity; $\tilde{h}^2 / \max \tilde{h}^2$. Green dash-dotted graphs represent \tilde{h}_+^{NG} , orange solid ones represent \tilde{h}_+^ϕ and in blue are \tilde{h}_+	60
B.1	The asymptotic symmetron field $\check{\chi}$ and the derivative $\check{q} = a^2 \dot{\check{\chi}}$ with different initial conditions. The horizontal axis is $\chi_+ = \sqrt{1-v}$. The thin, solid lines show the solutions with initial conditions used in simulations (χ_+ and $q_+ = a^2 \dot{\chi}_+$) and the dashed lines show solutions with optimised initial conditions ($\check{\chi}^{\text{ideal}}$ and $\check{q}^{\text{ideal}} = a^2 \dot{\check{\chi}}^{\text{ideal}}$)	84
D.1	Simulation results from simulations 1, 7 and 6, as functions of scale factor a . <i>Top panel:</i> The wall position ε^ϕ . <i>Bottom panels:</i> Spatially averaged values of the scalar fields χ and $q = a^2 \dot{\chi}$	93

List of Tables

2.1	Perfect-fluid description of various phenomena. The last column shows the corresponding topological defect, which will be introduced in Section 3.1 . . .	14
5.1	Details about simulations addressed in Part III. Each simulation is labelled 0–7. See Sections 5.3 and 5.4 for description of parameters.	47
A.1	Types of Bessel functions and conventions. Here, $\nu \in \mathbb{C}$ and $n \in \mathbb{Z}$ are constants, and $x \in \mathbb{C}$ is a variable. Linear combinations of the first and second kinds are denoted in the second column. Subscripts mean order, and parenthesised superscripts refer to kind.	79

List of Tables

Acknowledgements

I would like to give thanks to my extraordinary group of supervisors, David Mota, Øyvind Christiansen, Farbod Hassani and Julian Adamek, for guidance and support. I am grateful to the cosmology group at the Institute for Theoretical Astrophysics (ITA) for helpful discussion. Special thanks to ITA's own Morsal Saba, for being the person everyone can go to about anything.

This would not have been possible without the love, support and food from my generous family. Special thanks to my dear father for always believing in me, and to my loving mother for her help and guidance. And to all the roommates I have had during these years, I am thankful for your patience with me.

Words cannot express my gratitude to my study mates for our friendship and sense of community.

Lars the Loyal Coffee Maker—who has never failed me—deserves my gratitude as well. I guess a thank you also to *Ringnes AS* is in order. Lastly, I would like to recognise the radio channel *NRK Nyheter* for consistently reminding me that the world is bigger than this Master's thesis.

Acknowledgements

Notation

Constants and units

We use natural units where the speed of light in vacuum is $c = 1$ and the reduced Planck mass is $M_{\text{Pl}} = 1/\sqrt{8\pi G_N} = 1$. Here, G_N is the Newtonian constant of gravitation. Comoving lengths are usually given in units of megaparsec per reduced Hubble constant Mpc/h, where $1 \text{ pc} = 3.261566$ light-years. The critical density today is $\rho_{\text{cr}0} = 3H_0^2M_{\text{Pl}}^2$, where the Hubble constant is $H_0 = (2997.9 \text{ Mpc/h})^{-1}$ in these units.

Fiducial cosmology. We follow Dodelson & Schmidt [21] for the fiducial cosmological parameters:

$$h = 0.677, \quad \Omega_{m0} = 0.311, \quad \Omega_{\Lambda0} = 1 - \Omega_{m0} = 0.689, \quad (1)$$

where h is the reduced Hubble parameter, and $\Omega_{m0,\Lambda0}$ are the matter and cosmological-constant present-day energy parameters, respectively.

Tensors

We use the convention that tensors in the text are identified by their components in the normal coordinate basis, e.g. T^μ_ν refers to the tensor $T = T^\mu_\nu \partial_\mu \otimes dx^\nu$. For convenience, we will often use equality between a tensor and its corresponding matrix or vector representation, e.g. $x^\mu = (t, x, y, z)$.

Indices. Greek indices run from 0 to N , and Latin i, j, k, \dots from 1 to N , in an $(N + 1)$ -dimensional spacetime. Indices a, b, c are reserved for auxiliary coordinate systems. We adopt Einstein's summing convention in which repeated indices are summed over, e.g. $x^\mu x_\mu = \sum_{\mu=0}^N x^\mu x_\mu$.

Metric. The metric signature $(-, +, \dots, +)$ is considered. The Minkowski metric is denoted $\eta_{\mu\nu} \equiv \text{diag}(-1, +1, \dots, +1)$, whereas a general metric is denoted $g_{\mu\nu}$. The metric raises and lowers indices of tensors, e.g. $x^\mu = g^{\mu\nu}x_\nu$. We let g denote the determinant of the metric, $g \equiv \det(g_{\mu\nu})$.

Derivatives. We sometimes adopt the comma-notation for partial derivatives ∂_μ and covariant derivatives ∇_μ . For a scalar ϕ , we have:

$$\phi_{,\mu} \equiv \partial_\mu \phi = \frac{\partial \phi}{\partial x^\mu} = (\partial_0, \partial_i), \quad (2a)$$

$$\phi_{;\mu} \equiv \nabla_\mu \phi = \partial_\mu \phi. \quad (2b)$$

Notation

The covariant derivative of a general rank- (k, l) tensor $T^{\rho_1 \dots \rho_k}_{\sigma_1 \dots \sigma_l}$ is

$$\nabla_\mu T^{\rho_1 \dots \rho_k}_{\sigma_1 \dots \sigma_l} = \partial_\mu T^{\rho_1 \dots \rho_k}_{\sigma_1 \dots \sigma_l} + \Gamma_{\mu\nu}^{\rho_1} T^{\nu\rho_2 \dots \rho_k}_{\sigma_1 \dots \sigma_l} + \dots - \Gamma_{\mu\sigma_1}^\nu T^{\rho_1 \dots \rho_k}_{\nu\sigma_2 \dots \sigma_l} + \dots, \quad (3)$$

where $\Gamma_{\mu\nu}^\rho$ are the Christoffel symbols in Eq. (8). The d'Alembertian reads

$$\square = \nabla^\mu \nabla_\mu = \frac{1}{\sqrt{-g}} \partial_\mu (\sqrt{-g} \partial^\mu), \quad (4)$$

and we use $\square_M \equiv \partial^\mu \partial_\mu$ to specify the Minkowski box operator.

Miscellaneous. We make use of the notation

$$T_{(\mu\nu)} \equiv \frac{1}{2} (T_{\mu\nu} + T_{\nu\mu}), \quad (5a)$$

$$T_{[\mu\nu]} \equiv \frac{1}{2} (T_{\mu\nu} - T_{\nu\mu}). \quad (5b)$$

Thus, $T_{\mu\nu} = T_{(\mu\nu)} + T_{[\mu\nu]}$.

Special symbols and tensors. The Kronecker delta is defined as

$$\delta_{ij} = \begin{cases} 1 & \text{if } i = j, \\ 0 & \text{else,} \end{cases} \quad (6)$$

and the Levi-Civita symbol is

$$\epsilon_{i_1 i_2 \dots i_n} = \begin{cases} +1 & \text{if } (i_1 i_2 \dots i_n) \text{ is an even permutation of } (12 \dots n) \\ -1 & \text{if } (i_1 i_2 \dots i_n) \text{ is an odd permutation of } (12 \dots n) \\ 0 & \text{else,} \end{cases} \quad (7)$$

in n dimensions. The Christoffel symbols (also called connection coefficients) are given by

$$\Gamma_{\mu\nu}^\rho = \frac{1}{2} g^{\rho\sigma} (g_{\mu\sigma,\nu} + g_{\mu\sigma,\nu} - g_{\mu\nu,\sigma}), \quad (8)$$

where $g_{\mu\nu}$ is the spacetime metric. The Riemann curvature tensor is

$$\mathcal{R}_{\sigma\mu\nu}^\rho = \partial_\mu \Gamma_{\nu\sigma}^\rho - \partial_\nu \Gamma_{\mu\sigma}^\rho + \Gamma_{\mu\lambda}^\rho \Gamma_{\nu\sigma}^\lambda - \Gamma_{\nu\lambda}^\rho \Gamma_{\mu\sigma}^\lambda. \quad (9)$$

We express the *Lambda tensor*—sometimes called the “projection operator” or “spin-2 projector”—that projects a symmetric tensor onto the TT gauge as

$$\Lambda_{ij}^{kl}(\mathbf{k}) = P_i^k(\mathbf{k}) P_j^l(\mathbf{k}) - \frac{1}{2} P_{ij}(\mathbf{k}) P^{kl}(\mathbf{k}); \quad P_{ij}(\mathbf{k}) = \delta_{ij} - k_i k_j / k^2, \quad (10)$$

where \mathbf{k} is the propagation direction (see Section 2.4).

Fourier transforms

We use the following convention for the continuous Fourier transform of $f(\mathbf{x})$, $\tilde{f}(\mathbf{k})$, and its inverse, where \mathbf{x} and \mathbf{k} are three-vectors:

$$\begin{aligned} \tilde{f}(\mathbf{k}) &= \int_{\mathbf{k}} \mathcal{F}\{f(\mathbf{x})\} = \int d^3x e^{i\mathbf{k}\cdot\mathbf{x}} f(\mathbf{x}), \\ f(\mathbf{x}) &= \mathcal{F}_x^{-1}\{\tilde{f}(\mathbf{k})\} = \int \frac{d^3k}{(2\pi)^3} e^{-i\mathbf{k}\cdot\mathbf{x}} \tilde{f}(\mathbf{k}). \end{aligned} \quad (11)$$

Note that this gives $\partial_i \leftrightarrow +ik_i$.

Special functions

We denote linear combinations of the first and second kind of regular Bessel, spherical Bessel and Riccati–Bessel functions by Z , z and R , respectively. More details are found in Appendix A.

Basic mathematical language

We use \equiv for global definitions and \triangleq for temporary placeholders. With $dy/dx \supset f(x)$ is meant that $f(x)$ is a term in the first derivative of y . We will encounter the shorthand notation $\llbracket n \in \mathbb{Z} \rrbracket \equiv \sum_{m \in \mathbb{Z}} \delta(n - m)$, where n is dimensionless.

Acronyms

CDM	cold dark matter
CMB	cosmic microwave background [radiation]
CP	cosmological principle
DFT	discrete Fourier transform
F(L)RW	Friedmann(–Lemaître)–Robertson–Walker [metric]
GR	general relativity
GWB	[stochastic] gravitational wave background
HPC	high performance computing
MPI	Message Passing Interface
ODE	ordinary differential equation
PDE	partial differential equation
PTA	pulsar timing array
SE	stress–energy [tensor]
SR	special relativity
(S)SB	(spontaneous) symmetry breaking
TT	transverse-traceless [gauge]
VEV	vacuum expectation value
Λ CDM	Lambda (Λ) cold dark matter model

Notation

Chapter 1

Introduction

From the first gravitational-wave observation by the ground-based Laser Interferometer Gravitational-wave Observatory (LIGO) in 2015 [1], and until the detection of stochastic nHz-frequency gravitational waves by the North American Nanohertz Observatory for Gravitational Waves (NANOGrav) released in 2023 [5], astrophysical sources have been the primary focus of the community [40]. The latter pulsar timing array (PTA) data (called *NANOGrav 15 yr*) allows for cosmological scales, and together with other planned gravitational-wave experiments has the potential of probing new physics. Figure 1.1 illustrates relations between detector sensitivities, bandwidths and gravitational sources.

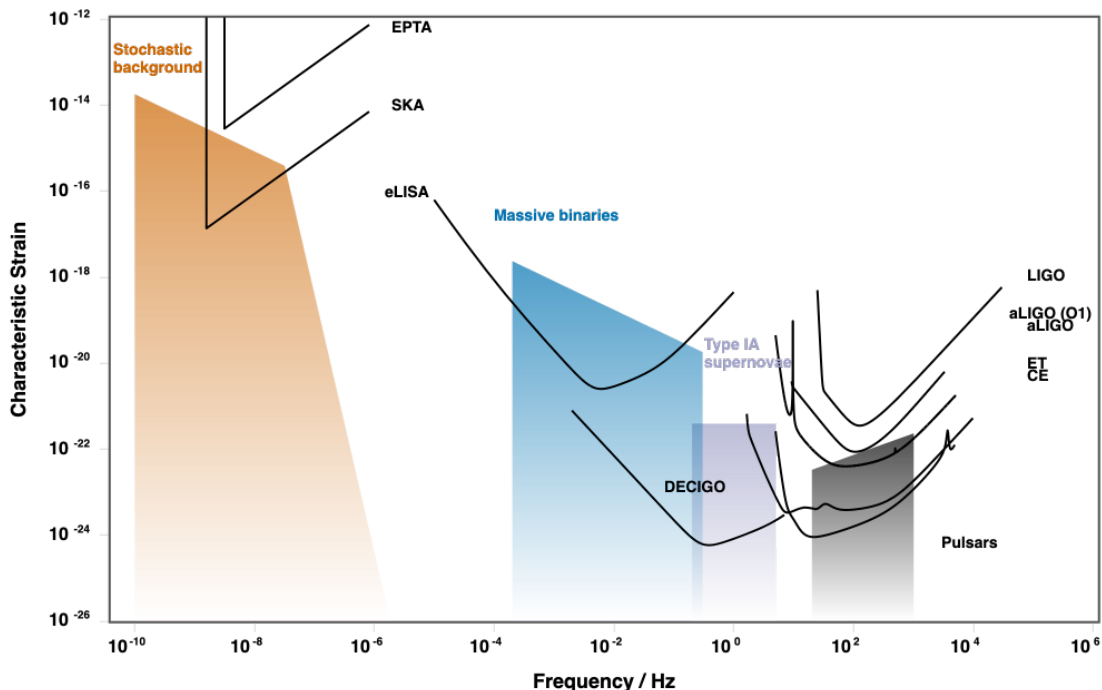


Figure 1.1: Sensitivity curves for present and future gravitational-wave experiments, created with gwplotter.com (Nov. 2024). The black curves represent the sensitivity curves for present detectors European Pulsar Timing Arrays (EPTA), Laser Interferometer Gravitational-wave Observatory (LIGO) and Advanced LIGO O1 (aLIGO (O1)), and future detectors Square Kilometer Array (SKA), evolving Laser Interferometer Space Antenna (eLISA), Deci-hertz Interferometer Gravitational-wave Observatory (DECIGO), aLIGO design (aLIGO), Einstein Telescope (ET) and Cosmic Explorer (CE).

Speculative topological defects in cosmology are generally remnants of phase transitions and

potential sources of gravitational waves [14, 52]. Dynamical ranges of cosmological simulations are limited, so resolving broad-frequency gravitational-wave spectra computationally is challenging [52]. This calls for novel analytical analyses of dynamics and gravitational-wave signals of candidate sources of a stochastic gravitational wave background (GWB). This search for cosmological gravitational waves can have great implications for both high-energy physics and cosmology alike, and can help constrain beyond-standard model particle-physics models [36].

Nanohertz frequencies today correspond to the horizon size in the early, very hot¹ universe [14]. Therefore, high-energy phase transitions, argued to manifest in these frequencies, has been the interest of recent studies [7, 32, 40, 52]. It is claimed [4] that *NANOGrav 15 yr* [5] can constrain for example domain-wall models. Babichev et al. [7] show that gravitational waves from melting domain walls—walls with time-dependent surface tension—show characteristics consistent with *NANOGrav 15 yr* [5].

Cosmic phase transitions creating or destructing topological defects are believed to produce gravitational waves [23, 32, 45]. Recent works [17, 23, 32, 33, 44, 46] show that domain walls can produce gravitational signals detectable in present and future gravitational-wave experiments. Amongst the phenomena studied by the community are colliding [8, 9, 38], collapsing [12, 27, 32, 49], and perturbed [6, 34] domain walls (and networks), many in context with gravitational waves.

To this end, we will focus on theoretical aspects of domain-wall formation in late-time phase transitions following Christiansen et al. [14, 16]. Cosmic domain walls are defects predicted by discrete symmetry-breaking scalar-field theories such as the symmetron model [31]. Their dynamics are well-understood in idealised scenarios [8, 26, 28, 34, 54], but self-contained, rigorous analytical frameworks connecting properties of topological defects and gravitational waves are lacking [52]. One of the aims of this thesis is to test the limits of the analytical solvability of such toy scenarios and discuss its potential as substitute for computationally expensive simulations.

We will use mathematical tools such as topology and geometry, and physical concepts like general relativity and cosmology, to study the dynamics of topological defects and to compute tensor perturbations sourced by infinitely thin, planar domain walls. We look at defects in expanding spacetime when the surface energy density is increasing. Similar works [8, 26, 34] explore the thin-wall approximation when the energy density is constant, best understood in Minkowski space. Extensions to thick walls have also been considered [18].

This work concludes in a framework that describes the motion of a small perturbation to the normal coordinate of a planar domain wall in a matter-dominated universe, with possibility for generalisation. The model assumes the symmetron potential, but this is easily changed to another scalar field model with discrete symmetry by changing the surface tension. We test the equations by comparison to toy scenarios in cosmological simulations using the `gevolution`-based [2] code `AsGRD` [14]. The final part—the resulting tensor perturbations to the metric—has room for improvement, or at least needs to be better tested against simulations. The pattern detected in simulations do resemble that of the analytical model, but there are discrepancies that we investigate in this thesis.

Thesis outline. The thesis is divided into three main parts. Part I presents the relevant background theory, including concepts from differential geometry and topological defects. In Part II we describe how the framework was designed and the way it is to be tested in simulations. Finally, in Part III we present the results from simulations and calculations, with comparisons and discussions.

¹Temperatures of order $\mathcal{O}(10^{12} \text{ K})$.

We give a brief summary and some concluding remarks in Chapter 8. In addition, we describe some basic concepts in the coming sections.

1.1 Physics overview

General relativity (GR) is a fundamental theory of gravitation proposed by Albert Einstein (1879–1955) in 1915. It describes gravity not as a force, but as a curvature of spacetime caused by mass and energy, fundamentally altering our understanding of both space and time. The theory is supported by numerous experiments and observations, such as the bending of light around massive objects (gravitational lensing) and the precise orbit of Mercury. Additionally, GR is essential for the accurate functioning of the Global Navigation Satellite System (GNSS), as it allows for the necessary corrections to account for the differences in the passage of time between satellites in orbit and receivers on Earth. Special relativity (SR)—proposed by the same physicist in 1905—is understood as a special case of GR where the background spacetime is Minkowski.

In cosmology, GR forms the backbone of our understanding of the universe on large scales. The theory predicts the expanding universe, which has been confirmed by the redshift observations of distant galaxies, leading to the development of the Big-Bang theory. GR also accounts for the formation of large-scale structures like galaxies and galaxy clusters, and provides the framework for understanding cosmic phenomena such as black holes and gravitational waves. The solutions to Einstein’s field equations under various conditions have led to a rich set of predictions and observations, including the cosmic microwave background radiation (CMB), which is a relic from the early universe and a critical piece of evidence supporting the Big Bang model.

The standard model of cosmology is called *Lambda cold dark matter* (Λ CDM). It postulates the existence of a cosmological constant (Λ), widely used synonymously with dark energy, and cold dark matter (CDM). Dark energy is used to explain the contemporary accelerated expansion of the universe, whereas dark matter accounts for the observed increased gravitational effects that ordinary matter alone cannot elucidate.

Besides the explanation of dark matter and dark energy, there are other shortcomings to these theories. Of most cosmological relevance are the smallness (“vacuum catastrophe”) and coincidence problems associated with the cosmological constant, as well as the Hubble tension (addressed in Section 2.3).

Amongst the more popular strategies scientists use to overcome the problems of modern cosmology, is to add extra degrees of freedom. Speculative scalar fields that possess certain symmetries tend to predict phase transitions, which in turn can produce topological defects such as domain walls. Domain walls are two-dimensional defects separating three-dimensional vacua, and they occur not only in cosmology, but also in particle physics, condensed-matter physics and every-day life.

1.1.1 Key literature

Let us mention a few foundational works that have been instrumental in shaping the theoretical and methodological approach in this project. *Spacetime and Geometry* by Carroll (2019) is the baseline for the majority of the differential-geometry analyses and GR discussions. A large part of the gravitational-wave discussion is inspired by *Gravitational Waves* volumes 1 and 2 by Maggiore (2007, 2018). *Kinks and Domain Walls* by Vachaspati (2006) provide the basis for our understanding of topological defects.

There are interesting quantum aspects to both gravitational waves and symmetry breaking that we will not cover here. We refer the interested reader to Peskin & Schroeder [48, Chapters 11, 12, 20 & 22] for quantum treatment of phase transitions with concepts such as effective potential, Higgs mechanism and quantum corrections. For a full field-theoretical approach to gravitons, see Maggiore [42, Chapter 2], and see Feynman [24] for the quantum field-theoretical formulation of gravitation.

1.2 Preliminaries

We assume that the reader is familiar with basic concepts from mathematical methods in physics such as the variational principle, tensors, Green's functions and cylindrical functions. Classical field theory and linear perturbation theory will not be covered from ground level. Other than this, the thesis will be relatively self-contained, but understanding of basic modern cosmology will be an advantage. For reference, we cover a few of these concepts in the subsections below.

1.2.1 Special relativity

The **four-vector** $x^\mu = (t, \mathbf{x})$ in Minkowski space $\mathbb{R}^{3,1}$ encompasses time $t = x^0$ and position $\mathbf{x} = x^i = (x^1, x^2, x^3)$. The metric tensor (defined in Section 2.1) in SR is $g_{\mu\nu} = \eta_{\mu\nu} \equiv \text{diag}(-1, +1, +1, +1)$. The four-vector x^μ is “naturally raised,” whereas the derivative

$$\partial_\mu \equiv \frac{\partial}{\partial x^\mu} = \left(\frac{\partial}{\partial t}, \boldsymbol{\nabla} \right) \quad (1.1)$$

is “naturally lowered.” The contraction between two four-vectors is independent of choice of reference system, commonly known as Lorentz-invariant.

1.2.2 Classical field theory

We formulate a theory of scalar fields $\Phi(x)$ in four-dimensional Minkowski spacetime in terms of the Lorentz-invariant action

$$S = \int d^4x \mathcal{L}(\Phi, \partial_\mu \Phi), \quad (1.2)$$

with \mathcal{L} being the *Lagrangian density* of the theory, a function of the set of fields Φ and its first derivatives. We will refer to \mathcal{L} simply as the Lagrangian, as is customary when working with fields.

This translates to a general (i.e. curved) n -dimensional spacetime through the construction of a Lorentz-invariant Lagrangian $\hat{\mathcal{L}}$,

$$S = \int d^n x \mathcal{L}(\Phi, \partial_\mu \Phi) = \int d^n x \sqrt{-g} \hat{\mathcal{L}}(\Phi, \nabla_\mu \Phi) \quad (1.3)$$

where $g \equiv \det(g_{\mu\nu})$ is the determinant of the metric, and

$$d^n x \sqrt{-g} = dx^0 \wedge dx^1 \wedge \cdots \wedge dx^{n-1} \sqrt{-g} \quad (1.4)$$

is the invariant volume element [11]. What was applied here, was the **minimal-coupling principle**, and we may refer to \mathcal{L} as the minimally-coupled Lagrangian (density). Loosely speaking, this principle involves replacing the Minkowski metric with the curved-spacetime metric ($\eta_{\mu\nu} \rightarrow g_{\mu\nu}$), and partial derivatives to covariant derivatives ($\partial_\mu \rightarrow \nabla_\mu$).

Action principle. We use variational calculus to obtain the fields' equations of motion. For a scalar field ϕ , we consider the change $\phi \rightarrow \phi + \delta\phi$ and apply this to the action, such that $S \rightarrow S + \delta S$. After isolating S and gathering terms up to leading order, we set $\delta S = 0$ and obtain an equation for ϕ in terms of first and second derivatives.

1.2.3 Mathematical tools

Method of Green's functions

A linear ordinary differential equation (ODE) $L_x f(x) = g(x)$ assumes a linear differential operator L , an unknown function f , and a right-hand side g that forms the inhomogeneous part of the ODE. The **Green's function** G for the ODE (or L) manifests as any solution to $L_x G(x, y) = \delta(x - y)$. Now

$$f(x) = \int dy G(x, y)g(y) \quad (1.5)$$

solves the original ODE.

Topology

The **n -torus** \mathbb{T}^n is the n -fold product of the circle \mathbb{S}^1 , [39]

$$\mathbb{T}^n = \underbrace{\mathbb{S}^1 \times \cdots \times \mathbb{S}^1}_n \equiv (\mathbb{S}^1)^n. \quad (1.6)$$

“Gluing” pairs of opposite-facing sides of a cube—which is to impose periodic boundary conditions—gives a 3-torus. 3-tori have no boundaries and are equivalent to infinite flat spaces with a periodically repeated cubic templates [11].

The cyclic group

The cyclic group, denoted \mathbb{Z}_n , describes a symmetry of a plane figure that remains invariant after a rotation of $2\pi/n$ radians (or $360^\circ/n$ degrees), where $n \in \mathbb{Z}$ (n is integer) [39]. We consider a subgroup of this in this thesis, namely discrete \mathbb{Z}_2 -symmetries, also called reflectional symmetries, which amount to invariance under change of sign: $\phi \rightarrow e^{i2\pi/2}\phi = -\phi$.

1.2.4 Cosmic scales

Chronology

The standard model of cosmology provides multiple time measurements that are useful for different applications. Cosmic time t is often impractical to use in physical cosmology, but it gives a certain intuition that other measures of time may lack. In this thesis, we give cosmic time estimates (in units of (giga)years) from the perspective of a flat Λ CDM model consisting of 31% non-relativistic matter and 69% vacuum energy today (Eq. (1)). In the following, we introduce alternative time measures such as redshift and scale factor.

The Doppler shift in electromagnetic waves arising from the recession of distant objects is

$$\text{redshift} = \frac{\text{observed wavelength} - \text{emitted wavelength}}{\text{emitted wavelength}}.$$

This shift is determined by the change in proper distance between two comoving points,

$$\frac{\text{proper distance now}}{\text{proper distance then}} = \frac{\text{scale factor now} \times \text{comoving distance}}{\text{scale factor then} \times \text{comoving distance}}.$$

This **cosmic scale factor** is denoted $a = a(t)$. Normalised such that “now” means “today”, we get

$$1 + \mathfrak{z} = a_0/a(t), \quad (1.7)$$

where $a_0 = a(t_0) \equiv 1$ is the scale factor today, and \mathfrak{z} the **cosmic redshift**. We denote it in this thesis with \mathfrak{z} to distinguish it from the Cartesian spatial z -coordinate, as they both are frequently used variables. To give some examples, redshifts $\mathfrak{z} = 0$ and $\mathfrak{z} = 2$ correspond to the universe at $t = t_0 \approx 13.8$ gigayears (today) and $t \approx 3.2$ gigayears old, respectively, defined as the coordinate time that has passed since $a(t \equiv 0) = 0$.

In this thesis we make use of **conformal time** τ for which $dt = ad\tau$ holds in units with $c = 1$. We will use $\dot{\cdot} \equiv d/d\tau$ as a shorthand notation for derivatives with respect to conformal time. Other common measures of time include the physical Hubble factor $H = 1/a da/dt$, and conformal Hubble factor $\mathcal{H} = aH = \dot{a}/a$.

Comoving and physical scales

We use comoving measures of distances and relate these to comoving wavenumbers k , which again is related to comoving wavelength λ . We adapt the convention in Maggiore [43] and use **reduced wavelengths**

$$\lambda \equiv 1/k = \lambda/(2\pi). \quad (1.8)$$

Comoving scales remain constant in time. We refer to modes with wavelengths larger than the horizon, $\lambda \gg \mathcal{H}^{-1}(a)$, as **super-horizon** modes, where $\mathcal{H} = 1/a da/d\tau$ is the conformal Hubble factor (Eq. (2.31)) or the “comoving horizon.” Modes well inside the horizon, $\lambda \ll \mathcal{H}^{-1}(a)$ are **sub-horizon**. Now, we obtain physical measurements via $k_{\text{ph}}(a) = k/a$ and $\lambda_{\text{ph}}(a) = a\lambda$.

1.2.5 Cosmological simulations

Simulations of cosmological scenarios are a topic of high-performance computing (HPC) and usually performed on three-dimensional lattices with periodic boundaries (i.e. 3-tori, \mathbb{T}^3). Say we have such a cubic lattice of side lengths L , with N points in each direction, giving a spatial resolution of $\Delta = L/N$. The **fundamental frequency** is the smallest frequency mode, which in terms of wavenumber is $k_{\text{IR}} = 2\pi/L$. The **Nyquist frequency**, given by the angular frequency $k_{\text{UV}} = k_{\text{IR}}N/2 = \pi N/L$, is the highest resolvable frequency.

High-performance computing

There are two main parallelisation techniques used in HPC; the distributed-memory standard Message Passing Interface (**MPI**), and the shared-memory Open Multi-Processing (**OpenMP**) application. The MPI standard functions on parallel computing architectures, such as computer clusters. In lattice simulations, this amounts to a clever division of tasks on different parts of the lattice.

Part I

Background

Chapter 2

General Relativity

Alongside quantum mechanics, Einstein's theory of gravity—general relativity—is widely accepted as the most accurate description of our surroundings. GR can be formulated from a geometrical point of view, or it can be viewed as a classical field theory. In the former approach we meet geometrical tools such as the geodesic equation, whereas the latter allows the application of field-theoretical methods. Considering both perspectives can be insightful and provide a better overall understanding of the concepts in GR [42].

This chapter will cover the parts of GR that are most relevant for this thesis. In Section 2.1 we will introduce relevant terminology from differential geometry and elaborate on some techniques for handling hypersurfaces and conformal spaces. We move on to discuss in broad terms the Einstein's equation in Section 2.2. A brief introduction to modern cosmology is found in Section 2.3, before we address gravitational waves in Section 2.4. Hopefully, this will be sufficient to obtain a basic understanding of standard GR.

2.1 Differential geometry

Einstein formulated GR in terms of spacetime geometries, using the mathematical discipline known as differential geometry. Whilst most prominent in physics, differential geometry has many applications in natural sciences. This section briefly introduces basic concepts and terminology of this mathematical branch. For formal definitions, see e.g. Carroll [11, Chapters 2 & 3].

Manifolds are topological spaces that locally *look like* Euclidian space. They are characterised by metric tensors that describe their geometries. For example, the Minkowski spacetime from special relativity is described by the metric tensor $\eta_{\mu\nu}$ (defined shortly) which is related to the line element through

$$ds^2|_M = \eta_{\mu\nu} dx^\mu dx^\nu = -dt^2 + \delta_{ij} dx^i dx^j, \quad (2.1)$$

where δ_{ij} is the Kronecker delta (Eq. (6)). In the standard picture, the coordinates are $x^\mu = (t, x, y, z)$ such that the last term above is the three-dimensional Euclidean line element in Cartesian coordinates. Minkowski manifolds are special cases of pseudo-Riemannian manifolds (discussed below).

Metric tensor

The **metric tensor** $g_{\mu\nu}$ is a symmetric rank-(0, 2) tensor that is non-degenerate ($\det(g) \neq 0$) and relates to the line element¹ as

$$ds^2 = g_{\mu\nu} dx^\mu dx^\nu. \quad (2.2)$$

Its inverse satisfies $g^{\mu\kappa} g_{\kappa\nu} = \delta^\mu_\nu$, and we usually denote the determinant by $g = \det(g)$. The metric tensor is used to raise and lower indices of other tensors, e.g. $A_\mu = g_{\mu\nu} A^\nu$.

Pseudo-Riemannian manifolds

A manifold \mathcal{M} with a metric $g_{\mu\nu}$ that, when put into its *canonical form* is [11]

$$g_{\mu\nu}|_{\text{canon.}} = \text{diag}(-1, +1, +1, \dots, +1), \quad (2.3)$$

is called Lorentzian or **pseudo-Riemannian**. For all practical purposes, it is to say that the spacetime has one time dimension and arbitrary number (D) of spatial dimensions. We say that \mathcal{M} has $D + 1$ dimensions with coordinates x^μ , and emphasise that Greek indices take the values $\mu = 0, i$ and Latin ones take $i = 1, \dots, D$. Now, there exists a unique connection $\Gamma^\rho_{\mu\nu}$ constructed from the metric, called the **Christoffel symbols** (Eq. (8)). From this we get important structures such as the **covariant derivative** ∇_μ (Eq. (3)) and the **Riemann curvature tensor** $\mathcal{R}^\rho_{\sigma\mu\nu}$ (Eq. (9)). Further, one can construct the **Ricci tensor** $\mathcal{R}_{\mu\nu} = \mathcal{R}^\lambda_{\mu\lambda\nu}$, the contraction of which is the **Ricci scalar** $\mathcal{R} = g^{\mu\nu} \mathcal{R}_{\mu\nu}$. The **Bianchi identities**, [11]

$$\mathcal{R}_{\mu\nu\alpha\beta;\gamma} + \mathcal{R}_{\mu\nu\gamma\alpha;\beta} + \mathcal{R}_{\mu\nu\beta\gamma;\alpha} = 0, \quad (2.4)$$

in GR reduce to $\mathcal{G}_{\mu\nu}^{;\nu} = \nabla^\nu \mathcal{G}_{\mu\nu} = 0$, where

$$\mathcal{G}_{\mu\nu} = \mathcal{R}_{\mu\nu} - \frac{1}{2} g_{\mu\nu} \mathcal{R} \quad (2.5)$$

is the **Einstein tensor**.

2.1.1 Hypersurfaces

A manifold Σ *embedded* (contained within) in another manifold \mathcal{M} is a submanifold of the ambient spacetime. We define an **induced metric**

$$\gamma_{ab} = X^\mu_{,a} X^\nu_{,b} g_{\mu\nu} \quad (2.6)$$

where $X^\mu(\xi^a)$ is the embedding function describing the mapping $\Sigma \rightarrow \mathcal{M}$, and ξ^a are the coordinates on Σ .

A **hypersurface** of a $(p + q)$ -dimensional manifold \mathcal{M} is a submanifold of codimension 1, i.e. with $p + q - 1$ dimensions. We write the metric in **Gaussian normal coordinates** $\{Y, \xi^a\}$ as

$$ds^2 = \varsigma dY^2 + \gamma_{ab} d\xi^a d\xi^b, \quad (2.7)$$

where γ_{ab} is the induced metric in Eq. (2.6) [11]. We have

$$\varsigma = n_\mu n^\mu = \begin{cases} -1 & \text{if } \Sigma \text{ is spacelike,} \\ +1 & \text{if } \Sigma \text{ is timelike,} \end{cases} \quad (2.8)$$

where $n^\mu = (\partial_Y)^\mu$ is the normal vector. This means that spacelike hypersurfaces have timelike normal vectors, and vice versa. We define the **extrinsic curvature** as a tensor \widehat{K}_{ab} on Σ by

$$\widehat{K}_{ab} \equiv -X^\mu_{,a} X^\nu_{,b} \nabla_\nu n_\mu. \quad (2.9)$$

Note that this definition tends to vary in references [11].

¹“Line element” and “metric” is often used synonymously.

2.1.2 Conformal geometry

The class of transformation called **conformal transformations** are in all essence local changes of scale. They are written

$$\tilde{g}_{\mu\nu} = \Upsilon^2(x)g_{\mu\nu}, \quad \exists \Upsilon(x) > 0, \quad (2.10)$$

where x denotes spacetime events on \mathcal{M} , and Υ is called the **conformal factor**. The convenience of conformal equivalence comes from the simple fact that any function of $g_{\mu\nu}$ can be thought of as a function of $\tilde{g}_{\mu\nu}$ and $\Upsilon(x)$ [11].

The inverse transformation is trivial, $g_{\mu\nu} = \Upsilon^{-2}(x)\tilde{g}_{\mu\nu}$, and the determinant transforms as $\sqrt{-\tilde{g}} = \Upsilon^d \sqrt{-g}$, where d is the dimension of the spacetime. The conformally-transformed Christoffel symbols take the form

$$\tilde{\Gamma}_{\mu\nu}^\rho = \Gamma_{\mu\nu}^\rho + C_{\mu\nu}^\rho, \quad (2.11)$$

where

$$C_{\mu\nu}^\rho = \Upsilon^{-1} \left(2\delta_{(\mu}^\rho \Upsilon_{,\nu)} - g_{\mu\nu} g^{\rho\sigma} \Upsilon_{,\sigma} \right). \quad (2.12)$$

We obtain neat expressions for the Riemann and Ricci tensors and the Ricci scalar, which we will not list here.

Consider a scalar field ϕ . We get $\tilde{\phi}_{;\mu} = \phi_{;\mu} = \phi_{,\mu}$ for the covariant derivative, and as for the d'Alembertian,

$$\tilde{\square}\phi = \Upsilon^{-2} \square\phi + (d-2)g^{\rho\sigma}\Upsilon^{-3}\Upsilon_{,\rho}\phi_{;\sigma}. \quad (2.13)$$

Below, we consider two special cases of such relations that will be of use in this thesis.

Expanding universe

If $\Upsilon(x) = a(\tau)$ and $ds^2 = -d\tau^2 + d\Sigma^2$, where Σ is a spacelike hypersurface with a given Gaussian curvature, then $\tilde{ds}^2 = a^2 ds^2$ is the Friedmann–Lemaître–Robertson–Walker (FLRW) line element (see Section 2.3). If $\Sigma = \mathbb{R}^3$, the metric $\tilde{g}_{\mu\nu}$ is said to be conformally flat. We define the Fourier transform of a function $f(\mathbf{x})$ of comoving coordinates \mathbf{x} as

$$\tilde{f}(\mathbf{k}) = \int d^3x f(\mathbf{x}) e^{i\mathbf{k}\cdot\mathbf{x}}, \quad (2.14a)$$

and its inverse

$$f(\mathbf{x}) = \int \frac{d^3k}{(2\pi)^3} \tilde{f}(\mathbf{k}) e^{-i\mathbf{k}\cdot\mathbf{x}}, \quad (2.14b)$$

where \mathbf{k} is the comoving wavevector. The comoving frame relates these coordinates to physical coordinates by $\mathbf{x}_{\text{ph}} = a\mathbf{x}$ and $\mathbf{k}_{\text{ph}} = \mathbf{k}/a$.

The d'Alembertian is

$$\tilde{\square}\phi = a^{-2} (\square_M \phi - 2\mathcal{H}\partial_\tau \phi), \quad (2.15)$$

where $\mathcal{H} = a^{-1}\partial_\tau a$ and $\square_M \equiv \partial^\mu \partial_\mu$.

Note that more often than not, the tilde will be reserved for other quantities, and the metric $g_{\mu\nu}$ will refer to the generalised metric or FLRW if specified.

Scalar–tensor theories

A scalar–tensor theory (see Section 3.2) with auxiliary field $\phi(x)$ can be formulated (mathematically) equivalently in two different reference frames related by $\tilde{g}_{\mu\nu} = A^2(\phi)g_{\mu\nu}$. Here, $g_{\mu\nu}$ defines what is known as the **Einstein frame**, and $\tilde{g}_{\mu\nu}$ the **Jordan frame**.

2.2 Einstein's equation

How does the gravitational field affect how matter behaves, and in what way is matter controlling the gravitational field? Newtonian gravity proposes very good answers to these questions: The acceleration of an object in a gravitational potential Φ is

$$\mathbf{a} = -\nabla\Phi, \quad (2.16)$$

and said field is governed by the matter density ρ through the Poisson equation

$$\nabla^2\Phi = 4\pi G_N \rho. \quad (2.17)$$

In physics, the answer to a question is highly dependent on *how the question was asked*. A common misconception is that Newtonian gravity was disproven by Einstein. Newton was simply telling a different story; a story about dynamics in non-relativistic systems.² The discovery of the limitations to Newtonian dynamics (cf. precision of Mercury's orbit) called for novel descriptions of gravitation. Einstein confronted gravitational physics with different but analogous questions, and subsequently more complex answers than Newton. General relativity explains how curvature of spacetime influences matter, manifesting as gravity, and in what way energy and momentum affects spacetime to create curvature. In mathematical terms, these are the **geodesic equation**

$$\frac{d^2x^\mu}{d\lambda^2} = -\Gamma_{\rho\sigma}^\mu \frac{dx^\rho}{d\lambda} \frac{dx^\sigma}{d\lambda} \quad (2.18)$$

and **Einstein's equation**

$$\mathcal{G}_{\mu\nu} = 8\pi G_N T_{\mu\nu}. \quad (2.19)$$

One can arrive at this equation by use of the minimal-coupling principle and Bianchi identities (Eq. (2.4)), as explained in Carroll [11, Chapter 4]. A more tangible way to obtain the same equation is to vary the combined matter and Einstein–Hilbert actions $S = S_{\text{EH}} + S_m$, where [11]

$$S_{\text{EH}} = \frac{M_{\text{Pl}}^2}{2} \int d^4x \sqrt{-g} \mathcal{R}. \quad (2.20)$$

The result is [11]

$$\mathcal{R}_{\mu\nu} - \frac{1}{2} g_{\mu\nu} \mathcal{R} = -\frac{1}{M_{\text{Pl}}^2} \frac{2}{\sqrt{-g}} \frac{\delta S_m}{\delta g^{\mu\nu}}, \quad (2.21)$$

where the right-hand side is identified as proportional the energy–momentum tensor, $8\pi G_N T_{\mu\nu}$, and the left-hand side is the Einstein tensor $\mathcal{G}_{\mu\nu}$ (Eq. (2.5)). We see that Eqs. (2.19) and (2.21) are equivalent.

2.2.1 Energy–momentum tensor

The (Hilbert) **stress–energy (SE) tensor**, also known as the energy–momentum tensor, constitute the non-geometrical part of the Einstein equation—the right-hand side of Eq. (2.19). It encodes information about the energy and momentum contained in the system.

For a perfect fluid, the SE tensor in the fluid rest frame is $T^\mu_\nu = \text{diag}(-\rho, p, p, p)$ where $\rho = -T^0_0$ is the homogeneous energy density and $p = (1/3)T^i_i$ is the isotropic pressure. We will address this in a cosmological context in the next section.

²Which, to be fair, are most common on Earth.

Conformal transformations

Let us comment on the energy–momentum tensor under conformal transformations (Eq. (2.10)). Consider the matter action in d spacetime dimensions

$$\tilde{S}_{(m)} = \int d^d x \sqrt{-\tilde{g}} \tilde{\mathcal{L}}_{(m)} = \int d^d x \sqrt{-g} \mathcal{L}_{(m)} = S_{(m)}, \quad (2.22)$$

where the Lagrangian $\tilde{\mathcal{L}}_{(m)} = \Upsilon^{-d} \mathcal{L}_{(m)}$ [19]. We let ${}^{(m)}T \triangleq T$ and ${}^{(m)}\tilde{T} \triangleq \tilde{T}$ denote the matter energy and momentum in the two frames for notational ease. Under Eq. (2.10), the *matter* SE tensor transforms as

$$\tilde{T}^\mu_\nu = \Upsilon^{-d} T^\mu_\nu, \quad (2.23)$$

and thus the trace $T \equiv g^{\mu\nu} T_{\mu\nu}$ transforms as $\tilde{T} = \Upsilon^{-d} T$.

As a result, we get different conservation laws in the two frames:

$$T^{\mu\nu}_{;\nu} = 0 \quad \Rightarrow \quad \tilde{T}^{\mu\nu}_{;\nu} = -\Upsilon^{-1} \Upsilon^\mu \tilde{T}, \quad (2.24)$$

or vice versa:

$$\tilde{T}^{\mu\nu}_{;\nu} = 0 \quad \Rightarrow \quad T^{\mu\nu}_{;\nu} = \Upsilon^{-1} \Upsilon^\mu T. \quad (2.25)$$

2.2.2 Linearised gravity

Applying perturbation theory to the metric gives rise to a new set of equations, often referred to as the “linearised Einstein field equations.” The general starting point is to expand the metric to the order o in question,

$$\dot{g}_{\mu\nu} = g_{\mu\nu} + \sum_{i=1}^o (\delta^i g)_{\mu\nu}. \quad (2.26)$$

Consequently, the perturbed Einstein reads

$$\dot{\mathcal{G}}_{\mu\nu} = 8\pi G_N \dot{T}_{\mu\nu}, \quad (2.27)$$

where $\dot{\mathcal{G}}_{\mu\nu}$ and $\dot{T}_{\mu\nu}$ are the o th-order perturbed Einstein and SE tensor, respectively. Equation (2.27) is then solved order by order. We refer to Carroll [11], Dodelson & Schmidt [21], Jokela et al. [35], Maggiore [42] for calculations.

2.3 Modern cosmology

Employing the cosmological principle (CP) to the Einstein equation, simplifies them drastically. The cosmological principle states that the universe is spatially homogeneous and isotropic, or equivalently that the line element of the universe takes the form $ds^2 = -dt^2 + a^2(t)d\Sigma^2$ where $d\Sigma^2$ is a three-dimensional metric with a specified Gaussian curvature. The scale factor a describing the universe’s expansion is

$$a = \frac{1}{1 + z}, \quad (2.28)$$

where z is the cosmic redshift. This was the starting point for Alexander Friedmann (1888–1925) when he developed the Friedmann equations. If CP holds—which is widely accepted as a good approximation at large scales, typically orders larger than $\mathcal{O}(100 \text{ Mpc})$ —any constituent s behaves as a perfect fluid, and the Hubble parameter H reads

$$H^2 = H_0^2 \sum_s \Omega_{s0} a^{-3(1+w_s)}. \quad (2.29)$$

The parameter $\Omega_{s0} \equiv \rho_{s0}/\rho_{\text{cr0}}$ is a dimensionless present-day energy density measure, normalised to the critical density today, $\rho_{\text{cr0}} = 3H_0^2 M_{\text{Pl}}^2$. The equation-of-state parameter of s , w_s , is given by

$$\text{isotropic pressure} = w \cdot \text{energy density}.$$

Table 2.1 provides an overview of the various phenomena (potentially) contributing to the total energy in the universe.

We will work with conformal time τ that relates to cosmic time t such that the metric is

$$ds^2 = a^2(-d\tau^2 + d\Sigma^2). \quad (2.30)$$

Subsequently, we make use of the conformal Hubble factor $\mathcal{H} \equiv aH$, given by

$$\mathcal{H}^2 = H_0^2 \sum_s \Omega_{s0} a^{-(1+3w_s)}, \quad (2.31)$$

To get simplified—or simply analytically solvable—equations, we often assume $a \sim \tau^\alpha$ that corresponds to a universe dominated by a single substance. Now, α is ultimately determined by the equation-of-state parameter w_s associated with the substance s in question,

$$\alpha = \frac{2}{1 + 3w_s}. \quad (2.32)$$

This means that $\alpha = 1$ and $\alpha = 2$ for radiation (RD) and matter domination (MD), respectively.

EOS ^a	Energy ^b	Scale fac. ^c	Constituent	Top. defect ^d
$w = 1/3$	$\rho \propto a^{-4}$	$a \sim \tau^1$	ultra-relativistic matter (photons, neutrinos)	
$w = 0$	$\rho \propto a^{-3}$	$a \sim \tau^2$	non-relativistic matter (CDM, baryons)	monopoles
$w = -1/3$	$\rho \propto a^{-2}$		curvature	cosmic strings
$w = -2/3$	$\rho \propto a^{-1}$	$a \sim \tau^{-2}$		domain walls
$w = -1$	$\rho \propto a^0$	$a \sim \tau^{-1}$	cosmological constant (vacuum, dark energy)	
$w < -1$			phantom energy [43, 45]	

^aEffective equation-of-state parameter, $w = p/\rho$.

^bEnergy density scaling, $\rho \propto a^{-3(1+w)}$.

^cScale factor $a \sim \tau^\alpha$.

^dNetwork of topological defects modelled as a perfect fluid. Isotropic pressure is $p = -(D/3)\rho$, where D is the dimension of the defect [54, 55].

Table 2.1: Perfect-fluid description of various phenomena. The last column shows the corresponding topological defect, which will be introduced in Section 3.1.

With fiducial observed values for $\Omega_{\text{r}0}$, $\Omega_{\text{m}0}$ and $\Omega_{\Lambda0}$, it is understood that our universe was dominated by radiation in its early stages, after inflation and until before $a = \Omega_{\text{r}0}/\Omega_{\text{m}0}$ (when $\rho_{\text{m}} = \rho_{\text{r}}$, about 50 thousand years after Big Bang). The universe entered a matter-dominated era after this, until $a = (\Omega_{\text{m}0}/\Omega_{\Lambda0})^{1/3}$ (when $\rho_{\Lambda} = \rho_{\text{m}}$, about 10 billion years after Big Bang). The universe started accelerating, and is currently on steady course to a vacuum-dominated era.

Hubble trouble

The **Hubble tension** refers to a discrepancy between measurements of the Hubble constant describing the expansion rate of the universe. Different methods yield conflicting values of $H_0 = 100 \text{ h km s}^{-1} \text{ Mpc}^{-1}$, where h is the reduced Hubble constant. Local measurements involving for example distant supernovae suggest $\text{h} \approx 0.73$ [e.g. 43]. In contrast, the other

approach, derived from CMB observations by the Planck satellite, indicates $h \approx 0.67$ [e.g. 43]. Their confidence intervals do not overlap, thus necessitating new measurements [e.g. 43].

Many argue that revision of Λ CDM is necessary. The accelerated expansion is a late-universe phenomenon conservatively made clear by the dark-energy/cosmological-constant duality, with $w_{\text{de}} = w_{\Lambda} = -1$. Introducing instead a time-dependent “phantom” equation-of-state parameter $w_{\text{de}}(a)$ can harmonise the two measurements [43].

2.3.1 Cosmological perturbation theory

Just look around you—the universe is definitely *not* homogeneous and isotropic. The story of structure formation as we know it is told through cosmological perturbation theory. The leading-order perturbed metric $\dot{g}_{\mu\nu} = g_{\mu\nu} + \delta g_{\mu\nu}$ can be written in terms of functions A , B_i and C_{ij} ,

$$\dot{ds}^2 = a^2 \left[-(1 + 2A)d\tau^2 + 2B_i dx^i d\tau + (\delta_{ij} + C_{ij})dx^i dx^j \right]. \quad (2.33)$$

It is convenient to adopt the convention that spatial vectors and tensors are raised and lowered with δ , e.g. $C^{ij} = \delta^{ik}\delta^{jl}C_{kl}$. The symmetric metric has ten degrees of freedom, and a scalar-vector-tensor (SVT) decomposition separates these into scalar perturbations A , B , C , D , vector perturbations F_i , G_i , and tensor perturbations E_{ij} :

$$A \rightarrow A, \quad (2.34a)$$

$$B_i \rightarrow \partial_i B + F_i, \quad (2.34b)$$

$$C_{ij} \rightarrow (2\delta_{ij}C + 2\partial_i\partial_j D - (2/3)\delta_{ij}\nabla^2 D) + 2\partial_{(i}G_{j)} + 2E_{ij}. \quad (2.34c)$$

This is extremely useful since in the first-order linearised Einstein equation for scalars, vectors and tensors do not mix. We treat these separately and assume they originate from inflation. This thesis focuses solely on the tensorial part of the metric perturbation. Therefore, we will consider the divergence- and traceless $h_{ij} = 2E_{ij}$. This particular choice is called the **transverse-traceless** (TT) **gauge**, and will be addressed in the next section. Plugging this into the linearised Einstein equation Eq. (2.27), we get the equation of motion for the tensor perturbations h_{ij} , which (spoiler alert) are in fact the gravitational waves.

2.4 Gravitational waves

Gauge freedom, in a general context, refers to the invariance of a physical theory under certain transformations that do not alter the observable quantities or physical content of the theory. In GR, gauge freedom manifests as invariance under coordinate transformations, which is used to simplify the metric or solve Einstein’s equation more easily. By choosing an appropriate gauge we can eliminate redundancies.

Metric perturbations on a homogeneous and isotropic background leaves two tensor degrees of freedom. We isolate the physical, observable components of metric tensor perturbation by selecting the TT gauge, defined by

$$h_{0\mu} = 0, \quad h_i^i = 0, \quad h_{ij}^{;i} = 0, \quad (2.35)$$

where $\dot{g}_{\mu\nu} = a^2(\eta_{\mu\nu} + h_{\mu\nu})$. In Fourier space where $\partial_i \leftrightarrow ik_i$, Eq. (2.35) becomes

$$\tilde{h}_{0\mu} = 0, \quad \tilde{h}_i^i = 0, \quad k^i \tilde{h}_{ij} = 0. \quad (2.36)$$

We extract the TT-part of a symmetric 3×3 tensor by use of the projection tensor in Eq. (10). The spin-2 projector is non-local in space, and we define the TT-projected tensor in coordinate space as

$$h_{ij}(\tau, \mathbf{x}) = \int \frac{d^3k}{(2\pi)^3} e^{-ik \cdot x} \Lambda_{ij}^{kl}(\mathbf{k}) \tilde{h}_{kl}(\tau, \mathbf{k}). \quad (2.37)$$

In the **linear polarisation basis** we consider plus- (+) and cross- (\times) polarised states. Said basis is given by tensors [42]

$$\begin{aligned} e_{ij}^+(\mathbf{k}) &= \hat{\mathbf{m}} \otimes \hat{\mathbf{m}} - \hat{\mathbf{n}} \otimes \hat{\mathbf{n}}, \\ e_{ij}^\times(\mathbf{k}) &= \hat{\mathbf{m}} \otimes \hat{\mathbf{n}} - \hat{\mathbf{n}} \otimes \hat{\mathbf{m}}, \end{aligned} \quad (2.38)$$

where the momentum vector $\mathbf{k} = k\hat{\mathbf{Q}}$ defines the right-handed orthonormal basis $\{\hat{\mathbf{m}}, \hat{\mathbf{n}}, \hat{\mathbf{Q}}\}$, and

$$e_{ij}^P e_{P'}^{ij} = 2\delta_{P'}^P. \quad (2.39)$$

The tensor representation is written as a superposition of these states,

$$h_{ij} = h_+ e_{ij}^+ + h_\times e_{ij}^\times = \sum_{P=+, \times} \mathcal{F}_x^{-1} \{ \tilde{h}_P e_{ij}^P \}. \quad (2.40)$$

Note that

$$|h|^2 = h^{ij} h_{ij} = 2 \sum_P h_P^2. \quad (2.41)$$

2.4.1 Expanding universe

We are interested in a flat FRLW background plus first order in perturbations, and define the perturbed metric as $\mathring{g}_{\mu\nu} = a^2(\eta_{\mu\nu} + h_{\mu\nu})$. Furthermore, we focus on the tensorial part of the perturbations, leaving

$$ds^2 = a^2(\tau)(-d\tau^2 + [h_{ij} + h_{ij}(\tau, \mathbf{x})]dx^i dx^j) \quad (2.42)$$

for the perturbed line element.

We define an anisotropic stress-energy tensor $\Pi_{ij} \equiv T_{ij} - \delta_{ij}\delta^{kl}T_{kl}$, and project it onto the TT gauge. It is useful to define a stress-energy tensor whose indices are raised and lowered with δ_{ij} . We impose the TT-conditions in Eq. (2.35) on this such that

$$\pi_{ij} = \pi^{ij} = \pi^i_j \equiv \Pi^i_j|_{\text{TT}} = a^{-2}\Pi_{ij}^{\text{TT}} = a^{-2}\Lambda_{ij}^{kl}\Pi_{kl}. \quad (2.43)$$

Note that $\Pi_{ij}^{\text{TT}} = T_{ij}^{\text{TT}}$. We consider the linearised Einstein equation (Eq. (2.27)) in this gauge. Now, to first order we have $\delta G^i_j = 8\pi G_N \delta T^i_j$ as the only non-vanishing components, giving [43]

$$-\frac{1}{2}\square h_{ij} = 8\pi G_N \pi_{ij}. \quad (2.44)$$

The equation of motion for h_{ij} is [21]

$$\ddot{h}_{ij} + 2\mathcal{H}\dot{h}_{ij} - \nabla^2 h_{ij} = 16\pi G_N a^2 \pi_{ij} \quad (2.45)$$

where a dot signifies the conformal time derivative, $\dot{\cdot} \equiv d/d\tau$.

It is convenient to introduce a scaled strain $\psi \equiv ah$ and transform to Fourier space. The equation now reads

$$\ddot{\psi}_P + \left(k^2 - \frac{\ddot{a}}{a}\right)\tilde{\psi}_P = k^2 f_P; \quad P = +, \times, \quad (2.46)$$

where

$$f_P \equiv \frac{16\pi G_N a^3 \tilde{\pi}_P(\tau, \mathbf{k})}{k^2}. \quad (2.47)$$

Homogeneous solution. We see that for small modes $k \gg \ddot{a}/a \sim \tau^{-2}$, the linear operator is approximately $\partial_\tau^2 + k^2$, i.e. the harmonic oscillator, with plane wave solutions for $f_P = 0$. That is to say, small-scale gravitational waves, in the absence of a source, propagate free waves in an FLRW spacetime (divided by the scale factor). On larger scales, the propagation is damped in accordance with the expansion of the universe. This damping term generally depends on expansion history.

Inhomogeneous solution. The method of Green's functions presents a suitable recipe for determining the dynamics of tensor perturbations on an expanding background. There are some limitations, however, as to the analytical solvability of the system. In the small-scale limit, the damping is neglected, and we only need the retarded Green's function associated with the harmonic oscillator, $\sin(k(\tau - \tau'))/k$. Otherwise, an equation of the form $L_{u=k\tau} \tilde{\psi}_P = f_P$, where

$$\frac{d^2}{du^2} + \left(1 - \frac{(\alpha - 1)\alpha}{u^2}\right) \quad (2.48)$$

has a Green's function in terms of Bessel functions $\sqrt{u}Z_{\alpha-1/2}(u)$, which is the case of power-law expansion, $a \propto \tau^\alpha$. On a compact form, if $n \equiv \alpha - 1 \in \mathbb{Z}$, we can use the Green's function

$$G(u, v) = S_n(u)C_n(v) - C_n(u)S_n(v) \quad (2.49)$$

where $S_n(x)$ and $C_n(x)$ are the Riccati–Bessel and –Neumann functions (given in Eq. (A.9)).

Assume homogeneous initial conditions $\tilde{\psi}_P(\tau_i, \mathbf{k}) = \dot{\tilde{\psi}}_P(\tau_i, \mathbf{k}) = 0$. The full solution is as follows:

$$a(\tau)\tilde{h}_{ij}(\tau, \mathbf{k}) = \frac{16\pi G_N}{k^2} \int_{\tau_i}^{\tau} d\hat{\tau} G(k\tau, k\hat{\tau})a^3(\hat{\tau})\tilde{\pi}_{ij}(\hat{\tau}, \mathbf{k}). \quad (2.50)$$

If the source disappears after $\tau_f - \tau_i$, we may write the solution as

$$\tilde{\psi}_{ij}(\tau, \mathbf{k}) = S_n(k\tau)F_2(\mathbf{k}) - C_n(k\tau)F_1(\mathbf{k}) \quad (2.51)$$

with

$$F_i(\mathbf{k}) = \int_{\tau_i}^{\tau_f} d\hat{\tau} R_n^{(i)}(k\hat{\tau})f_P(\hat{\tau}, \mathbf{k}), \quad (2.52)$$

where $R^{(i)}$ refers to the Riccati–Bessel function of i th kind.

Gravitational radiation

The gravitational-wave energy density is given by [43]

$$\rho_{gw}(\tau) = \frac{1}{16\pi G_N a^4(\tau)} \sum_{P=+, \times} \langle (\dot{\psi}_P - \mathcal{H}\psi_P)^2(\tau, \mathbf{x}) \rangle. \quad (2.53)$$

For sub-horizon modes, $\dot{\psi}_P \sim k\psi_P \gg \mathcal{H}\psi_P$, and therefore

$$\rho_{gw}(\tau) \simeq \frac{1}{16\pi G_N a^4(\tau)} \sum_{P=+, \times} \langle \dot{\psi}_P^2(\tau, \mathbf{x}) \rangle. \quad (2.54)$$

With the spatial average over a volume V [22, 43]

$$\frac{1}{V} \int_{V \gg \lambda^3} d^3x e^{i(\mathbf{k}-\mathbf{k}') \cdot \mathbf{x}} = \frac{(2\pi)^3}{V} \delta^{(3)}(\mathbf{k} - \mathbf{k}') \quad (2.55)$$

where $\lambda \sim 1/k, 1/k'$, we obtain

$$\rho_{\text{gw}}(\tau) \simeq \frac{1}{16\pi G_N a^4(\tau)} \frac{1}{V} \sum_{P=+, \times} \int \frac{d^3k}{(2\pi)^3} |\dot{\psi}_P(\tau, \mathbf{k})|^2 \quad (2.56)$$

as a measure of the energy density of gravitational waves in an expanding universe, where $\psi_P = ah_P$, $\dot{\psi}_P = d\psi_P/d\tau$ and $P = +, \times$.

Chapter 3

Symmetry-Breaking Dark Energy

When a system spontaneously changes from one physical state to another due to external conditions such as temperature or pressure reach certain critical points, it is said to undergo a **phase transition**. Water, for example changes from liquid to gas at the critical temperature 100° C, given atmospheric pressure. Spontaneous symmetry breaking (SSB), an important concept in particle physics and cosmology especially, occurs when the physical laws possess a certain symmetry, but the vacuum state does not [37].

Topological defects, or topological **solitons**, are ubiquitous and manifest in a variety of forms across different scales and systems. Their hypothesised existence in exotic environments such as the early universe is further motivated by proofs of their existence in everyday life, such as whorls, loops and arches in our fingerprints [25]. It was in fact a very mundane event in 1834 that induced the first formal description of a soliton; John Russell Scott (1808–1882) keenly observed a hump of water moving from the prow of a boat rapidly down a canal whilst preserving its shape [54]. Such solitary waves that can interact with others and restore its shape were later named “solitons”.

3.1 Cosmological defects

Solitons are remarkably stable “humps” of energy. The simplest soliton is the topological soliton best known as the **kink**. Kink solutions placed in spacetime with more than one spatial dimension become extended, planar structures (or membranes), which we will call “domain walls” [54]. Domain walls possess richer dynamics than kinks, and these are quite well understood in Minkowski spacetimes. In contrast to higher codimension defects like strings and monopoles, kinks and domain walls are of codimension one and therefore also hypersurfaces, at least approximately. The study of kinks and domain walls can to some extent be applied to other topological defects [54].

Domain walls are of particular interest in this thesis, specifically the \mathbb{Z}_2 type. These two-dimensional topological defects occur where a discrete symmetry is broken.¹ To give an idea of the basic properties of topological defects, we present an example. More thorough derivations can be found in Vachaspati [54].

¹Likewise, cosmic strings and monopoles are products of axial/cylindrical and spherical symmetry breaking, respectively.

3.1.1 The stationary \mathbb{Z}_2 kink

The king of kinks, the so-called “ \mathbb{Z}_2 kink,” can be described through a scalar field ϕ with the action $S = S_{\text{EH}} + S_{\mathbb{Z}_2}$,

$$S_{\mathbb{Z}_2} = \int d^{n+1}x \sqrt{-g} \left\{ -\frac{1}{2} g^{\mu\nu} \partial_\mu \phi \partial_\nu \phi - V(\phi) \right\}, \quad (3.1)$$

where $V(\phi)$ is the two-fold degenerate potential $V(\phi) = \lambda(\phi^2 - \eta^2)^2$. The equation of motion $\square\phi = V_{,\phi}$ is derived from variation of S with respect to ϕ . For simplicity, we consider Minkowski spacetime with $1 + 1$ dimensions where $\eta_{\mu\nu} = \text{diag} = (-1, 1)$ is the metric. The equation of motion reads

$$-\partial_t^2 \phi + \partial_x^2 \phi = \lambda(\phi^2 - \eta^2)\phi. \quad (3.2)$$

Setting time derivatives to zero, and imposing boundary conditions $\phi(x \rightarrow \pm\infty) = \pm\eta$, we obtain a class of static solutions

$$\phi_k(x - x_0) = \eta \tanh \left(\sqrt{\frac{\lambda}{2}} \eta (x - x_0) \right), \quad (3.3)$$

where x_0 is the position of the kink.

Multi-kink field. Without commenting further, we state that this kink has *topological charge*² $Q = 1$. This comes from the boundary conditions, and thus similar arguments construct solutions with $Q = -1$ by swapping the boundaries; $\phi(x \rightarrow \pm\infty) = \mp\eta$. This is the *antikink* solution $\bar{\phi}_k(x) = -\phi_k(x)$. A feature of the \mathbb{Z}_2 kinks is that one cannot have a system with total topological charge $|Q| > 1$. For sufficiently separated kinks and antikinks located at $x = x_1, x_2, \dots, x_N$ and $x = \bar{x}_1, \bar{x}_2, \dots, \bar{x}_M$, respectively, we write [54]:

$$\phi(x) = \frac{\eta}{\eta^{N+M}} \prod_{i=1}^N \phi_k(x - x_i) \prod_{j=1}^M \bar{\phi}_k(x - \bar{x}_j), \quad (3.4)$$

where $|N - M| \leq 1$ and $x_i < \bar{x}_j < x_{i+1}$. This describes the allowed system of N kinks and M antikinks aligned in an alternating structure.

Basic properties

The energy of the kink is obtained integrating over the energy density, i.e.

$$E = - \int dx T^0_0 = \frac{2\sqrt{2}}{3} \lambda \eta^3. \quad (3.5)$$

We define the half-width of the kink to be

$$w = \frac{1}{\eta \sqrt{\lambda}}. \quad (3.6)$$

Most of the energy is confined within $x \in x_0 \pm w$. See Fig. 3.1 for illustrative explanation accompanied by a demonstration of how a Gaussian with standard deviation $w/\sqrt{2}$ tracks the kink’s energy profile.

²See Vachaspati [see 54, Chapter 1] for discussion

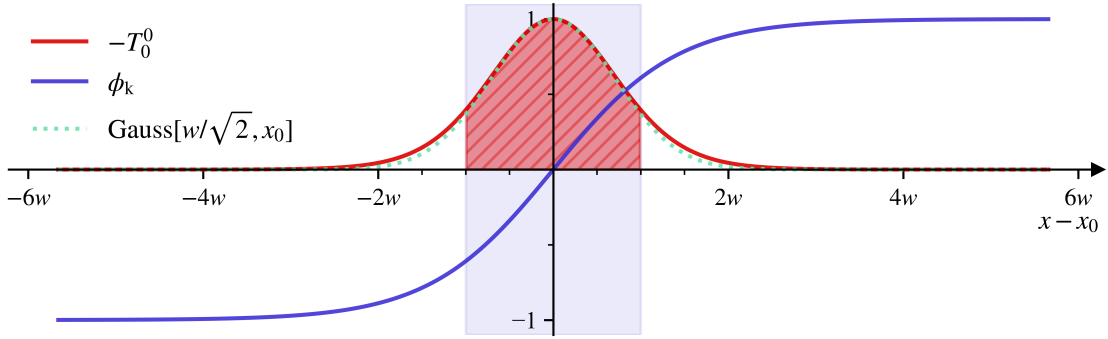


Figure 3.1: Demonstration of the \mathbb{Z}_2 kink and its energy content for $\eta = 1$ and $\lambda = 2$. The green dotted graph is a Gaussian around $x = x_0$ with standard deviation $w/\sqrt{2}$. Inspiration from Vachaspati [54].

3.1.2 Domain walls

The kink solution in Section 3.1.1 put in two more spatial dimensions (setting $\eta_{\mu\nu} = \text{diag}(-1, 1, 1, 1)$) is a planar \mathbb{Z}_2 domain wall. The volume integral in Eq. (3.5) is instead an integral over one axis, which means the result is a surface energy density. This is better known as the **surface tension** of the wall, denoted σ , and reads $\sigma = -\int dz T_0^0$ for a wall in the xy -plane. In analogy to the width parameter, we will refer to δ as the **wall thickness** (parameter), and we see from Fig. 3.1 that a Gaussian with standard deviation $\delta/\sqrt{2}$ tracks the energy density well.

For later convenience, we define σ_∞ and δ_∞ as the surface tension and wall thickness as their solutions in the stationary \mathbb{Z}_2 scenario, respectively. In terms of the mass scale³ $\mu = \eta \sqrt{\lambda}$, this amounts to

$$\sigma_\infty \equiv \frac{2\sqrt{2}\mu^3}{3\lambda} \quad \text{and} \quad \delta_\infty \equiv \frac{1}{\mu}. \quad (3.7)$$

Cosmological implications

We can model a network of domain walls as a perfect fluid with equation-of-state parameter $w_{dw} = -2/3$ (Table 2.1).⁴ This implies that in the absence of a greater cosmological constant (if $\Omega_{\Lambda 0} < \Omega_{dw0}$), even a tiny energy contribution from this network would eventually dominate the energy density in the universe. As this overclosing of the universe happens before matter–vacuum equality, this contradicts observations.

The prototypical defect is manifestly stable (robust against perturbations) and dissipationless (survives indefinitely). One way to surpass the overclosing problem is to introduce an **energy bias** between the two vacua, so that the system eventually converges to the true minimum and the walls disappear [52]. Another method is to let σ decrease with time (melting domain walls), which is considered in Babichev et al. [7].

3.1.3 Defect formation

Cosmological defects typically form during a phase transition, and it is the nature of the associated (broken) symmetry that decides what type of defect we have at hand. We mention cosmic strings and monopoles arising from axial and spherical symmetry breaking, respectively. Domain walls—the main interest of this thesis—form when *discrete* symmetries are broken.

³In Part II we set $\phi_\infty = \eta$.

⁴This is easily seen from the trace Nambu–Goto stress–energy tensor in Minkowski space.

To study phase transitions, it is helpful to use the **effective potential** that takes into account the interaction between some field and a background [37, 54]. We will demonstrate this in Section 3.2 for a particular scalar-field theory.

Energy bias

Existence of discrete vacua implicates existence of domain walls. The degeneracy of these vacua ensures the stability of such walls. If we imagine a slight break in this degeneracy, that is, if one vacuum is favoured over another, *biased* domain walls form [54]. Some models employ an energy gap directly into the potential. A generalisation of the symmetron model [31]—the *asymmetron* [47]—includes a cubic term in the effective potential that also changes the vacuum expectation value. We will discuss the latter in Section 3.2.2.

3.2 Scalar-field theories

The general picture interprets scalar-field theories as a group of scalar–tensor theories; a subgroup of modifications to gravity in which a scalar field is added to the total action. By going through all possible covariants with maximum second-order time-derivatives in four-dimensional spacetime, one arrives at the most general formulation of these types of theories, the *Hordenski theory*. Said theory is summed up by the total Lagrangian density $\mathcal{L}_H = \mathcal{L}_m + M_{Pl}^2 \sum_{i=2}^5 \mathcal{L}_i$, where \mathcal{L}_i are built up by derivatives of the scalar field, the Einstein tensor and arbitrary functionals of the scalar field ϕ and its kinetic term $X = -\frac{1}{2}\phi^{;\mu}\phi_{;\mu}$.⁵ Let $\mathcal{L}_i = 0$ as a starting point. General relativity—represented by the Einstein–Hilbert action—is retrieved with $\mathcal{L}_4 = \mathcal{R}/2$. By also setting $\mathcal{L}_2 = X(\phi) - V(\phi)$, we get a *quintessence* model. Performing relevant variations eventually gives an equation of motion that is indistinguishable from standard GR with $\mathcal{L}_m \rightarrow \mathcal{L}_m + \mathcal{L}_2$ in the stress–energy tensor on the right-hand side of the Einstein equation. Thus, quintessence models are not actually modified gravity theories, but adds to the total matter in the universe, and should be classified as a scalar-field theory rather than a scalar–tensor theory.

3.2.1 General framework

Let us go through the dynamics of a scalar field ϕ that is associated with a kinetic term $X = -\frac{1}{2}g^{\mu\nu}\phi_{;\mu}\phi_{;\nu}$ and potential energy $V(\phi)$ in broad terms. This will lay the foundation for our treatment of the (a)symmetron model in Section 3.2.2.

The dynamics of the bosonic field ϕ is described by the Einstein-frame (see Section 2.1.2) action

$$S = \int d^4x \sqrt{-g} \left\{ \frac{M_{Pl}^2}{2} \mathcal{R} + X(\phi) - V(\phi) \right\} + S_{(m)}[\tilde{g}_{\mu\nu}, \Psi], \quad (3.8)$$

where Ψ collects all matter fields, which couple minimally to the Jordan-frame metric,

$$\tilde{g}_{\mu\nu} = A^2(\phi) g_{\mu\nu} \quad (3.9)$$

⁵With the usual notation convention and arbitrary functionals G_i , the Lagrangian densities \mathcal{L}_i are given by the following:

$$\begin{aligned} \mathcal{L}_2 &= G_2(\phi, X), \\ \mathcal{L}_3 &= G_3(\phi, X)\square\phi, \\ \mathcal{L}_4 &= G_4(\phi, X)\mathcal{R} + G_{4,X}(\phi, X)((\square\phi)^2 - \phi_{;\mu\nu}\phi^{;\mu\nu}), \\ \mathcal{L}_5 &= G_5 G_{\mu\nu}\phi^{;\mu\nu} - \frac{1}{6}G_{5,X}(\phi, X)((\square\phi)^3 + 2\phi_{;\mu}^\nu\phi_{;\nu}^\mu - 3\phi_{;\mu\nu}\phi^{;\mu\nu}\square\phi), \end{aligned}$$

where $G_{i,X} = \partial G_i / \partial X$.

and $S_{(m)}$ is the total matter action. Without the presence of this last term, the equation of motion for the scalar field is $\square\phi = V_{,\phi}$. The minimal coupling to matter contributes such that $\square\phi \supset -A^3 A_{,\phi} \tilde{T}_{(m)}$, where $\tilde{T}_{(m)} = {}^{(m)}\tilde{T}_{\mu\nu} \tilde{g}^{\mu\nu}$ is the trace of the Jordan-frame matter SE tensor [15, 31]. In particular,

$$\square\phi = V_{,\phi}(\phi) - A^3(\phi) A_{,\phi}(\phi) \tilde{T}_{(m)}. \quad (3.10)$$

We model the matter content as non-interacting, perfect fluids indexed s with equation-of-state parameter w_s such that the trace becomes $\tilde{T}_{(m)}|_{\text{p.f.}} = \sum_s (3w_s - 1)\tilde{\rho}_s$. We have $\tilde{\rho}_s \propto (Aa)^{-3(1+w_s)} \equiv A^{-3(1+w_s)}\rho_s$, where $\rho_s = a^{-3(1+w_s)}$ defines a scaled energy density, conserved in the Einstein frame, and a is the Einstein-frame scale factor. Now

$$\square\phi = V_{,\phi}(\phi) - A_{,\phi}(\phi) \sum_s A^{-3w_s}(\phi) (3w_s - 1)\rho_s, \quad (3.11)$$

which for near-constant ρ_s reduces to $\square\phi = V_{\text{eff},\phi}$ where [31]

$$V_{\text{eff}} = V(\phi) + \sum_s A^{1-3w_s}(\phi) \rho_s \quad (3.12)$$

is the effective potential.

Review

Matter particles in the Jordan frame obey the simple geodesic equation as there is no coupling to ϕ . On the other hand, particles in the Einstein frame matter sector experience a **fifth force** due to the universal coupling. The fifth-force concept captures the non-trivial right-hand side of in the geodesic equation,

$$\frac{d^2x}{dt^2} \supset \frac{\mathbf{F}_5}{m} = -\frac{\beta}{M_{\text{Pl}}} \nabla\phi. \quad (3.13)$$

Thus, β is a measure of the strength of the fifth force relative to the Newtonian gravitational force.

The dynamic, effective equation-of-state parameter is

$$w_{(\phi)} = \frac{p_{(\phi)}}{\rho_{(\phi)}} = \frac{\frac{1}{2a^2}\dot{\phi}^2 - V(\phi)}{\frac{1}{2a^2}\dot{\phi}^2 + V(\phi)}, \quad (3.14)$$

for which $\lim_{\phi \rightarrow 0} w_{(\phi)} = w_\Lambda = -1$. These models are thus often proposed in context of dark-energy models to explain the accelerated cosmic expansion. We will not consider this directly in this project.

3.2.2 Asymmetron model

The particular scalar-field model characterised by the symmetric Mexican-hat potential

$$V(\phi) = \frac{\lambda}{4}\phi^4 - \frac{\mu^2}{2}\phi^2 + V_0 \quad (3.15)$$

is called the **symmetron** model [31]. This theory is invariant under reflection, $\phi \rightarrow -\phi$.⁶ Not equally well-established is the generalisation of this model called the **asymmetron** [47], in

⁶See Peskin & Schroeder [48, Chapters 11, 12, 20 & 22] or Kolb [37, Chapter 7] for discussion on quantum corrections.

which the potential is given an additional cubic term, $V(\phi) \supset -\kappa\phi^3/3$. Here, one of the domains is favoured over the other.

Now, why would we want this asymmetry in the first place? It complicates things by breaking the \mathbb{Z}_2 -degeneracy of the symmetron, so the theory only holds approximately. However, this asymmetry can aid in overcoming the domain wall problem, manifest in the inevitable biased domain wall collapse. We mentioned this briefly in Section 3.1.2. We stress that introducing asymmetry in this way is different from energy bias in the sense that not only is the energy in the two domains different, but the expectation values for ϕ are shifted.

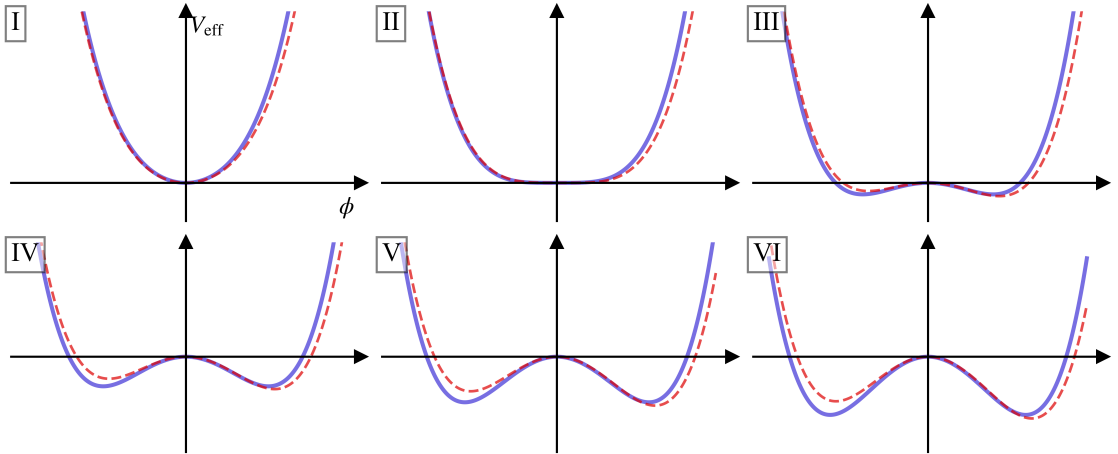


Figure 3.2: The evolution of the (a)symmetron effective potential in (dashed red) solid blue. *Panel I*: The potential before SSB, *panel II*: at SSB, and *panels III–VI*: after SSB, with diluting density.

The simplest (a)symmetron model has the quadratic coupling

$$A(\phi) = 1 + \frac{1}{2} \left(\frac{\phi}{M} \right)^2 + \mathcal{O}\left((\phi/M)^4\right). \quad (3.16)$$

We consider the matter content to be dust-like, so that $\tilde{T}_{(m)} \simeq -\tilde{\rho}_{(m)}$. The effective potential is then given by [31]

$$V_{\text{eff}}(\phi) = \frac{\lambda}{4}\phi^4 - \frac{\kappa}{3}\phi^3 + \frac{\mu^2}{2} \left(\frac{\rho_{(m)}}{\mu^2 M^2} - 1 \right) \phi^2 + V_0, \quad (3.17)$$

up to an irrelevant constant. This potential becomes unstable when (or where) $\rho_{(m)} \leq \mu^2 M^2 \equiv \rho_*$, and the field rolls into either of the two vacua. We call ρ_* the *critical density*. From the cosmological perspective, ignoring κ , we imagine an initially dense region in the universe where a scalar field oscillates slightly around zero. The energy density dilutes and eventually reaches the critical density ($\rho_{(m)} = \rho_*$), spontaneously breaking the \mathbb{Z}_2 symmetry, and separates the scalar field into domains according to their sign at the time. A schematic of this evolution is shown in Fig. 3.2. The potential barriers created at this *phase transition* correspond to the topological solitons discussed in Section 3.1.2; namely cosmic domain walls.

Let $v \equiv \rho_{(m)}/\rho_* = \rho_{(m)}/(\mu^2 M^2)$. By setting $V_{\text{eff},\phi} = 0$, we find the vacuum expectation values (VEVs)

$$\phi_0 = 0 \quad \vee \quad \phi_{\pm} = \phi_{\infty} \left(\bar{\kappa} \pm \sqrt{\bar{\kappa}^2 + 1 - v} \right), \quad (3.18)$$

where we defined $\bar{\kappa} = \kappa/(2\mu\sqrt{\lambda})$ and $\phi_{\infty} = \mu/\sqrt{\lambda}$. Note that the (real) VEV is zero before SSB for the symmetron ($\kappa = 0$). We determine the stability of these minima by evaluating $V_{\text{eff},\phi\phi}$ at $\phi = \phi_0, \phi_{\pm}$ and see that ϕ_0 remains stable until $\rho_{(m)} = \rho_*$, and for $\rho_{(m)} \leq \rho_*$, ϕ_{\pm} are stable.

Screening

In this context, a **screening mechanism** is a property of the model that removes the effect of the extra scalar field in the appropriate environment. The symmetron scalar field mediates fifth forces in low-density environments while being screened in dense regions. We illustrate this in Fig. 3.3.

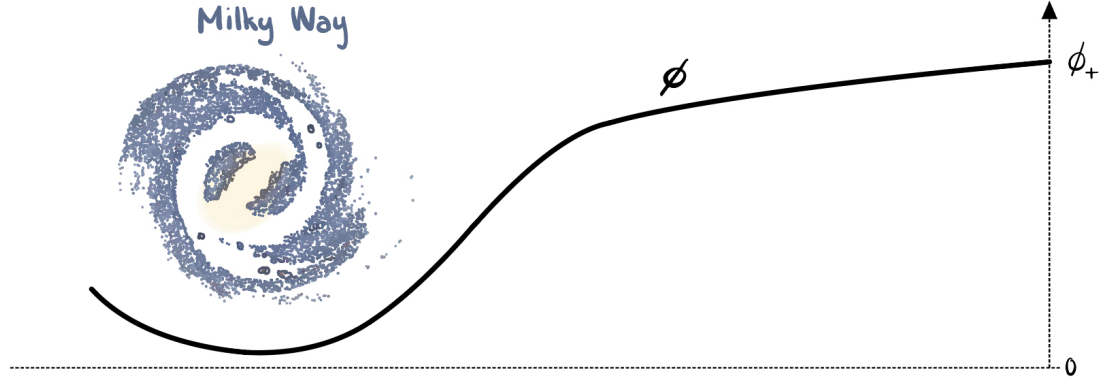


Figure 3.3: Schematic of the symmetron screening mechanism. It is clear that the vacuum expectation value goes to zero in dense regions. This example assumes a symmetron with Compton length scale $L_C \sim \mathcal{O}(\text{kpc})$ [10]. Illustration based on Christiansen [13].

Free parameters

The quartic coupling constant λ measures the scalar self-interactions and μ defines the bare mass of the (a)symmetron. The cubic coupling κ is a measure of the difference between the two vacua, and is zero in the symmetron case. The constant V_0 can be interpreted as a cosmological constant Λ [15], but we will not discuss this here. The conformal coupling scale M governs the matter coupling strength [10]. We introduce the **symmetron Compton wavelength**

$$L_C \equiv \frac{1}{\sqrt{2}\mu} \quad (3.19)$$

which defines the range of the symmetron forces.⁷ Local tests of gravity require $M \lesssim 10^{-3} M_{\text{Pl}}$ for the quadratic coupling [10, 29, 30, 31]. This is to say that fifth forces is mediated within a range $L_C \lesssim \text{Mpc}$ [30].

⁷Note that some references consider the dynamical quantity $L_C \sqrt{1 - \nu}$ to be the symmetron Compton wavelength, which is the actual dynamical range of the symmetron.

Part II

Methodology

Chapter 4

Imperfect Defects

Any cosmologically relevant domain wall will be thin compared to the horizon [50]. Are they sufficiently thin so that the thin-wall approximation holds? If so, we should be able to study the dynamics of such walls by viewing them as $(2 + 1)$ -dimensional timelike hypersurfaces in a spacetime of $3 + 1$ dimensions. By Nambu–Goto theory and an action principle, one can derive an equation governing the dynamics of this worldsheet [55]. In fact, this is the same for any hypersurface of d dimensions, thus relevant for several types of defects. In particular, this concerns the codimension-one defects, as higher-codimension defects cannot generally be thought of as hypersurfaces, but submanifolds in any case [54].

To substantiate the applicability of this theory, we begin in a more general picture than what we eventually will require. We consider a d -dimensional timelike ($\varsigma = +1$ in Eq. (2.8)) submanifold Σ embedded in a smooth pseudo-Riemannian n -dimensional manifold \mathcal{M} . We let Σ have codimension one ($d = n - 1$) and split the ambient space into two separate hypervolumes. Now, Σ is a timelike hypersurface of \mathcal{M} that can be interpreted as the d -dimensional analogue of an infinitely thin domain wall.

We will use this to explore the dynamics of domain walls in the thin-wall limit, where the emphasis is not on the symmetry-breaking scalar field ϕ , but of the position and evolution of the domain wall itself. There exist analytical solutions to the equation of motion for linear perturbations to the *planar* wall position in expanding spacetime. We derive this equation for conventional, static walls and propose a version of this applicable to the defect during phase transition (when the surface energy density is changing).

Now, static, symmetric walls do not produce gravitational radiation by themselves. We will use the dynamics of a wiggly domain wall as source to tensorial metric perturbations, a.k.a. gravitational waves.

The chapter is outlined as follows. In Section 4.1 we review the general formula for dynamics of topological defects. In Section 4.2 we look at domain walls in a general spacetime, as well as perturbations to planar domain walls in an FLRW universe. We implement the symmetron description of these walls in Section 4.3 and solve the linear perturbation in a matter-dominated universe. In Section 4.4 we review the gravitational waves sourced by the Nambu–Goto stress–energy tensor.

4.1 Formal treatment of defect dynamics

In this fairly technical section we follow Garriga & Vilenkin [26] and Ishibashi & Ishihara [34]. In mathematical terms, we consider a smooth spacetime

$$\mathcal{M} = (\mathbb{R}^{n-1,1}, g_{\mu\nu}) \supset \Sigma = (\mathbb{R}^{d-1,1}, \gamma_{ab}) \quad (4.1)$$

where $d = n - 1$ and indices $a, b, c = 0, 1, \dots, d - 1$, while Greek indices as usual runs from 0 to $n - 1$. Let the world sheet Σ divide \mathcal{M} into two hypervolumes \mathcal{M}_\pm such that $\mathcal{M} = \mathcal{M}_+ \cup \Sigma \cup \mathcal{M}_-$. We invoke a smooth coordinate system $\{x^\mu\}$ of the spacetime in a neighbourhood of Σ . The embedding of Σ in \mathcal{M} is $x^\mu = X^\mu(\xi^a)$, where the coordinate system $\{\xi^a\}$ parametrises Σ . The induced metric on Σ is

$$\gamma_{ab} = g_{\mu\nu} e_a^\mu e_b^\nu; \quad e_a^\mu \equiv X^\mu,_a = \partial X^\mu / \partial \xi^a. \quad (4.2)$$

Here, e_a^μ are the tangent vectors and n^μ the unit-normal vector pointing from Σ to \mathcal{M}_+ , obeying

$$g_{\mu\nu} n^\mu n^\nu = 1 \quad \text{and} \quad g_{\mu\nu} e_a^\mu n^\nu = 0. \quad (4.3)$$

The action for the system is [34]

$$S = -\sigma \int_\Sigma d^d\xi \sqrt{-\gamma} - v_+ \int_{\mathcal{M}_+} d^n x \sqrt{-g} - v_- \int_{\mathcal{M}_-} d^n x \sqrt{-g}. \quad (4.4)$$

The first term is called the Nambu–Goto action S_{NG} , with σ representing the constant positive energy density of the defect in its rest frame. The rest is the vacuum action S_{vac} given through the constant potential energy densities v_\pm of \mathcal{M}_\pm .

Let us consider the variation of S under small changes in the world sheet, $X^\mu \rightarrow X^\mu + \delta X^\mu$. Since only transverse motion is physically relevant, we can write the variation in terms of the small, but otherwise arbitrary, function $\psi(\xi^a)$;

$$X^\mu \rightarrow X^\mu + \psi n^\mu. \quad (4.5)$$

The equation of motion for the normal coordinate is then [26, 34]

$$n_\mu \widehat{\square} X^\mu + n_\mu \Gamma_{\kappa\tau}^\mu \gamma^{ab} X^\kappa,_a X^\tau,_b + \frac{v}{\sigma} = 0, \quad (4.6)$$

where $v = v_+ - v_-$ is the difference in vacuum energies,

$$\widehat{\square} = \widehat{\nabla}^a \widehat{\nabla}_a = \frac{1}{\sqrt{-\gamma}} \partial_a (\sqrt{-\gamma} \gamma^{ab} \partial_b) \quad (4.7)$$

is the d'Alembertian associated with Σ , and $\Gamma_{\kappa\tau}^\mu$ are the spacetime Christoffel symbols. This can be written in the simple form

$$\gamma^{ab} \widehat{K}_{ab} = -\frac{v}{\sigma}, \quad (4.8)$$

where the extrinsic curvature tensor (Eq. (2.9)) is $\widehat{K}_{ab} = -e_a^\mu e_b^\nu \nabla_\nu n_\mu$.

Minkowski. In Garriga & Vilenkin [26] it is shown that a planar domain wall oriented perpendicular to the z axis in Minkowski space follows the trajectory $z = z(t)$ whose equation of motion is

$$\frac{z_{,tt}}{(1 - z_{,t}^2)^{3/2}} = \frac{v}{\sigma}. \quad (4.9)$$

With $v = 0$ the solution is $z(t) = 0$ in a suitable Lorentz frame. With non-degenerate vacua, the solution is the hyperbola [26].

4.1.1 Linearised perturbations

Let X^μ solve the equation of motion for the defect. We denote the perturbed solution \dot{X}^μ . Only transverse motion is physically observable, and so

$$\dot{X}^\mu = X^\mu + \delta X^\mu = X^\mu + \epsilon(\xi^a) n^\mu, \quad ^1 \quad (4.10)$$

where the wall displacement variable ϵ is a linear perturbation ($\epsilon^2 \simeq 0$), and n^μ is the unit-normal of the *unperturbed* worldsheet [55]. To find the equation of motion for ϵ we apply Eq. (4.10) to Eq. (4.8) and solve order by order. If the ambient space is Minkowski, this amounts to [26]

$$\widehat{\square}\epsilon + \widehat{K}^{ab}\widehat{K}_{ab}\epsilon = 0; \quad g_{\mu\nu} = \eta_{\mu\nu}. \quad (4.11)$$

4.1.2 Energy and momentum

From the Nambu–Goto action S_{NG} , we can construct an effective energy–momentum tensor associated with the defect

$$T^{\mu\nu}\Big|_{\text{NG}} = \frac{2}{\sqrt{-g}} \frac{\delta S_{\text{NG}}}{\delta g_{\mu\nu}}. \quad (4.12)$$

Consider $X^\mu = \xi^a e_a^\mu + X_\perp n^\mu$. By rewriting the action to the spacetime integral

$$S_{\text{NG}} = -\sigma \int_{\mathcal{M}} d^m x \sqrt{-\gamma} \delta(r); \quad r \equiv n_\mu x^\mu - X_\perp, \quad (4.13)$$

where the Dirac delta function essentially eliminates any spacetime event that is *not* the defect. The variation $g_{\mu\nu} \rightarrow g_{\mu\nu} + \delta g_{\mu\nu}$ gives [54, 55]

$$T^{\mu\nu}\Big|_{\text{NG}} = \frac{\sigma}{\sqrt{-g}} \int d^d \xi \sqrt{-\gamma} \gamma^{ab} X^\mu{}_{,a} X^\nu{}_{,b} \delta(r), \quad (4.14)$$

or equivalently

$$T^{\mu\nu}\Big|_{\text{NG}} = \frac{\sigma \delta(r)}{\sqrt{-g} \sqrt{-\gamma}} \frac{\delta \gamma}{\delta g_{\mu\nu}}. \quad (4.15)$$

4.2 Domain-wall dynamics

So far, we have addressed the very general Nambu–Goto picture. From here, we turn our attention to (2+1)-dimensional submanifolds living in (3+1)-dimensional spacetime, i.e. domain walls. Let $v = v_+ - v_- = 0$. We describe the wall position in \mathcal{M} with $x^\mu = X^\mu(\xi^a)$ where $\mu = 0, 1, 2, 3$ and $a = 0, 1, 2$, and impose coordinates that satisfy

$$ds^2 = dY^2 + \gamma_{ab} d\xi^a d\xi^b, \quad (4.16)$$

where Y is the normal distance Σ [55]. With Eq. (4.2) and the identity $\delta \gamma = \gamma \gamma^{ab} \delta \gamma_{ab}$, we obtain [55]

$$\widehat{\square}X^\mu + \Gamma_{\kappa\tau}^\mu \gamma^{ab} X^\kappa{}_{,a} X^\tau{}_{,b} = 0, \quad (4.17)$$

which is a repetition of Eq. (4.6) with degenerate vacua. According to Vilenkin & Shellard [55], to the best of the authors’ knowledge, no known gauge choice can reduce Eq. (4.17) to an exactly solvable linear equation. If X^μ is a known solution, we can study a linear perturbation to this instead, with the perturbed wall trajectory in Eq. (4.10).

¹Formally, this is the same as the variation above, but now we are dealing with a physical perturbation as opposed to a mathematical variation.

4.2.1 Planar walls in expanding spacetime

Assume we have the unperturbed wall parallel to the xy -plane of an expanding spacetime

$$ds^2 = a^2 ds^2|_M = a^2(-d\tau^2 + dx^2), \quad (4.18)$$

where $\mathbf{x} = (x, y, z)$ are the comoving Cartesian coordinates. We fix the gauge $\xi^a = (\tau, x, y)$ so that $z = z_w = z_0 + \epsilon(\tau, x, y)$ uniquely describes the wall motion. The Nambu–Goto action reads

$$S_{NG} = -\sigma \int d^3\xi \sqrt{-\gamma} = -\sigma \int d\tau a^3(\tau) \int dx \int dy h(\tau, x, y) \quad (4.19)$$

where

$$h \triangleq a^{-3} \sqrt{-\gamma} = \sqrt{1 + \epsilon^a \epsilon_{,a}}. \quad (4.20)$$

The equation of motion for the wall becomes [55]

$$-\partial^a(\epsilon_{,a}/h) + 3\mathcal{H}\epsilon_{,\tau}/h = 0, \quad (4.21)$$

where $\mathcal{H} = a_{,\tau}/a$ is the conformal Hubble factor. We let ϵ be a linear perturbation such that $\epsilon^2 \rightarrow 0$ and consider power-law expansion, $a \propto \tau^\alpha$. Now,

$$\epsilon_{,\tau\tau} + 3\mathcal{H}\epsilon_{,\tau} - \epsilon_{,xx} - \epsilon_{,yy} = 0 \quad (4.22)$$

is the equation for the first-order displacement field. This is a separable partial differential equation (PDE) and we assume solutions of the form $\epsilon(\tau, x, y) = \varepsilon(\tau)\mathcal{E}(x, y)$. Now, we separate Eq. (4.22) into

$$\ddot{\varepsilon} + \mathcal{D}(\tau)\dot{\varepsilon} + p^2\varepsilon = 0 \quad \text{and} \quad \mathcal{E}_{,xx} + \mathcal{E}_{,yy} + p^2\mathcal{E} = 0, \quad (4.23)$$

where $\mathcal{D}(\tau) = 3\mathcal{H}(\tau)$. The spatial part has solutions that are linear combinations of $\sin(p_x x + p_y y)$ and $\cos(p_x x + p_y y)$, with $p_x^2 + p_y^2 = p^2$. The solutions to this equation are of the form $\varepsilon = (p\tau)^\nu Z_\nu(p\tau)$ with $\nu = (1 - 3\alpha)/2$ (see Appendix A, Eq. (A.2)).

Energy and momentum

To some extent, we can account for a possibly non-vanishing thickness $l \sim \delta$ by choosing a Gaussian function instead of a Dirac delta distribution. Simply substituting

$$\delta(r) \rightarrow \Phi_l(r) \equiv \frac{1}{\sqrt{2\pi}l} \exp\left\{-\frac{r^2}{2l^2}\right\} \quad (4.24)$$

in Eq. (4.15) does the trick, and restores $\delta(r)$ in the limit where $l \rightarrow 0$. This is understood in context with Section 3.1.2, where we argue that $l = \delta/\sqrt{2}$ gives a suitable Gaussian profile. Note that this is not the same as going beyond the thin-wall limit, but rather an approximation that includes a thickness that is small enough to not alter the dynamics. Domain walls of cosmological relevance will have thickness much smaller than the horizon [26]. However, some models will have instances in time when this is not true, and the thickness in fact varies [30].

We perform the variation in Eq. (4.15) for the scenario in question in Appendix C.3, to find the SE tensor associated with the wall motion. The non-vanishing spatial components are

$$\begin{aligned} W_{AB} &= -a\sigma\Phi_l(z - z_w) \cdot \delta_{AB}, \\ W_{(A3)} &= -a\sigma\Phi_l(z - z_w) \cdot \epsilon_{,A}, \end{aligned} \quad (4.25)$$

where indices $A, B = 1, 2$ and $z_w = z_0 + \epsilon$. The tensor $W^{\mu\nu}$ refers to the stress–energy tensor associated with a particular domain wall by Eq. (4.15).

4.2.2 Time-dependent surface tension

Until now, the theory is model-independent in the sense that we have not assumed any particular type of domain wall (or defect, in general). This dependence is encoded in the *constant* surface tension σ and difference in vacuum energies $v = v_+ - v_-$. It is plain to see from Eq. (4.8) that the absence of energy bias removes the surface-tension dependence. But what if the surface tension is not constant?

If we allow the surface tension to vary, $\sigma = \sigma(\tau)$, we need to put this inside of the integral in the Nambu–Goto action in Eq. (4.19). The calculation is presented in Appendix C.2. We immediately see that this is equivalent to letting $a^3 \rightarrow a^3\sigma$, which amounts to

$$\mathcal{D}(\tau) = \frac{3}{a\sigma^{1/3}} \frac{da\sigma^{1/3}}{d\tau} = 3\frac{\dot{a}}{a} + \frac{\dot{\sigma}}{\sigma} = 3\frac{d\ln a}{d\tau} + \frac{d\ln\sigma}{d\tau} \quad (4.26)$$

in Eq. (4.23). We get

$$\ddot{\varepsilon} + (3\dot{a}/a + \dot{\sigma}/\sigma)\dot{\varepsilon} + p^2\varepsilon = 0. \quad (4.27)$$

This extra term will introduce the model-dependence since the surface tension is given by (see Appendix C.1)

$$\sigma \simeq \int_{\phi_-}^{\phi_+} d\phi \sqrt{2V_{\text{eff}}(\phi) - 2V_{\text{eff}}(\phi_\pm)}, \quad (4.28)$$

where $V_{\text{eff}}(\phi)$ is the effective potential of the scalar field theory.

4.3 Symmetron walls

The symmetron effective potential in Eq. (3.17) is designed to induce phase transition at conformal time τ_* , or scale factor a_* . Inserting this into Eq. (4.28), we find in Appendix C.1 that the surface tension of a thin symmetron domain wall is

$$\sigma = \sigma_\infty(1 - v)^{3/2}; \quad v = (a_*/a)^3, \quad (4.29)$$

where σ_∞ is the vacuum surface energy density (Eq. (3.7)).

From here it becomes advantageous to introduce some new, dimensionless variables. We will use $s \equiv \tau/\tau_*$ as our time variable, and $\omega \equiv p\tau_*$ as the eigenvalue, when it comes to that. In a universe with $a = a_*s^\alpha$ we have $v = s^{-3\alpha}$ and thus

$$\frac{\sigma'}{\sigma} = \frac{d\ln\sigma}{ds} = \frac{9\alpha}{2s(s^{3\alpha} - 1)}, \quad (4.30)$$

where primes mean derivatives with respect to s . Finally, the equation of motion for the scalar perturbation to the wall normal coordinate is

$$\varepsilon'' + \left(\frac{3\alpha}{s} + 2d(s) \right) \varepsilon' + \omega^2 \varepsilon = 0; \quad d(s) \triangleq \frac{9\alpha}{4s(s^{3\alpha} - 1)}. \quad (4.31)$$

4.3.1 Solution in matter-dominated universe

This work only truly experiments in a universe with, and only with, homogeneous matter distribution, i.e. $\alpha = 2$ and $\sum_s \Omega_{s0} = \Omega_{m0} = 1$. Generalisation of the following to other α should in principle be trivial, but at some point in the following we require $\alpha \geq 1/3$, and so a different analysis would be required for smaller α .

Restricting our discussion to $\alpha = 2$, we continue with the planar domain wall placed parallel to the xy -plane, spontaneously formed at symmetry breaking, $s = 1$. Assume an initial perturbation of amplitude ε_* was given to the wall. We consider the solution to Eq. (4.31) that has eigenvalue $\omega = p\tau_*$ and restrict $\max |\mathcal{E}(x, y)| = 1$ for the spatial part. With initial conditions $\varepsilon(s = 1) = \varepsilon_*$ and $\varepsilon'(s = 1) = 0$, we shall solve

$$\varepsilon'' + \left(\frac{6}{s} + \frac{9}{2s(s^6 - 1)} \right) \varepsilon' + \omega^2 \varepsilon = 0 \quad (4.32)$$

analytically in two regimes, and sow these solutions together in the region where they overlap. For notational ease, we write $\varepsilon(s) = \varepsilon_* e(s)$.

Shortly after symmetry breaking. We begin by solving the equation of motion for $s \sim 1$. As our equation has a singularity at $s = 1$, the natural way to go is through a Laurent expansion around this point of the damping term in Eq. (4.32). We find

$$\frac{6}{s} + \frac{9}{s(s^6 - 1)} = \frac{3}{2}(s - 1) + \frac{3}{4} + \frac{29}{8}(s - 1) - \frac{93}{16}(s - 1)^2 + \mathcal{O}((s - 1)^3). \quad (4.33)$$

Now $e(s)$ is also subject to an expansion around $s = 1$:

$$e^{(I)}(s) = [1 + c_1(s - 1) + c_2(s - 1)^2 + c_3(s - 1)^3 + \dots]. \quad (4.34)$$

When put together, we get a polynomial in $(s - 1)$ on the left-hand side of Eq. (4.32), for which all coefficients must vanish. We solve the system of equations for $\{c_1, c_2, c_3\}$ and find

$$e^{(I)}(s) = \left[1 - \frac{\omega^2}{5}(s - 1)^2 + \frac{\omega^2}{35}(s - 1)^3 \right] + \mathcal{O}((s - 1)^4). \quad (4.35)$$

Adiabatic evolution. The extra damping term $2d(s)$ initially changes extremely rapidly from very large values, before it becomes very small compared to $6/s$. We expect the solution to quickly approach that of Eq. (4.23) as $s \gg 1$. Said damping term is not completely negligible, however, as it causes a *damping envelope* that is considered much like in the case of a damped harmonic oscillator. We write

$$e^{(II)}(s) \simeq \zeta(s) \cdot \exp \left\{ - \int^s dt d(t) \right\}. \quad (4.36)$$

Employing this ansatz in the equation of motion gives

$$\zeta'' + \frac{6}{s} \zeta' + (\omega^2 - \theta(s)) \zeta = 0; \quad \theta(s) \triangleq d'(s) + d^2(s) + \frac{6}{s} d(s), \quad (4.37)$$

whose solution is $\zeta(s) \simeq s^{-5/2} Z_{-5/2}(\omega s)$ when the phase shift introduced by $\theta(s)$ is negligible.² Now, we find that $\exp \left\{ - \int^s dt d(t) \right\} = s^{9/2} (s^6 - 1)^{-3/4} \cdot \text{constant}$. Thus,

$$e^{(III)}(s) \simeq \frac{A J_{-5/2}(\omega s) + B Y_{-5/2}(\omega s)}{s^{5/2}} \frac{s^{9/2}}{(s^6 - 1)^{3/4}}, \quad (4.38)$$

where A and B are constants to be determined.

²In fact, it is possible to show that $\lim_{\omega \rightarrow \infty} [\sqrt{\omega^2 - \theta(1 + \omega^{-1})} - \omega]/\omega = \sqrt{19}/4 - 1 \approx 0.09$.

Complete evolution. We use a computer algebra system, namely *SageMath* [53], to determine A and B from the system of equations

$$\begin{aligned} e^{(I)}(s = s_{\text{sow}}) &= e^{(II)}(s = s_{\text{sow}}), \\ e^{(I)\prime}(s = s_{\text{sow}}) &= e^{(II)\prime}(s = s_{\text{sow}}), \end{aligned} \quad (4.39)$$

where we choose $s_{\text{sow}} = 1 + \omega^{-1}$, since only sub-horizon modes, $\omega \gg 1$, are of interest. Now,

$$\varepsilon(s) = \varepsilon_* \cdot \begin{cases} e^{(I)}(s) & \text{if } s \leq s_{\text{sow}}, \\ e^{(II)}(s) & \text{if } s \geq s_{\text{sow}}, \end{cases} \quad (4.40)$$

where the coefficients are given in Appendix C.2.1, Eq. (C.15). In Fig. 4.1 we demonstrate how this solution looks like for arbitrary ω , in the different steps described above.

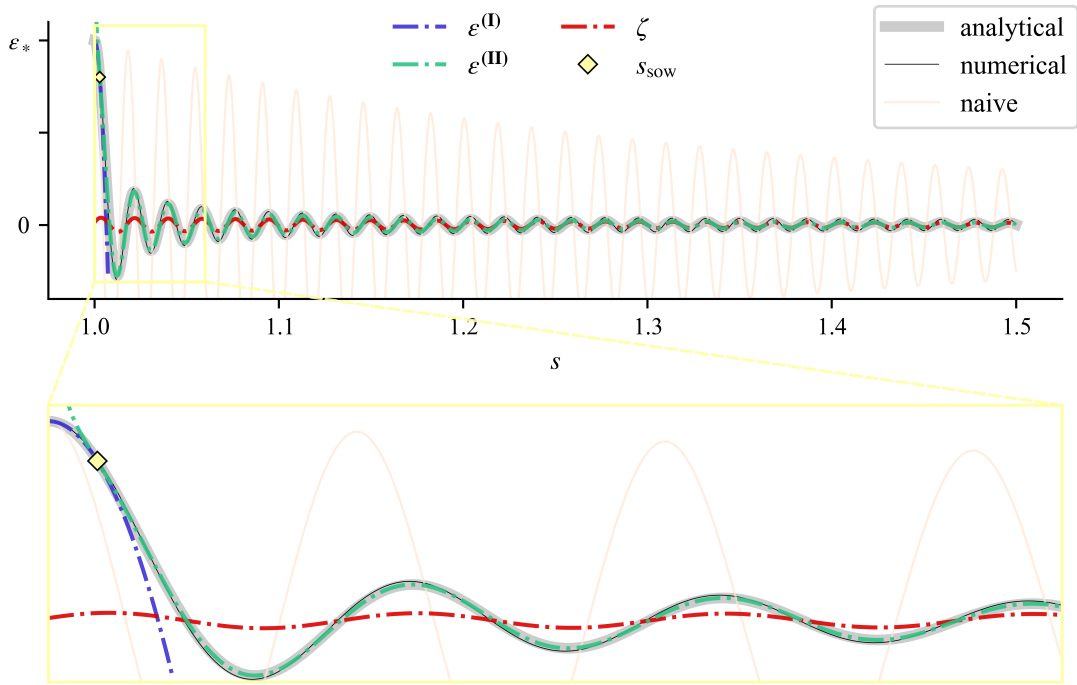


Figure 4.1: Demonstration of how the analytical solution to the equation of motion for $\varepsilon(s)$ was obtained. The numerical solution is included, both in the case with constant (“naive”) and time-varying (numerical) surface tension.

Review

We see that the initial amplitude ε_* can be factored out and does not affect the evolution of the wall. However, we need to keep in mind that this should be small enough to satisfy $(\varepsilon_*/\tau_*)^2 \simeq 0$.

We ignore x -dependence in ε and impose Dirichlet boundary conditions $\mathcal{E}(y = 0) = \mathcal{E}(y = \tau_*) = 0$. We write the complete solution in terms of eigenvalues $p^{(n)} = \pi n / \tau_*$,

$$\varepsilon(\tau, y) = \varepsilon_* \sum_{n=0}^{\infty} \{a_n F_a(s; \pi n) + b_n F_b(s; \pi n)\} \sin(p^{(n)} y); \quad \max \varepsilon(\tau_*, y) = \varepsilon_*, \quad (4.41)$$

where $F_{a,b}(s; \omega^{(n)})$ are the linearly independent solutions to Eq. (4.32). This makes $\varepsilon = \varepsilon(\tau) \sin p y$ a simple solution to the full equation, where ε solves Eq. (4.32).

4.4 From domain wall wiggles to spacetime ripples

Static, planar domain walls do not themselves produce gravitational radiation. Introducing asymmetry to the system, as we do when adding perturbations, can give rise to non-vanishing stress-energy tensor components in the TT gauge. In this section we present the gravitational-wave calculations in the case of a planar, thin domain wall in a conformally flat universe with expansion rate a . We neglect back-reaction, that is we assume that the defect does not change the unperturbed background metric.

4.4.1 Gravitational waves in expanding universe

From Section 2.4.1 we have the calculation of $\tilde{h}_{ij}(\tau, \mathbf{k})$ in a universe with $a \propto \tau^\alpha$, specified for $\alpha \in \mathbb{Z}$. Assuming homogeneous initial conditions at $\tau_i = \tau_*$, the tensor perturbations are given by Eq. (2.50) and Eq. (2.49) with $n = \alpha - 1$. For convenience, we use a linear polarisation basis (see Section 2.4) and the decomposition $\tilde{\psi}_P = a\tilde{h}_P = H_P^1 + H_P^2$, $P = +, \times$, such that [36]

$$H_P^{1,2}(\tau, \mathbf{k}) = \pm R_n^{(1,2)}(k\tau) \int_{\tau_*}^{\tau} d\hat{\tau} R_n^{(2,1)}(k\hat{\tau}) f_P(\hat{\tau}, \mathbf{k}). \quad (4.42)$$

The function f_P , given in Eq. (2.47), contains the TT-projected, Fourier-transformed stress-energy tensor. The conformal time derivative $\dot{\psi} = \dot{H}_P^1 + \dot{H}_P^2$ is given by

$$\dot{H}_P^{1,2}(\tau, \mathbf{k}) = \pm k \left[R_\alpha^{(1,2)}(k\tau) - n z_n^{(1,2)}(k\tau) \right] \int_{\tau_*}^{\tau} d\hat{\tau} R_n^{(2,1)}(k\hat{\tau}) f_P(\hat{\tau}, \mathbf{k}). \quad (4.43)$$

Note that $\dot{h} = a^{-1}(\dot{\psi} - \dot{a}\psi)$ is the conformal time derivative of the gravitational waves. We repeat that $R^{(i)}$ and $z^{(i)}$ are the Riccati- and spherical Bessel functions of i th kind, respectively, reported in Appendix A.

4.4.2 Fourier-space stress-energy tensor

In Section 4.2 we found that the SE tensor of a thin domain wall in an expanding universe looks like Eq. (4.25). For the case of a wall in the xy -plane, this reduces to

$$\begin{aligned} W_{ab}(\tau, \mathbf{x}) &= -a(\tau)\sigma_w(\tau)\Phi_l(z - z_w)\eta_{ab}, \\ W_{iz}(\tau, \mathbf{x}) &= -a(\tau)\sigma_w(\tau)\Phi_l(z - z_w)\epsilon_{,i}, \end{aligned} \quad (4.44)$$

where σ_w is the wall's surface tension, $z_w = z_0 + \epsilon(x^a)$ the wall normal coordinate and Φ_l is a Gaussian with standard deviation $l = l_w \triangleq \delta_w/\sqrt{2}$. We go further and look at this quantity in Fourier space:

$$\begin{aligned} \tilde{W}_{ab}(\tau, \mathbf{k}) &= -a(\tau)\sigma_w(\tau)\eta_{ab}\mathcal{D}_w(\tau, k_z) \int d^2x e^{ik_z\epsilon} e^{i(k_x x + k_y y)}, \\ \tilde{W}_{iz}(\tau, \mathbf{k}) &= -a(\tau)\sigma_w(\tau)\mathcal{D}_w(\tau, k_z) \int d^2x \epsilon_{,i} e^{ik_z\epsilon} e^{i(k_x x + k_y y)}, \end{aligned} \quad (4.45)$$

where $\mathcal{D}_w = \exp\{ik_z z_0 - (k_z l_w)^2/2\}$ adjusts for wall width and unperturbed distance from the xy -plane. Let us assume $\epsilon_{,x} = 0$ such that $\epsilon(\tau, x, y) = \epsilon(\tau)\mathcal{E}(y)$. Now

$$\underbrace{\int dy e^{ik_z\epsilon(\tau)\mathcal{E}(y)} e^{ik_y y}}_{\equiv I_s} \quad \text{and} \quad \underbrace{\epsilon(\tau) \int dy \partial_y \mathcal{E} e^{ik_z\epsilon(\tau)\mathcal{E}(y)} e^{ik_y y}}_{\equiv I_a} \quad (4.46)$$

are all we need to solve to have a completely analytic expression for \tilde{W}_{ij} .

We choose a linear polarisation basis (Section 2.4). As there is no dependence on x in real space, there is a proportionality to $\delta(k_x)$ in Fourier space. Considering $\mathbf{k} = (0, k_y, k_z)$ leaves only one degree of freedom, and we see that

$$\tilde{W}_{ij}|_{\text{TT}} = \Lambda_{ij}^{kl} \tilde{W}_{kl} = \sum_{P=+, \times} \tilde{W}_P e_{ij}^P = \tilde{W}_+ e_{ij}^+, \quad (4.47)$$

where detailed expressions are put in Appendix C.3.2. From here, we work with $\tilde{\pi}_+^w = \tilde{\pi}_{xx}^w = a^{-2} \Lambda_{xx}^{ij} \tilde{W}_{ij}$, where

$$a^2 \tilde{\pi}_+^w = \tilde{W}_+ = \frac{k_y}{2k^2} \left\{ k_y \tilde{W}_{xx} + 2k_z \tilde{W}_{xy} \right\}. \quad (4.48)$$

Spatial part

For simplicity, we choose $\mathcal{E}(y) = \sin py$. In Appendix C.3.2 we show that this implies

$$a^2 \tilde{\pi}_+^w = -\frac{k_y^2}{2k^2} \tilde{W}_{xx}. \quad (4.49)$$

The explicit calculation gives

$$\tilde{\pi}_+^w = 2\pi^2 \delta(k_x) (k_y/k)^2 a^{-1} \sigma_w \mathcal{D}_w \sum_{n \in \mathbb{Z}} \delta(k_y + np) J_n(k_z \varepsilon), \quad (4.50)$$

which we use to compute \tilde{h}_+ .

Chapter 5

Cosmic Phase Transitions

Discrete symmetry breakage leads to formation of domain walls [55]. We may apply thin-wall dynamics when the thickness parameter δ is negligible compared to other dimensions of the problem, primarily the horizon size [55]. Otherwise, we must employ the full field theory. During a phase transition in which the dynamics is governed by a reflection-invariant Lagrangian in $3 + 1$ dimensions, the system quickly divides into alternating positive and negative vacuum domains. Separating these are domain walls, which during transition is thinning from initially (as we will see) infinite thickness.¹

In this chapter we attack the field-theoretical approach to describing the motion of domain walls, during and after phase transition. We eventually take leave of one spatial dimension, and so the framework can also describe strings [8]. Previous work [8] has been done on Minkowski background in the static picture. The following analysis assumes a conformally flat, homogeneous and isotropic background, particularly one with scale factor $a \propto \tau^\alpha$. We consider the entire phase transition, i.e. the actual formation of defects, which alters the dynamics in the Nambu–Goto picture. We build up towards simulations of toy scenarios for which we set $\alpha = 2$.

This chapter first, in Section 5.1, presents the scalar-field formulation of the defect and defect formation. We address the code that was used in Section 5.2 and how we design the simulative experiments in Section 5.3. In Section 5.4 we present details about the particular simulations we perform.

5.1 \mathbb{Z}_2 -symmetry breaking

Assume the boson ϕ is responsible for symmetry break at $a = a_*$, when the energy density of the universe is $\rho \simeq \rho_{(m)} = \rho_*$. From Section 3.2.2 we have the symmetron effective potential Eq. (3.17), and the equation of motion for the scalar field $\square\phi = V_{\text{eff},\phi}$ reads

$$-a^{-2}[\ddot{\phi} + 2\mathcal{H}\dot{\phi} - \nabla^2\phi] = \lambda\phi^3 + \mu^2(\nu - 1)\phi, \quad (5.1)$$

where $\nu = \rho_{(m)}/\rho_*$. To solve this highly nonlinear equation we evaluate it in the quasi-static (time derivatives negligible) and spatially asymptotic (spatial gradients ignored) limits separately.

In the rest of the thesis we use the scaled quantities $\chi = \phi/\phi_\infty$, $\phi_\infty = \mu/\sqrt{\lambda}$ and $\chi_\pm = \pm\sqrt{1-\nu}$. Prior to SSB, the scalar field solution is trivial, and so we move on to consider χ from this critical point where the quadratic term turns negative and the \mathbb{Z}_2 symmetry is spontaneously broken. In the following, we only address the regime where $\rho < \rho_*$. In the following, we assume $\rho = \rho_{(m)}$, where $\rho_{(m)}$ is the energy density of the matter fields.

¹Rather a naive extrapolation of the thickness interpretation, in Eq. (5.4).

5.1.1 Quasi-static limit

We can solve

$$\nabla^2 \chi \simeq +\mu^2 \cdot a^2 [\chi^2 - \chi_+^2] \chi \quad (5.2)$$

to obtain the solution in the limit where spatial gradient plays a much larger role than time derivatives. For $a = 1$ and $\chi_+ = 1$ the solution is the canonical soliton from Section 3.1.1. We consider the well-established extension [see e.g. 50] for the corresponding defect in an expanding universe in combination with adjusting for varying minima [41], namely

$$\chi_w(a, z) = \chi_+ \tanh\left(\frac{\chi_+ a z}{2L_c}\right), \quad (5.3)$$

where L_c is the symmetron Compton wavelength (Eq. (3.19)). This scale² signifies the range of the fields in regions where $\rho < \rho_*$ [47].

Basic properties. Consider the conventional \mathbb{Z}_2 wall from Section 3.1.2. Extrapolated to expanding spacetime, we get

$$\sigma_w = \sigma_\infty(1 - v)^{3/2} \quad \text{and} \quad a\delta_w = \delta_\infty(1 - v)^{-1/2} \quad (5.4)$$

as expressions for the comoving thickness δ_w and the surface energy density σ_w , where constants σ_∞ and δ_∞ are given in Eq. (3.7). We derive the former in Appendix C.1, whereas the latter is seen directly from Eq. (5.3).

5.1.2 Asymptotic limit

We let $\pm\check{\chi}$ denote the field values far away from the wall, well inside the positive and negative domains. Here,

$$\ddot{\check{\chi}} + 2\mathcal{H}\dot{\check{\chi}} = -\mu^2 \cdot a^2 [\check{\chi}^2 + v - 1] \check{\chi} \quad (5.5)$$

governs the evolution of the field strength. The trivial solution becomes unstable after phase transition onset, and the field may fall into any of the two vacua, depending on the phase of the a priori fluctuations. Without loss of generality, we take a look at one of the minima. The positive minimum, which was zero at SSB, goes as $\chi_+ = \sqrt{1 - v}$. Now, the rate at which χ_+ moves from its initial value, blows up at the phase transition, but decays rapidly when approaching the limit value. It makes sense to analyse the equation in the (i) non-adiabatic and (ii) adiabatic regimes separately.

The non-adiabatic regime (i) is a short window around phase transition in which the effective potential changes faster than what the dynamics of the scalar field allow. That is to say, the asymptotic field value $\check{\chi}$ cannot possibly hope to follow the system's actual minima χ_\pm . When the scalar catches up, the effective potential changes slower than the field in what we call the adiabatic regime (ii). What happens is that the field rolls towards the minimum and begins to oscillate around it whilst following its slow drift. The oscillation amplitude is decided by the initial conditions of the field.

We know that oscillations in the scalar field can themselves produce gravitational waves [36]. Ideally we would get rid of them completely to not contaminate the gravitational waves sourced by domain walls alone. In addition, these oscillations will to some extent affect the surface tension and thickness of the domain wall in Eq. (5.4). This will in turn alter the equations for ϵ and h_{ij} from the Nambu–Goto theory, making them analytically unsolvable. So we should avoid large oscillations in the scalar field at great cost. We present the protocol for finding the optimal path the field can take to minimise fifth-force oscillations in Appendix B.

²Dynamically and conformally $L_c/(a\chi_+)$.

5.2 Dynamic modelling

As test bed for our theory we use the C++-code `AsGRD` [14];³ an extended version of the massively parallelised relativistic N -body code `gevolution` [2]. `LATfield2` [20] is used as backend to this. We will describe the code in broad terms, and refer to Adamek et al. [2, 3], Christiansen et al. [14, 15, 16], Daverio et al. [20] for more detailed explanations.

Prelude

The general setup is a three-dimensional box of equal side lengths $L_{\#}$ in Mpc/h on a lattice of $N_{\#}^3$ points, giving spatial resolution $\Delta_{\#} = L_{\#}/N_{\#}$. A Cartesian coordinate system defines the comoving coordinate $\mathbf{x} = (x, y, z)$ and wave vector $\mathbf{k} = (k_x, k_y, k_z)$. The mapping from lattice coordinates $\mathbf{n} = (\mathbf{i}, \mathbf{j}, \mathbf{k})$ to comoving is $\mathbf{x} = \mathbf{n} \cdot \Delta_{\#}$, where $\mathbf{i}, \mathbf{j}, \mathbf{k} \in [0, N_{\#} - 1] \in \mathbb{Z}$. Correspondingly in Fourier space, we have lattice coordinates $\tilde{\mathbf{n}} = (\mathbf{u}, \mathbf{v}, \mathbf{w})$, where $\mathbf{u}, \mathbf{v}, \mathbf{w} \in \pm[0, N_{\#}/2 - 1]$, and the mapping $\mathbf{k} = \tilde{\mathbf{n}} \cdot k_{\#}$. Here, $k_{\#} = 2\pi/L_{\#}$ is the fundamental frequency. The box's boundaries are *periodic* which means that for any function $f(\mathbf{n})$, we have

$$f(\mathbf{i}, \mathbf{j}, \mathbf{k}) = f(\mathbf{i} + N_1 L_{\#}, \mathbf{j} + N_2 L_{\#}, \mathbf{k} + N_3 L_{\#}) \quad \forall N_i \in \mathbb{Z}. \quad (5.6)$$

This is to say that the global topology of the spacelike hypersurface is a 3-torus \mathbb{T}^3 [3]. Furthermore, the box is decomposed in rod domains for MPI-parallelisation [20].

The code automatically outputs scalar quantities like extremal values of χ and q , as well as their box-averaged values. Besides this, we request two-dimensional snapshots of the field in question at every-something time step. The file type for the snapshots are Hierarchical Data Format (HDF5). Saving this data is a computational cost, and requires available memory.

Fast Fourier transforms. We write $f(\mathbf{n})$ and its discrete Fourier transform (DFT) $\tilde{f}(\tilde{\mathbf{n}})$ as

$$f(\mathbf{n}) = \frac{1}{N_{\#}^3} \sum_{\tilde{\mathbf{n}}} e^{-2\pi i \tilde{\mathbf{n}} \cdot \mathbf{n} / N_{\#}} \tilde{f}(\tilde{\mathbf{n}}), \quad \tilde{f}(\tilde{\mathbf{n}}) = \sum_{\mathbf{n}} e^{+2\pi i \tilde{\mathbf{n}} \cdot \mathbf{n} / N_{\#}} f(\mathbf{n}). \quad (5.7)$$

The equations are solved using fast Fourier transforms (FFTs), taken care of by the `LATfield2` library [20]. Hermitian symmetry gives

$$\tilde{f}(-\tilde{\mathbf{n}}) = \tilde{f}^*(\tilde{\mathbf{n}}), \quad (5.8)$$

where \tilde{f}^* is the complex conjugate.

Units and conventions. The code measures length in units of $L_{\#}$ and the DFT sign convention is opposite of Eq. (5.7) and without normalisation [3, 20]. We need to adjust for this when comparing results to calculations, e.g. $\tilde{f}|_{\text{calc.}} \leftrightarrow \tilde{f}^*|_{\text{code.}}$

5.2.1 Equations

Perturbations to the FLRW background are evolved in accordance with the linearised Einstein equation.⁴ The tensorial part obeys

$$\ddot{\tilde{h}}_{ij} + 2\mathcal{H}\dot{\tilde{h}}_{ij} + k^2\tilde{h}_{ij} = 2M_{\text{Pl}}^{-2}\tilde{\Pi}_{ij}^{\text{TT}} \quad (5.9)$$

³Code available on <https://github.com/oyvach/AsGRD> (Nov. 2024).

⁴For details, see Adamek et al. [3].

as elaborated in Section 2.4.1. The asymmetron field is evolved in the Einstein frame with the equation

$$\dot{q} = \nabla^2 \chi - a^2 \mu^2 \{ \chi^3 - 2\bar{\kappa} \chi^2 + (\nu - 1) \chi \}, \quad (5.10)$$

where $q \equiv a^2 \dot{\chi} = a^2 d\chi/d\tau$ is the “speed” of the field. As before (Section 3.2.2), μ and $\bar{\kappa} = \kappa/(2\mu \sqrt{\lambda})$ encode the asymmetron parameters.

AsGRD solves discretised versions of these via a numerical-integration protocol chosen by the user. The fourth-order Runge-Kutta scheme and Leap-frog method are amongst the options. The size of the time step $\Delta_\tau^{(\psi)}$ for the solver of the field ψ is given in terms of the Courant factor [16]

$$C_f^{(\psi)} = v_g^{(\psi)} \frac{\Delta_\tau^{(\psi)}}{\Delta_\#}, \quad (5.11)$$

where $v_g^{(\psi)}$ is the group velocity of said field. ψ here represents CDM or ϕ , and we use $v_g^{(cdm)} \sim 0.02$ and $v_g^{(\phi)} = 1$.

5.3 Pilot design

To accurately compare the soliton’s evolution with the Nambu–Goto prediction, it is essential to begin with an initial configuration closely approximating the exact solution to the equations of the full field theory. Without this, any deviations from the Nambu–Goto dynamics might simply result from inaccuracies in the initial setup.

That said, we do not actually have these exact solutions in curved spacetime. However, with sufficient tweaking, we should be able to design our desired scenario in a `gevolution` simulation box. This section elaborates on the specific simulation configuration that is the toy model.

5.3.1 Initial configuration

The purpose of the simulations is to test the applicability of the thin-wall approximation for the wall evolution (Eq. (4.40)) and the corresponding gravitational waves (Section 4.4). Therefore, the simulation setup imitates a toy model, not a realistic scenario. To create this idealised cosmological scenario we initialise the simulation box as described below.

We assume wall profiles of the form

$$\chi_w(a_i, z - z_w) = \check{\chi} \tanh \left(\frac{a \check{\chi}}{2L_c} (z - z_w) \right) \Big|_{a=a_i}, \quad (5.12a)$$

$$q_w(a_i, z - z_w) = a^2 \frac{d\chi_w}{d\tau} \Big|_{a=a_i}, \quad (5.12b)$$

where a , $\check{\chi}$ and z_w generally depends on time, and z_w also on spatial coordinates x and y . Note that with $\check{\chi} = \chi_+$ we get the familiar quasi-static formula in Eq. (5.3). We refer to Appendix B for details.

In an FLRW universe a (semi-)stable symmetron domain wall is approximated Eq. (5.3) (or Eq. (B.8)). To preserve periodic boundary conditions, there needs to be an even number of walls present, where half are walls and the other half are anti-walls.⁵ We choose two, and place the wall of interest at $z_0 = L_\#/2$, and its counterpart at $\bar{z}_0 = 0$, both aligned with the xy -plane.

⁵Made-up term used as the domain-wall analogue of the antikink in Section 3.1.1.

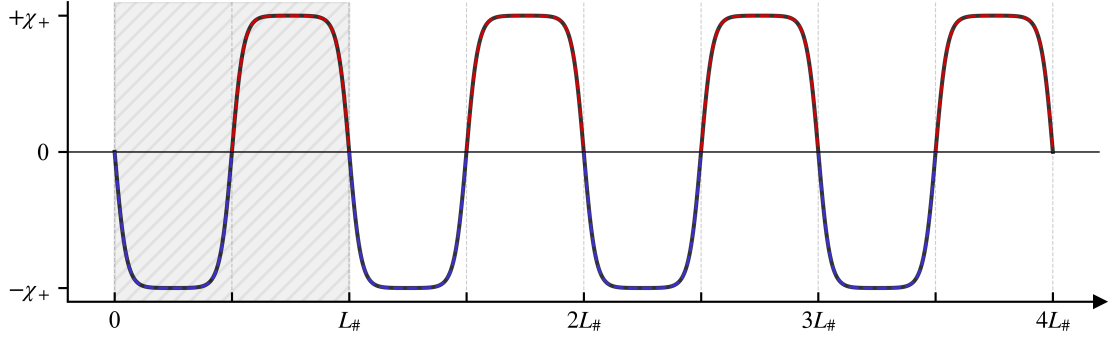


Figure 5.1: Demonstration of the periodicity of $\chi(a_i, z)$ on the lattice. The shaded region represents the box coordinates.

Now say we add a displacement $\epsilon = \epsilon(\tau, x, y)$ to the middle wall. Assuming sufficient spatial separation, the system of defects is given by (see Eq. (3.4))

$$\chi(a, x) = \check{\chi}^{1-2N} \prod_{n=-\infty}^{\infty} \chi_w(a, z - z_w^n) \prod_{m=-\infty}^{\infty} \bar{\chi}_w(a, z - \bar{z}_w^m), \quad (5.13)$$

where

$$z_w^n = z_0 + \epsilon + nL_\# \quad \text{and} \quad \bar{z}_w^m = \bar{z}_0 + mL_\#. \quad (5.14)$$

Figure 5.1 demonstrates how $\chi(a_i, z)$ varies with comoving coordinate z , in the absence of wall perturbation.

Setting the initial conditions on the field $q = a^2 \dot{\chi}$ is a matter of algebra. The expression is cleanest when $\dot{z}_w = \dot{\epsilon} = 0$, i.e. for $a_i = a_*$. See Appendix B.2 for detailed explanation.

Initial time. We need to be careful when choosing the exact redshift to initiate the simulation. Clearly, the conventional expression Eq. (5.3) does not work if we set initial redshift $\beta_1 = \beta_*$. Initiating only a few time steps later allows us to use this after all, but we need to make sure the wall and anti-wall do not collide. Whether this is the case depends on several parameters. Some sets of initial conditions will induce large fifth-force oscillations, and we should try to avoid this.

Using the tweaked initial conditions on the asymptotic fields as boundary conditions on the quasi-static field in Eq. (B.8) opens for the possibility of initialising as close to phase transition as we want. We observe that $\check{\chi}^{\text{ideal}} \rightarrow \chi_+$ after some time, and so another strategy to reduce oscillations is to initialise *after* this non-adiabatic phase. The drawbacks are that we might lose important information about the source of the gravitational waves and that $\dot{z}_w \neq 0$.

5.3.2 Energy and momentum

With this exact setup, we can write the total domain-wall SE tensor on the form $T_{\mu\nu} = \sum_n W_{\mu\nu}^n + \sum_m \bar{W}_{\mu\nu}^m$, i.e. as a sum over the SE tensors associated with each wall and anti-wall. Explicitly,

$$\begin{aligned} T_{ab}(\tau, x) &= -a\sigma\eta_{ab} \sum_n [\Phi_l(z - z_w^n) + \Phi_l(z - \bar{z}_w^n)], \\ T_{iz}(\tau, x) &= -a\sigma \sum_n [\Phi_l(z - z_w^n) \partial_i z_w^n + \Phi_l(z - \bar{z}_w^n) \partial_i \bar{z}_w^n], \end{aligned} \quad (5.15)$$

from Section 4.4.2, with z_w^n and \bar{z}_w^n are given in Eq. (5.14). Here, σ and $\delta = \sqrt{2}l$ refers to the surface tension and thickness of any wall in the system.

Continuous and discrete Fourier space

The Fourier analogue reads

$$\begin{aligned}\tilde{T}_{ab}(\tau, \mathbf{k}) &= -a\sigma\eta_{ab} \sum_n \left[\mathcal{D}^n(\tau, k_z) \int d^2x e^{ik_z\epsilon} e^{i(k_x x + k_y y)} + (2\pi)^2 \overline{\mathcal{D}}^n(\tau, k_z) \delta(k_x) \delta(k_y) \right], \\ \tilde{T}_{iz}(\tau, \mathbf{k}) &= -a\sigma \sum_n \mathcal{D}^n(\tau, k_z) \int d^2x \epsilon_i e^{ik_z\epsilon} e^{i(k_x x + k_y y)},\end{aligned}\quad (5.16)$$

where $\mathcal{D}^n = e^{ik_z L_\# / 2} \cdot \overline{\mathcal{D}}^n$ and $\overline{\mathcal{D}}^n = \exp\{ik_z n L_\# - k_z^2 l^2 / 2\}$ from Section 4.4.2. This essentially gives a periodicity in k_z in the SE tensor that goes as $n \cdot k_\#$. We define

$$D(\tau, w) \equiv \sum_n \delta(w - n) \mathcal{D}^n(\tau, w k_\#) = [w \in \mathbb{Z}] (-1)^w \exp\{-w^2 [k_\# \delta(\tau)]^2 / 4\} \in \mathbb{R}, \quad (5.17)$$

which gives

$$\tilde{T}_{ab} = -a\sigma\eta_{ab} D \cdot \mathcal{F}_{k_x, k_y} \{e^{ik_z\epsilon}\}, \quad \tilde{T}_{iz} = -a\sigma D \cdot \mathcal{F}_{k_x, k_y} \{\epsilon_i e^{ik_z\epsilon}\}, \quad (5.18)$$

as expressions for the walls' displacement field's contribution to the total energy and momentum. We used the shorthand notation \mathcal{F}_{k_i} for Fourier transforms (Eq. (11)).

We now get the same result as in Section 4.4.2 in letting $\epsilon = \epsilon(\tau) \sin py$ and considering $k_y \neq 0$. Substituting $\mathcal{D}_w \rightarrow D$ in Eq. (4.50), we get the TT-projected SE tensor for the whole system, and put into Eq. (4.42) gives the gravitational waves sourced by the displacement in the wall normal coordinate. We elaborate on this for $\alpha = 2$ in the coming subsection.

5.3.3 Ripples in matter-dominated spacetime

Consider matter-domination, $\alpha = 2$, and set $\epsilon = \epsilon(\tau) \sin py$. The resulting transverse, traceless tensor perturbations are given by $\tilde{h}_{ij} = \tilde{h}_+ e_{ij}^+ + \tilde{h}_\times e_{ij}^\times$. From Section 4.4.2 we have $\tilde{h}_\times = 0$, so the gravitational waves are monochromatic plus-polarised waves given by

$$a(\tau) \tilde{h}_+(\tau, \mathbf{k}) = H_+^1(\tau, \mathbf{k}) + H_+^2(\tau, \mathbf{k}), \quad (5.19a)$$

where

$$\begin{aligned}H_+^1(\tau, \mathbf{k}) &= +S_1(k\tau) \int_{\tau_*}^\tau d\hat{\tau} C_1(k\hat{\tau}) f_+(\hat{\tau}, \mathbf{k}), \\ H_+^2(\tau, \mathbf{k}) &= -C_1(k\tau) \int_{\tau_*}^\tau d\hat{\tau} S_1(k\hat{\tau}) f_+(\hat{\tau}, \mathbf{k}),\end{aligned}\quad (5.19b)$$

and

$$f_+(\tau, \mathbf{k}) = \frac{16\pi G_N a^3(\tau) \tilde{\pi}_+(\tau, \mathbf{k})}{k^2}. \quad (5.19c)$$

Now consider the TT-projected SE tensor associated with an infinitely thin wall located at the origin. We use Eq. (4.50) to write

$$a(\tau) \tilde{\pi}_+^{w0}(\tau, \ell, \vartheta) \triangleq 2\pi^2 \sigma_w(\tau) \cos^2 \vartheta \cdot (-1)^\ell J_\ell[\ell \tan \vartheta \cdot p \epsilon(\tau)], \quad (5.20a)$$

where $\ell = k_y/p \in \mathbb{Z}$ and $\vartheta = \arctan k_z/k_y \in [0, 2\pi]$. We make further use of this parametrisation and write the periodic system's total TT-projected SE tensor as

$$\tilde{\pi}_+(\tau, \mathbf{k}) = \delta(k_x) \delta(k_y - \ell p) [\ell \in \mathbb{Z}] \times \tilde{\pi}_+(\tau, \ell, \vartheta = \arctan k_z/k_y), \quad (5.20b)$$

where

$$\tilde{\pi}_+(\tau, \ell) = D(\tau, \ell \tan \vartheta p / k_\#) \times \tilde{\pi}_+^{w0}(\tau, \ell), \quad (5.20c)$$

with $\ell \equiv (\ell, \vartheta)$. Now, Eqs. (5.19) to (5.20) gives \tilde{h}_+ for a given input function $\epsilon(\tau)$.

5.3.4 Code output and interpretation

We use the outputted two-dimensional snapshots of χ at lattice coordinate $i = 4$ (chosen randomly) to track the simulated wall position, considered as the coordinates (y, z) of the minimum value of $|\chi|$ (ignoring the anti-wall). We define ε^ϕ as the aforementioned quantity at a y -coordinate for which $\sin py = 1$, subtracting the initial position $z_0 = L_\# / 2$. The confidence region of this is then $\pm \Delta_\# / 2$ in the z -direction.

The code outputs two-dimensional snapshots of tensor perturbations \tilde{h}_{ij} at the same rate, sliced at $u = 0$. We use only $\tilde{h}_{xx} = \tilde{h}_+$, but sporadically check that $2\tilde{h}_+^2 = \tilde{h}^{ij}\tilde{h}_{ij}$.

The formula for the gravitational waves in the thin-wall limit, Eq. (5.19), allows for any function $\varepsilon(\tau)$ as input. Therefore, we will use both the solution to the equation of motion Eq. (4.32), call it ε^{NG} , and the simulated result ε^ϕ . We will have to keep in mind that the latter suboptimally resolved.

The semi-analytical solution \tilde{h}_+ is obtained by means of the simple trapezoidal scheme in Python, specifically the *Scipy* library's `cumtrapz` method. We let \tilde{h}_+^{NG} and \tilde{h}_+^ϕ signify the solution to Eqs. (5.19) to (5.20) with ε^{NG} and ε^ϕ as input, respectively.

5.4 Simulation setups

Below, we describe the reasoning behind the choice of parameters. As a starting point, we consider the fiducial set of symmetron parameters $a_* = 0.33$, $\xi_* = 3.33 \times 10^{-4}$ and $\beta_* = 1$, following Christiansen [13], that will be defined below (Eq. (5.22)). This gives Compton wavelength $L_C \approx 1 \text{ Mpc/h}$ and asymptotic wall thickness $\delta_\infty = \sqrt{2}L_C \sim \sqrt{2} \text{ Mpc/h}$. Simulations are initiated and broken at redshifts z_i and z_f , respectively.

Simulation box

We use a comoving simulation box size that is comparable to the size of the universe—order $\mathcal{O}(\text{Gpc/h})$ —so that $\delta_w \ll L_\#$ and the separation between the walls is $\sim \mathfrak{D} \equiv L_\#/2$. If we want to resolve the Compton wavelength, this requires $N_\# \geq L_\#/L_C \gtrsim \mathcal{O}(10^3)$. However, since we are modelling the entire formation, conventional walls (Eq. (5.3)) will initially be infinitely thick and therefore interact with each other.

Only non-relativistic matter contributes to the expansion, giving the energy density $\sum_s \Omega_{s0} = \Omega_{m0} = 1$. The conformal time is

$$\tau = 2(\Omega_{m0}H_0^2)^{-1/2} \sqrt{a/a_0} = 2\sqrt{a}/H_0, \quad (5.21)$$

giving $\tau_* \simeq 3444 \text{ Mpc/h}$, and the scale factor reads $a = a_* s^\alpha = a_*(\tau/\tau_*)^2$.

We will provide the time step sizes in terms of a Courant factor $C_f = \Delta_\tau / \Delta_\#$ for the external loop and a number $N_\phi = \Delta_\tau / \Delta_\tau^{(\phi)}$ that sets the number of times the asymmetron field solver is used per cycle.

Initial configuration

The normal quasi-static tanh-profile (Eq. (5.3)) approximates the initial configuration to $\check{\chi}_* \rightarrow 0$ and $\check{\chi}'_* \rightarrow \infty$, which does not actually work out. Since $z_* = 1/a_* - 1 = 2 + 1/33 > 2$, choosing initial redshift $z_i = 2.00$ leaves wiggle room enough to get simulations started with spatially separated walls. In other words, with $a_* = 0.33$ and $z_i = 2.00 < z_*$, there is a tiny slot between SSB and initialisation ($z_* - z_i \approx 0.03$) that we do not simulate.

On the other hand, with the analysis in Section 5.1.2 we can impose suitable initial conditions so that the field rolls into the minima in the most effective way. We need to keep in mind that this affects the surface tension and wall thickness.

Symmetron parameters

The code uses phenomenological parameters (a_*, ξ_*, β_*) to define the symmetron model. The mapping to Lagrangian parameters (μ, M, λ) in Eq. (C.4) is [15]:

$$a_* = \left(\frac{\rho_{\text{cr}0} \Omega_{m0}}{\mu^2 M^2} \right)^{1/3}, \quad (5.22a)$$

$$\xi_* = \frac{H_0}{\sqrt{2}\mu}, \quad (5.22b)$$

$$\beta_* = \frac{M_{\text{Pl}}}{M^2} \frac{\mu}{\sqrt{\lambda}}. \quad (5.22c)$$

As before, a_* is the cosmic scale factor at symmetry break, $\xi_* = H_0 L_C$ is the Compton wavelength per Hubble length, and β_* measures the strength of the fifth force (see Eq. (3.13)).

For $\kappa > 0$, the parameter β_* is modified such that $\beta_* \rightarrow \bar{\beta} = (\beta_+ + \beta_-)/2$, and you get an additional parameter $\Delta\beta = \beta_+ - \beta_-$. Formal definitions are found in Christiansen et al. [15].

Nature of wall perturbation

For the linear theory to hold, we need

$$\varepsilon_* \ll L \quad \wedge \quad pL \gg 1 \quad (5.23)$$

where L is a length scale, previously taken to be $L \sim \tau_* \approx 3.4$ Gpc/h. For the prototype, we add that $|\varepsilon(\tau)| \gg \delta_w(\tau)$ for $\tau \in [\tau_i, \tau_f]$ for obvious reasons. We choose to only perturb one wall so that the time of collision between massless particles propagating from different wall centres is at $\tau_i + \mathfrak{D}$.⁶ We would like $\varepsilon_* \ll \mathfrak{D}$, but with a quick look at Fig. 4.1 we can assume that this would require a very high spatial resolution. As a result, we choose to exaggerate the initial perturbation amplitude and risk higher-order effects.

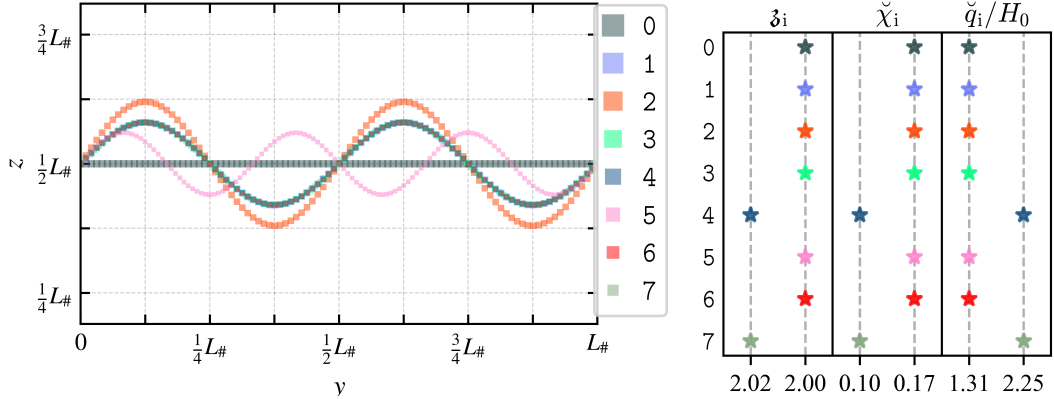
In every simulation, we adjust for the time gap between SSB and initialisation by using $\varepsilon^{\text{NG}}(\tau_i)$ and $\dot{\varepsilon}^{\text{NG}}(\tau_i)$ from Eq. (4.40).

5.4.1 Toy-model catalogue

We present results in Chapter 6 from the eight simulations that are listed in Table 5.1, with supplementary visualisation in Fig. 5.2. We largely use Christiansen et al. [16] to help make parameter choices. Every simulation—labelled $0, 1, \dots, 7$ —uses a 4th order Runge-Kutta solver. We use simulation 1 as a starting point and change one or two parameters at a time for subsequent experiments. The middle wall is unperturbed in simulation 0, and this particular experiment works as a sort of benchmark to separate the wall displacement effect. Each simulation is associated with a characteristic colour (see Table 5.1) that will distinguish it in figures to come.

An additional, completely homogeneous simulation (no walls present) is run with the same background as simulation 1, except that the symmetron initial conditions are optimised as described Appendix B with $\beta_i = 2.03$ and $\beta_f = 1.6$.

⁶Perturbing both walls would give collision time $\tau_i + L_\# / 4$.



(a) Schematic of the initial wall position in the yz -plane for each simulation. Note that 1, 3, 4 and 7 are overlapping.
(b) Initial redshift, and asymptotic scalar and velocity field values.

Figure 5.2: Visual representation of initial configurations listed in Table 5.1.

Wall–anti-wall simulations

	0	1	2	3	4	5	6	7
<i>Simulation box & numerics</i>								
$L_{\#}$ [Mpc/h]	1024	1024	1024	1024	1400	1024	1024	1024
$N_{\#}$	768	768	768	900	768	900	768	768
C_f	0.2	0.2	0.2	0.2	0.2	0.2	0.2	0.2
N_{ϕ}	4	4	4	4	4	4	4	4
<i>Initial configuration</i>								
\mathfrak{z}_i	2.00	2.00	2.00	2.00	2.02	2.00	2.00	2.02
\mathfrak{z}_f	1.00	1.00	1.00	1.00	1.00	1.00	1.00	1.00
$\check{\chi}_i$	0.10	0.10	0.10	0.10	0.17	0.10	0.10	0.17
\check{q}_i	1.31	1.31	1.31	1.31	2.25	1.31	1.31	2.25
<i>Symmetron parameters</i>								
a_*	0.33	0.33	0.33	0.33	0.33	0.33	0.33	0.33
$\xi_* \times 10^4$	3.33	3.33	3.33	3.33	3.33	3.33	1.00	3.33
β_*	1	1	1	1	1	1	1	1
<i>Perturbation parameters ($\varepsilon_* \sin(py)$)</i>								
$\varepsilon_*/L_{\#}$	0.00	0.08	0.12	0.08	0.08	0.06	0.08	0.08
$p/k_{\#}$	–	2	2	2	2	3	2	2
<i>Derived quantities</i>								
$\Delta_{\#}$ [Mpc/h]	1.33	1.33	1.33	1.14	1.82	1.14	1.33	1.33
\mathfrak{D} [Mpc/h]	512	512	512	512	700	512	512	512
L_C [Mpc/h]	1.00	1.00	1.00	1.00	1.00	1.00	0.30	1.00
$\delta_w(\tau_i)/\Delta_{\#}$	18.4	18.4	18.4	21.6	23.2	23.0	5.52	31.2
$\delta_w(\tau_i)/\varepsilon_*$	–	0.30	0.20	0.30	0.38	0.40	0.09	0.52
ω	–	42.3	42.3	42.3	30.92	63.4	42.3	42.3
Υ_*^{\sim}	0	16	24	16	16	18	16	16

Table 5.1: Details about simulations addressed in Part III. Each simulation is labelled 0–7. See Sections 5.3 and 5.4 for description of parameters.

Part III

Findings

Chapter 6

Pilot Testing

This chapter provides simulative insights to our theoretical framework. We both present and discuss results from the simulations described in Table 5.1, and compare these to the theory. The analysis is split into three parts: In Section 6.1 we study the background evolution through box-averaged scalar quantities. Less primitive analysis proceeds in Section 6.2 where the domain-wall dynamics of the two theories are compared. Finally, in Section 6.3 we look at what sort of gravitational waves we expect from this phenomenon.

We include in Section 6.4 some afterthoughts and comments about the simulations. Simulation 6 is considered unsuccessful as it blows up at around $a \approx 0.45$, see Appendix D.1. Where this is considered in the analysis, the results are shown for only $a \in [a_i, 0.46]$.

6.1 Symmetron field

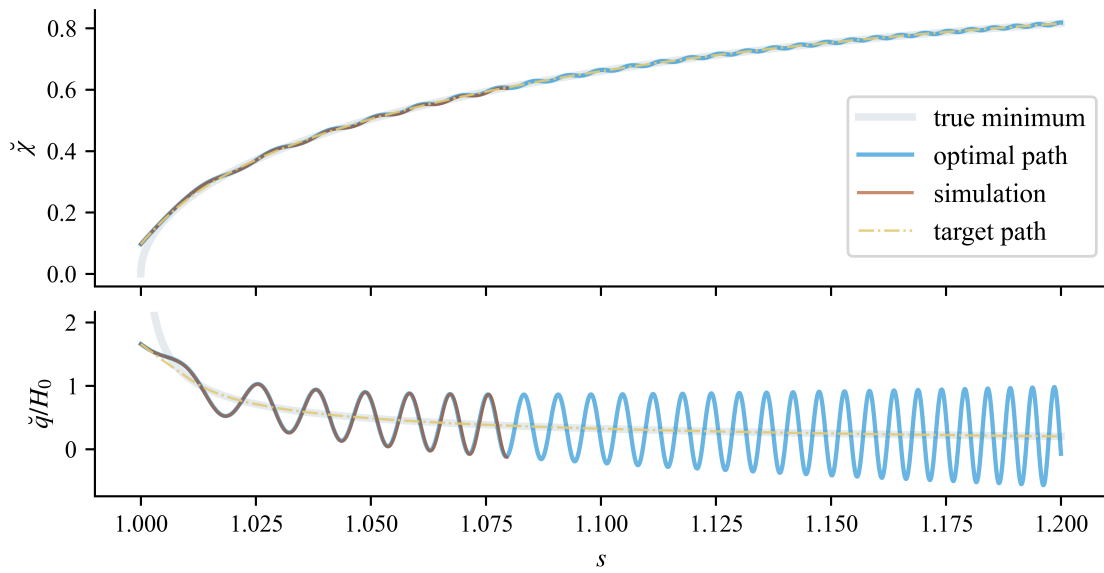


Figure 6.1: The evolution of the symmetron field in the asymptotic limit. The symmetron parameters are the fiducial ones. The simulation results are from the simulation with no walls. We see χ_+ in solid grey, χ_{opt} in solid blue, $\langle \chi \rangle$ in solid red and χ^{ideal} in dashed yellow.

In the simplest case where there are no walls present, and the scalar field takes the same value everywhere, the evolution is described solely by Eq. (5.5). In this case, we expect there to be good correspondence between theory and simulation. We find that the optimal path for the

symmetron to minimise oscillations occurs if initial conditions are given by Eq. (B.7). This result is demonstrated in Fig. 6.1. We distinguish between the idealised path—call it $\check{\chi}^{\text{ideal}}$ —given by Eq. (B.7), and the “optimal” path that solves Eq. (5.5) with initial conditions $\check{\chi}|_{a_i} = \check{\chi}^{\text{ideal}}|_{a_i}$ (and likewise with derivatives), that differ slightly for different choices of a_i (see Appendix B.1 for discussion).

With that established, we move on to wall–anti-wall simulations as described in Section 5.3 and Table 5.1. In general, the symmetron field χ will at SSB roll into one of the two minima, depending on the sign of the field right before it happens. The strength of the oscillations around the true minima depends on both the initial field value and its time-derivative. In our specific simulations, this is deterministic. We show in Fig. 6.2 a handful of background quantities from various simulations. The simulations with earlier initialisation (simulations 4 and 7) give

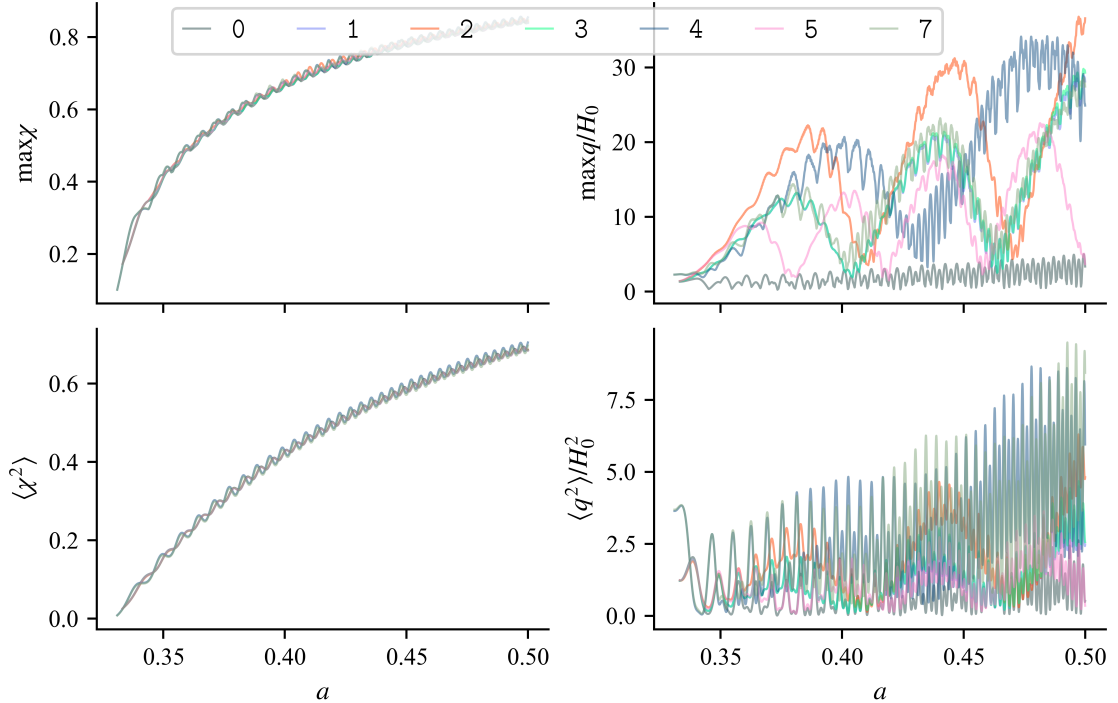
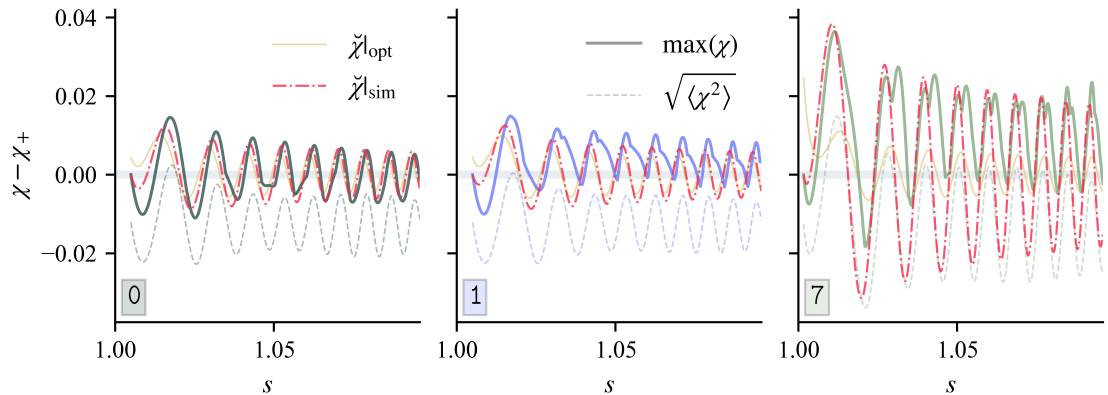


Figure 6.2: Background quantities as functions of scale factor a for different simulations. We show the maximum and box-averaged values of the symmetron field χ and its derivative $q = a^2 \dot{\chi}$.

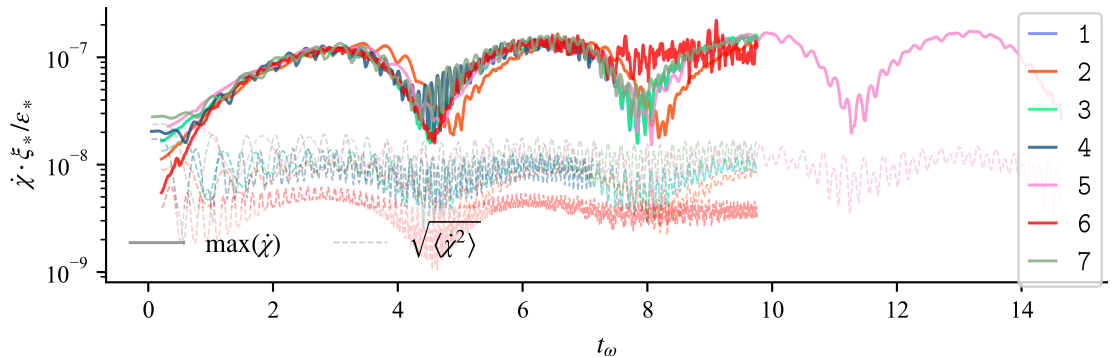
enhanced fifth-force oscillations. This is consistent with numerical solutions to the asymptotic equations with similar initial conditions. We take a closer look at the symmetron field in Fig. 6.3.

Symmetron field. Figure 6.3a shows two things. First, the asymptotic evolution of the symmetron field from simulations, correspond to numerical solutions to Eq. (5.5) with equal initial conditions. We come to this conclusion by combining the maximum value of χ and the smoothness of the averaged χ^2 . Second, the best possible path is very close to the actual evolution in simulations initialised at redshift 2.00, which makes re-runs less useful. On the other hand, we see that simulation 7 is expected to benefit quite a lot from such a tweaking of initial conditions. This also applies for simulation 4. We refer to Appendix B.1 for a demonstration of this.

Velocity field. It turned out to be very convenient to plot certain quantities over the peculiar time parameter $t = \omega(s - 1) = p(\tau - \tau_*)$. One of the quantities that inhabits such a nature is



(a) Yellow solid and red dash-dotted graphs show results from numerically solving the asymptotic Eq. (5.5) with optimal (Eq. (B.7)) and simulation (Table 5.1) initial conditions, respectively. The solid and dashed lines show respective simulation output, in form of maximum and averaged values. All are functions of conformal time $s = \tau/\tau_*$.



(b) The graphs show the outputted maximum (solid) and averaged (dashed) values of q in units $a^2 \epsilon_* \xi_*^{-1}$, all as functions of $t_\omega = p(\tau - \tau_*)$.

Figure 6.3: The asymptotic symmetron field $\tilde{\chi}$ and its time derivative $\dot{\tilde{\chi}}$.

the asymptotic velocity field \tilde{q} , or in actuality the maximum of q . The similarities in Fig. 6.3b in-between simulations are not difficult to spot. We plot the field as q [$a^2 \epsilon_* / \xi_*$] to emphasise how the speed scales as the initial perturbation amplitude (and symmetron length scale). We can look at Fig. 6.2 to see that this is a feature of the perturbation, as simulation 0 lacks said feature. The next section will show how this periodicity is strongly connected to the wall position. The average absolute value tells us more about the fields' stability, where we see a link between these lines' and the asymptotic scalar field's strengths of oscillations around the positive minimum.

6.1.1 Review

In the absence of topological defects, we see near perfect correspondence between predicted and simulated scalar field $\chi = \tilde{\chi}$ (Fig. 6.1). Presence of walls alters the maximum field value (Fig. 6.3a), due to the ‘‘bump’’ in the profile (also to be spotted in Fig. 6.4a). This feature is much more prominent when the walls are perturbed (cf. two left-most panels in Fig. 6.3a). We could have extracted the field value from the snapshots around lattice z -coordinate $k \sim 3N_{\#}/4$, but this is unnecessarily complicated and time-consuming, and the temporal resolution would be suboptimal.

In any case, we see from the *smooth* average-squared field-values in Fig. 6.3a, that the overall oscillations are very close to what we expect. We believe the aforementioned bumps to be a result of the quasi-static approximation (Section 5.1.1), which assumes time derivatives to be close to

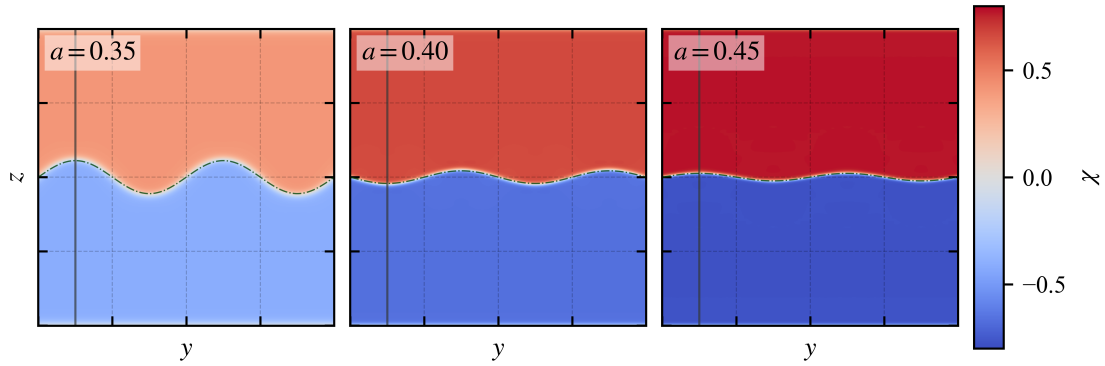
zero.

The path the field can take that inhabits the smallest possible fifth-force oscillations is close to what happens in simulations 0–3 and 5. The same cannot be said for simulations 4 and 7.

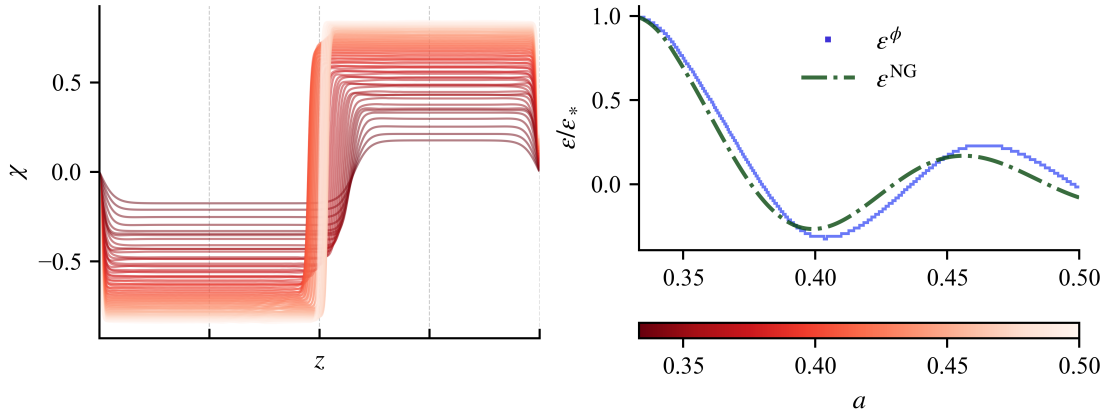
6.2 Domain-wall dynamics

In the following, we ignore the anti-wall at the box's boundaries and focus on the middle wall. Simulation-wise, the wall's position is tracked by the minimum value of $|\chi|$, i.e. the z -coordinate at which the field is closest to zero. We keep in mind that we do not expect a perfect match between the simulated and analytical wall perturbation, partly because the analytical equations are only valid for perturbations of leading order, but also because the thin-wall limit is expected to fail at the early stages of the phase transition. A more tangible way to look at it is to consider the unperturbed unit-normal vector that we put along the z -axis; just by looking at the simulations (Fig. 6.4a), we can see that this is clearly not the case, at least close to phase transition.

We reduce the problem from three dimensions to two, and then again to one dimension by considering a suitable slice in the y -direction (where $\sin py = 1$) at which we take the z -coordinate of the minimal absolute value of the scalar field χ . An example of the two-dimensional perspective is shown in Fig. 6.4a. This picture is more or less the same for all simulations, at least when comparing by-eye.



(a) The domain wall evolution in the yz -plane of the simulation box. We indicate the aforementioned slice with a grey vertical line. The dash-dotted green graph is $\epsilon^{\text{NG}}(\tau(a), y)$.



(b) *Left panel:* The scalar field value along $y = 96\Delta_z$ at different redshifts following the colour bar in the right panel. *Right panel:* The wall coordinate as function of time.

Figure 6.4: Demonstration of the interpretation of the results from simulation 1.

We observe a ‘‘bump’’ in the quasi-static tanh-solution in each simulation, manifesting in plots like the left panel of Fig. 6.4b around $z \sim z_0, \bar{z}_0$, and in the maximum value of χ in Fig. 6.3a. This effect is seemingly more prominent in simulations with $\varepsilon_* > 0$, i.e. all except simulation 0.

The simulated wall position graph is not perfectly overlapping with the analytical one, as the right panel of Fig. 6.4b shows. Simulated walls show a tendency to evolve slower, at least initially, realised in a phase difference between ε^ϕ from simulation and ε^{NG} from the thin-wall approximation.

In Fig. 6.5 we show the difference between the Nambu–Goto prediction—which for $e = \varepsilon/\varepsilon_*$ vs. $t_\omega = \omega(s - 1)$ is the same any setup—and the field theory. Simulations with similar perturbation setup (cf. simulations 1, 2, 4, 7) but different box parameters give similar wall evolution. Larger initial amplitude (simulation 2) increases the difference, as does larger scale parameter (simulation 5). The bottom panel of Fig. 6.5 is remarkably alike Fig. 6.3b.

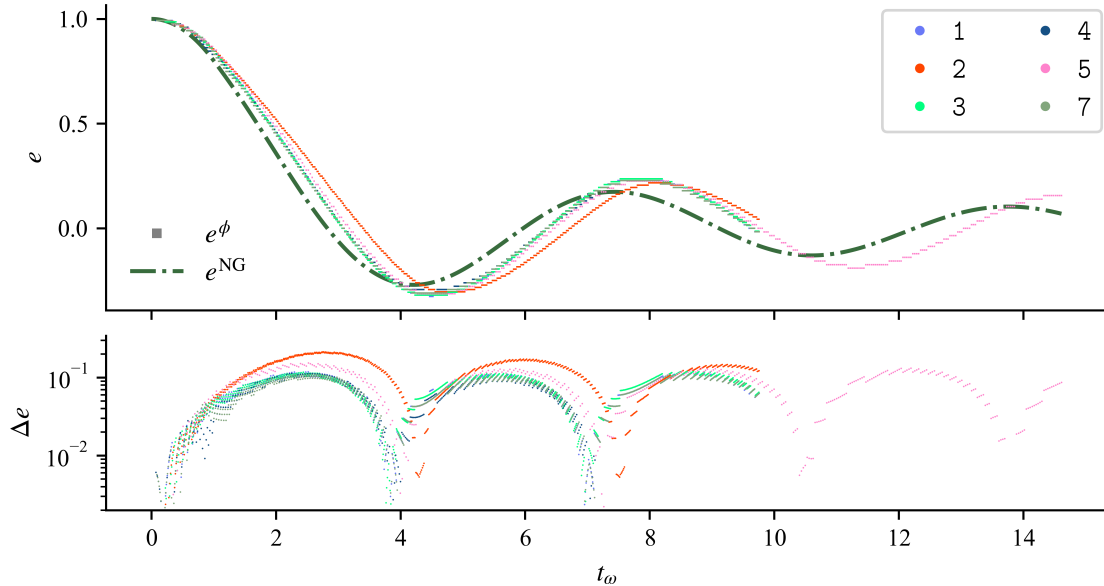


Figure 6.5: Functions of the scaled time parameter $t_\omega = \omega(s - 1) = p(\tau - \tau_*)$. *Top panel:* The wall extremal position normalised to the initial amplitude, $e = \varepsilon/\varepsilon_*$. *Bottom panel:* The absolute difference between the wall position from calculations and simulations, $\Delta e = |\varepsilon^{\text{NG}} - \varepsilon^\phi|/\varepsilon_*$.

We see that initial amplitude actually does matter in simulations, cf. simulation 1 vs. 2. The thin-wall approximation disagrees with this, but it can be argued that this relates to the validity of the linear-perturbation size. This suggests that higher-order effects or resolution issues are more likely explanations for the discrepancy, rather than a problem with the damping term in the equation of motion. Alternatively, this discrepancy could simply be an indication of the inherent approximation in the Nambu–Goto description.

We observe that the initial perturbation amplitudes in simulations 2 and 4 are similar in comoving units, with $\varepsilon_* = 0.12L_\# \approx 123 \text{ Mpc/h}$ and $\varepsilon_* = 0.08L_\# = 112 \text{ Mpc/h}$, respectively. The large-box simulation gives results close to those with $\varepsilon_* = 0.08L_\#$, whereas simulation 2 shows different wall dynamics. The point is that as far as the linearised-perturbation analysis goes, the order is given relative to the comoving horizon $\tau = \tau_*$. This gives substance to the hypothesis that the discrepancy might be due to interactions with the anti-wall. On the other hand, when factoring in the perturbation scale parameter, we can think of the perturbation in simulation 4 as equal to those of 1, 3, etc. A better upper length scale may then be $\sim \mathfrak{D}$ as opposed to τ_* .

6.2.1 Review

The full field-theoretical description of the wall evolution agrees with the thin-wall approximation to some level. We find that the maximum error is $\max(\Delta\epsilon) \approx (0.16 \pm 0.05)\epsilon_*$ between simulations 1–5 and 7. Similarly, we find average values $\langle\Delta\epsilon\rangle \approx (0.08 \pm 0.03)\epsilon_*$. The general tendency is that the oscillatory behaviour in the Nambu–Goto description is quicker and somewhat weaker than what simulations would have it. Both show characteristics of a damped harmonic oscillator with period $\gtrsim 2\pi/t_\omega$. Upgrading the spatial and temporal resolution with about 15%—as done with simulation 1 and 3—does not show significant changes in the evolution of the wall displacement parameter.

Minimising scalar-field oscillations does not seem to affect the wall evolution particularly. This can be seen by comparing simulations 1, 3, 4 and 7 in Fig. 6.5 which all have the same relative initial amplitude, but different levels of fifth-force oscillations (Fig. 6.3a). However, changing the “curvature” of the wall, seems to change the overall behaviour of the displacement parameter ϵ . Here, we increase the parameter Υ_*^\sim from 16 to 18 (simulation 3) or 24 (simulation 5). We use this as a naive quantification of the “badness” of the equation of motion for ϵ ; larger amplitude and wavenumber correspond roughly to increased risk of higher-order effects. The unperturbed wall normal coordinate is aligned with the z -axis, and Υ_*^\sim is a rough measure of the perturbed wall’s normal coordinate, relative to this.

The wall–anti-wall system may inhabit inter-kink forces if the walls are not sufficiently far apart [54], and this could contribute as an external force in the equation of motion for the wall perturbation. Since such forces would be attractive and position-dependent [54], this could explain why ϵ^ϕ is “slower” and “deeper” than ϵ^{NG} . There might also be “intra-kink” forces at play, that is interactions between different points on the same wall. The parameter Υ_*^\sim can provide an indication as to the risk of this happening, at least in the y -direction. The walls are not infinitely thin and one can imagine that internal forces may contribute in the z -direction.

We have *not* thoroughly tested whether $\epsilon^\phi(\tau, x, y) = \epsilon^\phi(\tau) \sin py$ holds over time in simulations. From Fig. 6.4a, and similar results, we can see that the sine profile seems to be quite well-preserved throughout the evolution.

6.3 Gravitational waves

The gravitational waves from the Nambu–Goto motion are given by a complicated expression. We have not been able to obtain the corresponding expression in configuration space, neither have we found a way to present sensible summary statistics from it.

We list a few key points about the simulated gravitational-wave results in general. The data we get from the code is the averaged squared value of the strain’s conformal time derivative (see below, Eq. (6.1)) at every time step, and the Fourier image of the tensor perturbations for $\tilde{\mathbf{n}} = (0, \mathbf{v}, \mathbf{w})$ at every fourth-or-so time step.

- Zero walls or unperturbed walls (simulation 0) produce no gravitational radiation.
- The predicted periodicity in k_y (that $\tilde{h}_{xx}|_{k_y \neq np} \rightarrow 0$) agrees with simulations.
- There is decidedly a signature of the perturbation in some wave modes. The characteristics are similar to what the thin-wall limit predicts, but the resemblance varies a lot from mode to mode, and also in time.
- Computing the magnitude of the gravitational waves analytically does not agree with corresponding simulative results.

- The unpredicted *imaginary* parts of the simulated gravitational waves carry much more resemblance to analytically calculated, real ones, than their real counterparts.

6.3.1 Gravitational radiation

We begin by having a look at the energy density of the gravitational waves, which is obtained through the spatial average conformal time derivative of the *real-space* tensor perturbations [36],

$$\rho_{\text{gw}} = \frac{1}{32\pi G_N a^2(\tau)} \langle \dot{h}_{ij}(\tau, \mathbf{x}) \dot{h}_{ij}(\tau, \mathbf{x}) \rangle_{\text{box}} = \frac{1}{32\pi G_N a^2(\tau)} \frac{1}{N_\#^3} \sum_{ijk} \sum_i [\dot{h}_{ij}(\tau, \mathbf{x}_{i,j,k} \Delta\#)]^2. \quad (6.1)$$

We plot this as functions of (scaled) conformal time s and the perturbation time parameter

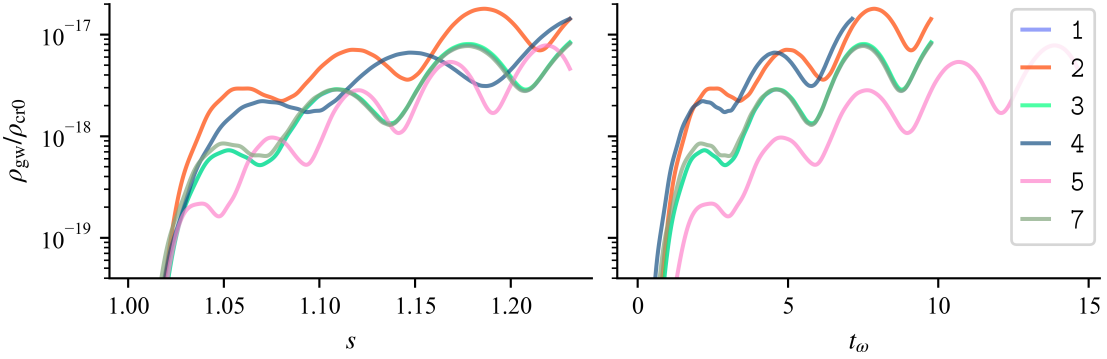


Figure 6.6: The box-averaged gravitational-wave radiation, normalised to the critical density today. Note the logarithmic y -axes. *Left panel:* ρ_{gw} as function of $s = \tau/\tau_*$. *Right panel:* ρ_{gw} as function of $t_\omega = \omega(s - 1) = p(\tau - \tau_*)$.

$t_\omega = \omega(s - 1)$ in Fig. 6.6 for a number of simulations. The graphs in the right panel show similar patterns as before, in Fig. 6.3b. The energy is in the range $\log(\rho_{\text{gw}}/\rho_{\text{cr}0}) \sim -18, -17$. In comparison, gravitational radiation from domain wall networks is often approximated as $\rho_{\text{gw}} \sim \sigma^2/(40\pi M_{\text{Pl}}^2)$ [51], which is approximately $\sim 10^{-12}\rho_{\text{cr}0}$ for the symmetron parameters used in every simulation, except for simulation 6.

6.3.2 Comparison with analytical results

We refer to Section 5.3.4 for details about how the data were extracted. Henceforth, \tilde{h}_+ refers to Eq. (5.19), for which inputs ε^{NG} and ε^ϕ give \tilde{h}_+^{NG} and \tilde{h}_+^ϕ , respectively. The output from simulations, the xx -component of the tensor perturbations, is denoted $\tilde{h}_+ = \tilde{h}_+^{\Re} + i\tilde{h}_+^{\Im}$. We will present our results in terms of scaled wavenumbers that satisfy

$$k_x = 0, \quad k_y = \mathbf{v}k_\# = \ell p, \quad k_z = \mathbf{w}k_\# = \ell p \tan \vartheta; \quad \ell \in \mathbb{Z}, \quad (6.2)$$

where $\tilde{\mathbf{n}} = (\mathbf{u}, \mathbf{v}, \mathbf{w}) \in \mathbb{Z}^3$ represents the lattice momentum. Note that $\ell = (\ell, \theta)$ and (\mathbf{v}, \mathbf{w}) represent different comoving momenta $(0, k_y, k_z)$ in e.g. simulation 1 and 4. The length of the wave vector is $k = |p \ell \sec \vartheta|$.

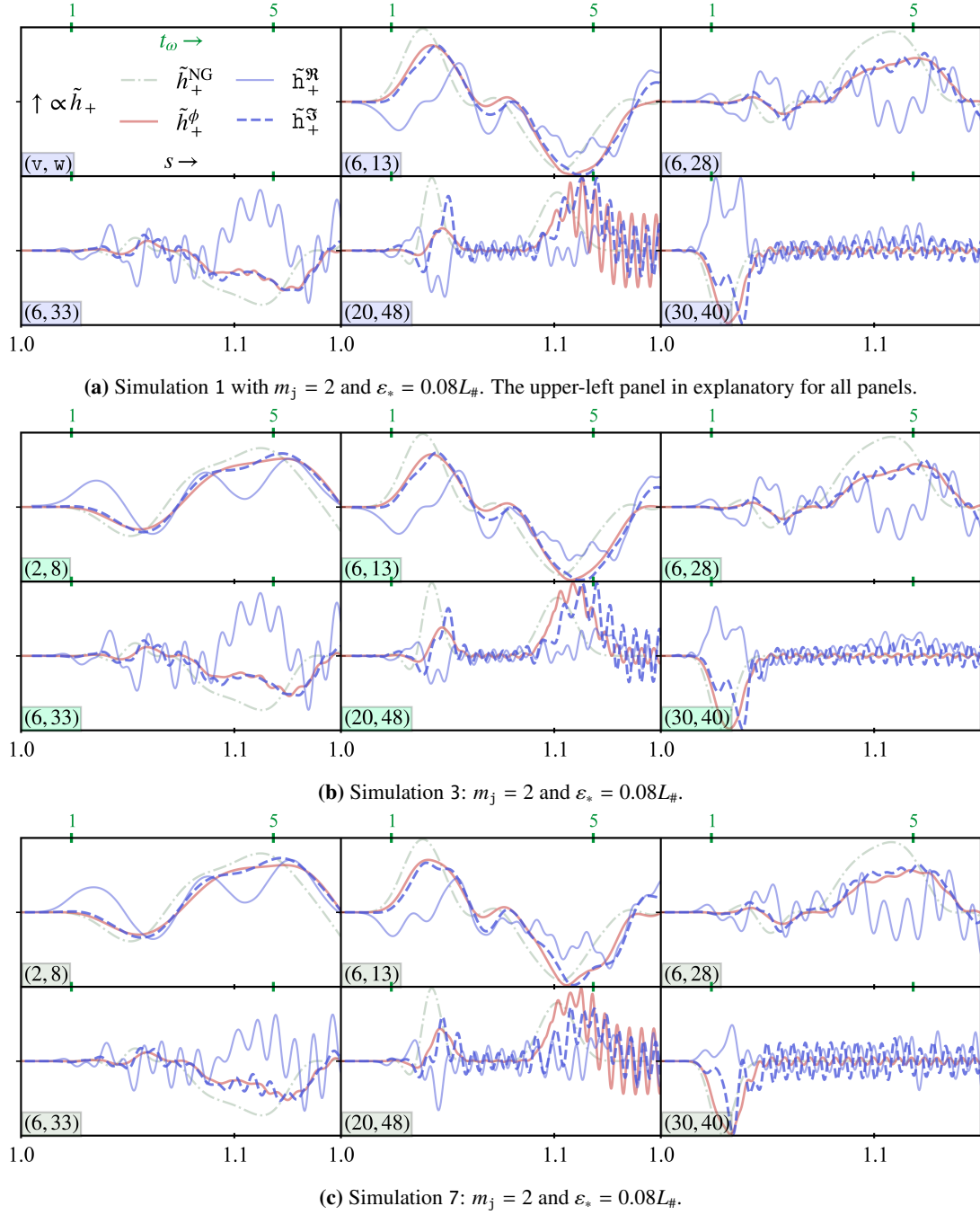
The first notable observation is that $\tilde{h}_+ \in \mathbb{R}$, whereas $\tilde{h}_+ \in \mathbb{C}$. In fact, the results consistently show more resemblance between \tilde{h}_+^ϕ and \tilde{h}_+^{\Im} , than between \tilde{h}_+^ϕ and \tilde{h}_+^{\Re} . It is clear that the slight offset $\Delta\varepsilon = |\varepsilon^{\text{NG}} - \varepsilon^\phi|$ makes for a significant difference in \tilde{h}_+ .

Figure 6.7 demonstrates this for a number of k -modes in simulations 1, 3, 7, 2 and 5. The magnitudes are ignored in this analysis. There is a quite remarkable likeness between \tilde{h}_+^ϕ (solid red lines) and \tilde{h}_+^{\Im} (blue dashed lines). Comparison of Figs. 6.7a to 6.7c suggests that more

prominent scalar-field fluctuations disturb the gravitational wave modes a little (blue graphs), and that \tilde{h}_+^ϕ is sensitive to tiny deviations in ε^ϕ (red graphs). The initial size of the perturbation, ε_* , affects the temporal behaviour, as expected, and not just the scale parameter p . This is seen by comparing Figs. 6.7d and 6.7e to any of Figs. 6.7a to 6.7c. We see from the secondary time-axes that the resonance in t_ω -space lives on to some extent, backed by the right panel of Fig. 6.6.

Studying each wave mode's evolution over time does not give as much physical insight as it is time-consuming.¹ Another way to compare the results is to study the strain in some instances in time. We see from Fig. 6.6 where the intensity of the waves peaks and use this to choose time points for our coming analysis. It is interesting to compare simulations with different

¹There are potentially $N_\#^2/2/m_j$ different modes for each simulation.



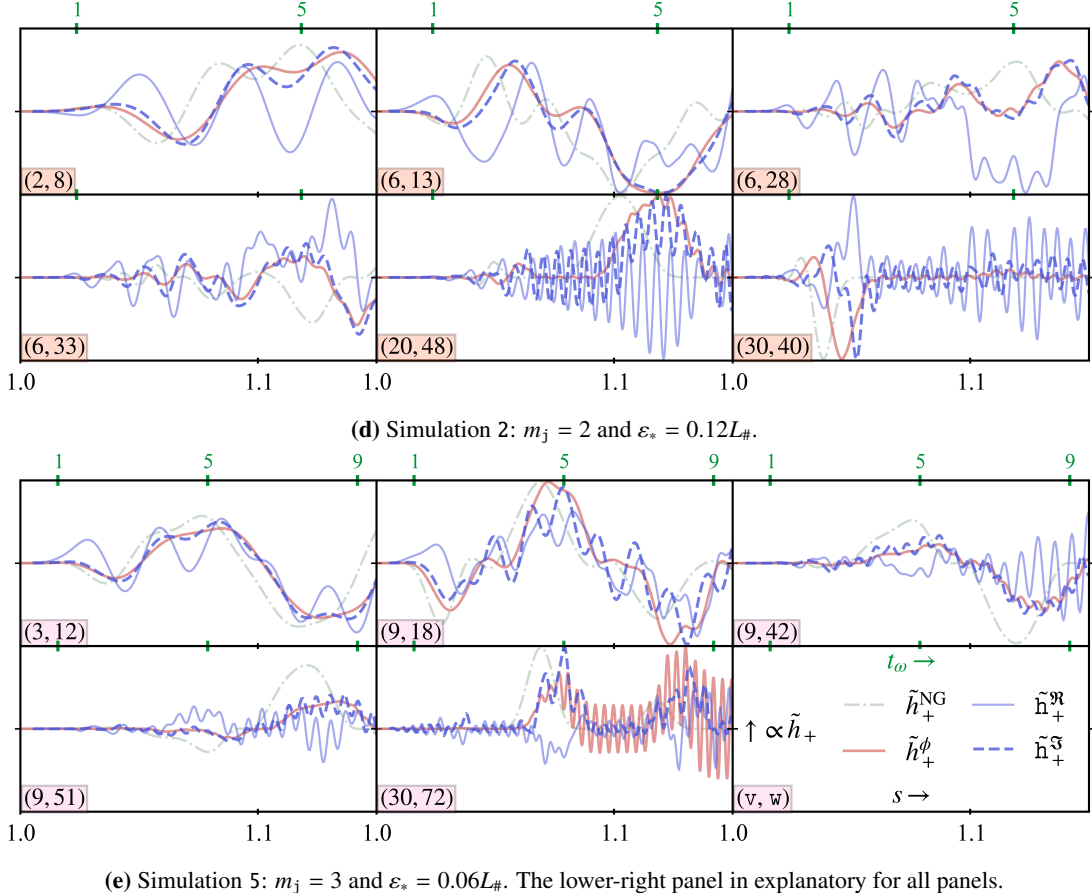


Figure 6.7: Monochromatic plus-waves evolving over conformal time $s = \tau/\tau_*$, normalised to unity ($h_+ / \max |h_+|$). The upper-left/lower-right panel is explanatory for all panels: Green dash-dotted graphs represent \tilde{h}_+^{NG} , orange solid ones represent \tilde{h}_+^ϕ and in blue are \tilde{h}_+ . The wave vector is given in the lower left corner of each plot, as (v, w) . The secondary above x -axis represents scaled time $t_\omega = p(\tau - \tau_*)$.

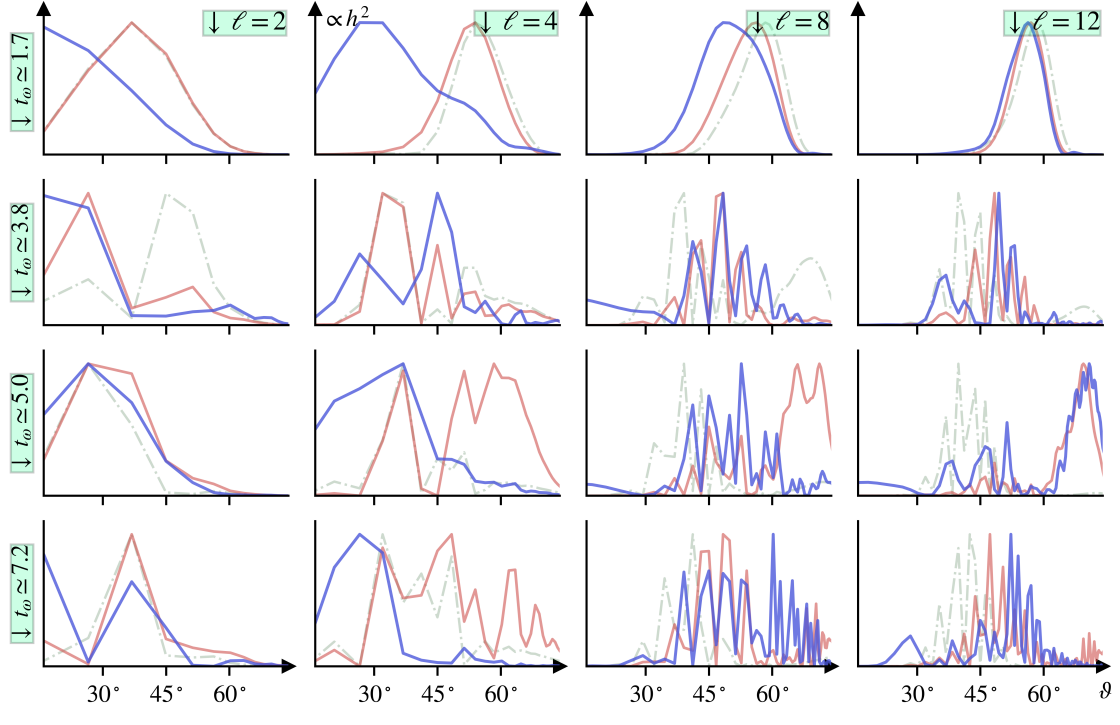
perturbation scale. In Fig. 6.8 we compare the results from the Nambu–Goto theory (Eq. (5.19)) \tilde{h}_+^{NG} and \tilde{h}_+^ϕ , and directly from simulation, \tilde{h}_+ . We stress that the magnitudes are not reported, and all spectra are normalised as $\tilde{h}^2 / \max \tilde{h}^2$. Each column represents the same ℓ -mode for different times, whereas each row signifies the same time point but different ℓ 's. The horizontal axes show ϑ , where $\vartheta = 0^\circ$ and $\vartheta \rightarrow 90^\circ$ correspond to $\mathbf{k} = (0, k, 0)$ and $\mathbf{k} \rightarrow (0, 0, k)$, respectively. Note that $\vartheta = 0^\circ$ suggests waves propagating along the domain wall.

The results in Fig. 6.8 show some likeness in the shape and evolution of \tilde{h}^2 with \tilde{h}_+^ϕ and \tilde{h}_+ for some values of ℓ . The wave vectors in Fig. 6.8a and Fig. 6.8b are equal, but the time points are different.

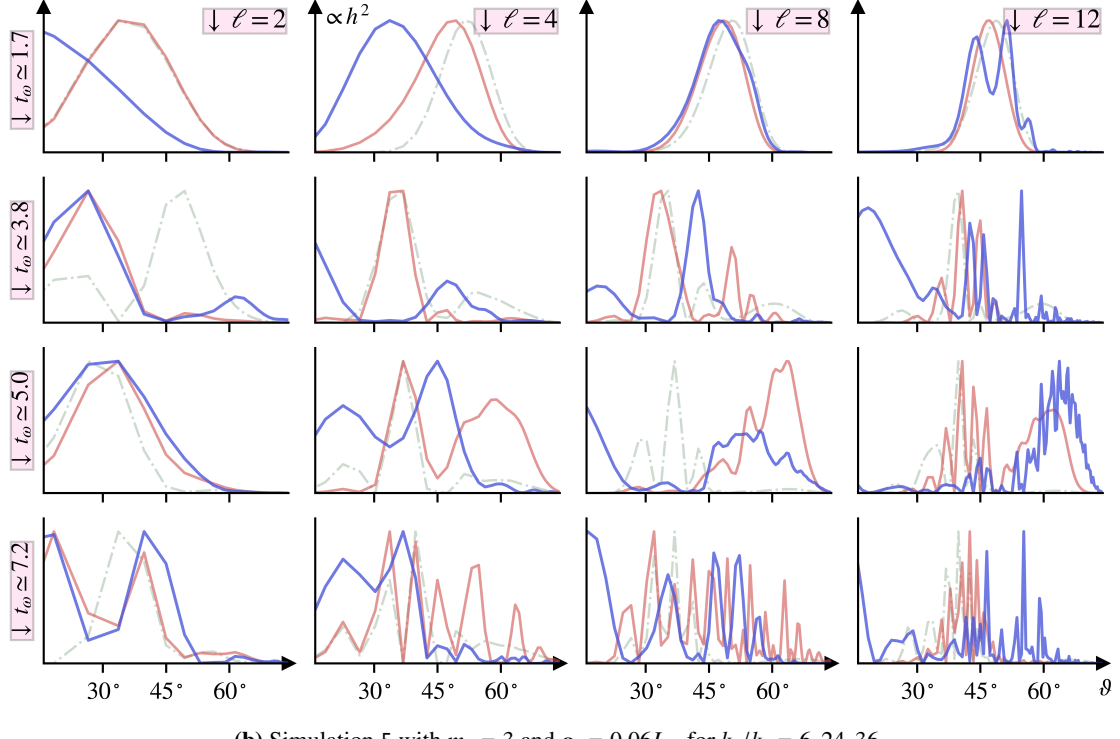
6.3.3 Review

Figure 6.7 shows that the perturbation parameters clearly manifest in the gravitational waves. The physical insight of analysing this mode by mode is maybe not too great, but the likeness indicates that there is a pattern to be found, at least. We would have to go further into technicalities regarding the lattice spin-2 projector to conclude anything about what causes $\tilde{h}_+^3 \neq 0$ (see Appendix D.2). Figure 6.6 agrees that there is a predictable relationship between the wall perturbation in its simplest form ($\varepsilon \sin py$) and gravitational radiation.

There is a large and inconsistent difference in magnitude between \tilde{h}_+^2 and \tilde{h}_+^3 . This thesis



(a) Simulation 3 with $m_j = 2$ and $\varepsilon_* = 0.08L_\#$, for $k_y/k_\# = 6, 24, 36$.



(b) Simulation 5 with $m_j = 3$ and $\varepsilon_* = 0.06L_\#$, for $k_y/k_\# = 6, 24, 36$.

Figure 6.8: The strain squared $\tilde{h}^2 = 2\tilde{h}_+^2$ as functions of angle ϑ , normalised to unity; $\tilde{h}^2 / \max \tilde{h}^2$. Green dash-dotted graphs represent \tilde{h}_+^{NG} , orange solid ones represent \tilde{h}_+^ϕ and in blue are \tilde{h}_+ .

does not cover this part of the analysis in depth, but we list some issues that are possibly related to this.

- The dimensions of the Fourier-transformed tensor perturbations and SE tensor are

$[k^{-3}] = (\text{length})^3$ and $[k \cdot k^{-3}] = (\text{length})^2$, respectively, in the continuous case. There can be a misunderstanding in the unit conversion both from the simulation output and in the computation of $\tilde{\pi}_+$. A source of confusion may be the transformation from discrete to continuous Fourier transforms.

- The cumulative-trapezoidal scheme that computes \tilde{h}_+ has numerical weaknesses, and the input to \tilde{h}_+^ϕ is originally discrete. Tiny changes in ε can have massive effect for \tilde{h}_+ , and discontinuities often lead to larger values.
- The wall width is defined from convention, and measures scale more than an actual physical observable.

6.4 Hindsight

Some technicalities regarding our choices is necessary to address at this point. It seemed natural to begin with a set of parameters that was deemed sensible before, i.e. $a_* = 0.33$, $\xi_* = 3.33 \times 10^{-4}$ and $\beta_* = 1$ from Christiansen et al. [15]. The initial idea was to start simulations at initial redshift $z_i = 2.00$ with SSB happening only a few time steps before this, at $z_* = 1/a_* - 1 = 2 + 1/33 \approx 2.0303$. This way, the “true” wall width $\delta_w = (a\mu\chi_+)^{-1}$ is not infinite at the start, and we may use the quasi-static approximation for χ and q with $\check{\chi} = \chi_+$. We used the analytical expression for ε and $\dot{\varepsilon}$ to find suitable values at initial time. To get an idea of the impact of larger oscillations around minima, we attempted initialising at redshift 2.02, where the walls were dangerously close to colliding, but were separated just enough.

It was not until later that we decided to tweak the initial conditions to our advantage, and performed the analysis in Section 5.1.2. Now we could initialise as close to phase transition as we wanted. The catch was now that maybe the surface tension was too different from what we used in Section 4.3, so we spent some time adjusting the expression for σ_w and studying the effect on ε . The result was that only when the fifth-force oscillations are exaggeratedly large was there significant changes in ε .

Now, the plan was to run additional optimised simulations as explained in Appendix B.2, but the first experiments (including 7) did not show any change in the symmetron field. This was due to a bug in the new lines of C++-code that overwrote the initial conditions to the previous versions (χ_+ and q_+). One of these, simulation 7, is presented amongst the results, as it is unique, while the rest was equivalent to other simulations and therefore discarded. Due to shortage of time, no more simulations were run, with the exception of the homogeneous one presented in Fig. 6.1.

If we were to do it all over again, it might make sense to set for example $a_* = 2/5$ such that $z_i = z_* = 3/2$, to avoid a tiny difference between z_i and z_* . We could then use the initial conditions $\check{\chi} = \chi_*$ and $\check{q} = q_*$ from Appendix B, with $\varepsilon = \varepsilon_*$ and $\dot{\varepsilon} = 0$. The advantage that $\dot{z}_w = 0$ is not only that q is less complicated, but we avoid having to include it in χ as well. To account for a moving wall, we should technically perform a Lorentz transformation on the argument to the hyperbolic tangent [8, 54]. In the kink scenario from Section 3.1.1, Eq. (3.3) becomes [54]

$$\phi_k(t, x) = \eta \tanh \left(\sqrt{\frac{\lambda}{2}} \eta \frac{x - vt}{\sqrt{1 - v^2}} \right), \quad (6.3)$$

where v is the speed of the moving defect.

Chapter 6. Pilot Testing

Chapter 7

In-Depth Analysis

In this chapter, we take a few steps back and look at our work from a more critical point of view. We provide a general discussion of the toy-model analysis—both methodically and result-wise—in Sections 7.1 and 7.2 with regrets and proposed methods of verification. In Section 7.3 we address the framework as is, agnostic to any potential (in)validations, and discuss its implications and potential. We summarise with some open questions in Section 7.4.

7.1 Project reflection

We are able to create model scenarios with AsGRD that lets us test the validity of the thin-wall approximation. The quasi-static approximation with naive boundary conditions ($\check{\chi} = \chi_+$) is used as to configure the initial symmetron state, which can affect the comparison. Besides this inherent approximation, there are three main reasons why we do not expect a perfect match between ε^{NG} and ε^ϕ :

Wall thickness: The wall is thin compared to other dimensions of the problem throughout the entire evolution. In particular, $\max(\delta_w) = \delta_\infty(a_i \check{\chi}_i)^{-1} \approx 25 \text{ Mpc}/h \ll L_\#$ for the majority of the simulations (see Table 5.1). However, the wall thickness is comparable to the perturbation amplitude in the very beginning of the simulations and this might affect the wall motion.

Perturbation amplitude: We choose initial perturbation strengths $\varepsilon_* \in [0.12, 0.24]\mathfrak{D}$, where the wall separation is $\mathfrak{D} = L_\#/2$. If we let \mathfrak{D} be the linear-perturbation length scale, then $(\varepsilon_*/\mathfrak{D})^2 \rightarrow 0$, which is not the case. In other words, we are pushing the limits of the linear perturbation theory. Still, between simulations 1, 3–5 and 7 we have $|\varepsilon| < 0.06\mathfrak{D}$ for $t_\omega > 2.3$, following Fig. 6.5, so second order terms are small after this $((\varepsilon/\mathfrak{D})^2 < 4\%)$.

Spatial resolution: We expect discrepancies due to the discreteness of the lattice. The absolute wall displacement field is below 3% of the box length for the majority of the evolution. For example in simulation 1, this corresponds to only about 23 lattice points. Another thing to have in mind is that to get ε^ϕ , we extract the z -coordinate with the smallest absolute value of χ , which in principle can be a range of coordinates.

The first two arguments are most prominent in the initial evolution.

Simulations give substance to the derived equation of motion for a linear perturbation to the planar-wall normal coordinate, Eq. (4.31), in a matter-dominated, conformally flat spacetime. The difference between the analytical and numerical solution to this is insignificant. The anomaly between the Nambu–Goto and full field-theoretical results is more or less consistent in-between simulations, which speaks against any numerical explanations.

The toy-model simulations give tensor perturbations $\tilde{h}_+ = \tilde{h}_+^R + i\tilde{h}_+^I$ roughly comparable to the Nambu–Goto prediction with the simulated wall position as input, $\tilde{h}_+^\phi \in \mathbb{R}$. The Nambu–Goto “naive” prediction $\tilde{h}_+^{\text{NG}} \in \mathbb{R}$ is generally worse than \tilde{h}_+^ϕ , and the resemblance is most prominent between \tilde{h}_+^ϕ and \tilde{h}_+^I .

With more time, we could have developed the expression for $\dot{\tilde{h}}_+$ more so that we might have obtained an analytical approximation for $\rho_{\text{gw}}(\tau)$ in the thin-wall limit to compare with Fig. 6.6. We elaborate on this in Section 7.2.

Systematic convergence-testing would give more reliability to our results. Such an analysis is not covered in this thesis. Together with similar analyses [15, 16], trial-and-error is how we set the numerical parameters on the simulations.

7.2 Continued assessment

In this section, with the toy model from Section 5.3 in mind, we elaborate on further analysis that time limitations does not allow us to perform.

7.2.1 Inter-wall force

Vachaspati [54] gives a rough estimate of the force between a kink and an antikink. A possible way forward could involve such estimates for our setups, and see if this relates the distance $|z_w(\tau, y) - \bar{z}_w|$ to the resulting $\epsilon^\phi(\tau, y)$ in any way.

7.2.2 Gravitational waves

We turn our attention to the *analytically* computed gravitational-wave modes in Eq. (5.19). The energy density of gravitational waves in an FLRW universe given in Eq. (2.56), presented for *simulated* waves in Fig. 6.6. One way to use this, is to discretise the integration; $dk \rightarrow k_\#$, and loop through all possible modes \tilde{n} (which is an option in AsGRD). Agnostically, this involves solving two integrals numerically $N_\#^3$ times for each τ . This brute-force experiment is computationally very inefficient, and it would be much more insightful to find an approximate expression for ρ_{gw} that is analytical, or at least with fewer computation steps. Such an expression may exist through asymptotic evaluations of Bessel functions, among other things. Not only would this offer an efficient verification strategy, but would also help put this framework into the context of actual gravitational-wave observations.

In any case, the aforementioned seemingly trivial brute-force analysis was tried towards the end. This precursory analysis is not presentable due to unforeseen problems and time-shortage.

In-depth gravitational-wave analysis. An interesting analysis would be to systematically change various parameters in the source $\tilde{\pi}_+$ and see what effect this has on the resulting tensor perturbations. From what we gather, it appears that in letting σ_w and/or δ_w be defined from oscillating asymptotic fields $\pm\check{\chi}$ instead of χ_\pm , \tilde{h}_+ becomes noisier, i.e. with small oscillations around the original result. Changing ε seems to shift the phase of the oscillations. The analysis is precursory, and therefore not included here. This is comprehensive as \tilde{h}_+ depends on time and a two-dimensional wave vector, and several other parameters. This motivates approaches such as attempts at summary statistics that would reduce the dimensionality of the problem drastically.

Dimensional analysis. It might be possible to perform an asymptotic analysis of Eq. (5.19) to estimate the strain in terms of ε_* (and possibly also p). With Fig. 1.1 (and others, of course) one could find a lower limit to ε_* for the produced waves to be detectable. Now, if this limit exceeds the linearity constraint (Eq. (5.23) with $L \sim \tau_*$), one would have to reconsider the motivation for further gravitational-wave analyses from linear perturbations.

7.2.3 Supplementary experiments

It was indeed very unfortunate that the simulations that were supposed to be updated with optimised initial conditions (cf. simulation 7), were run with a bug that was not detected soon enough, as elaborated in Section 6.4. Here are some alterations that can be done in future experiments.

Upgraded resolution. With extended time (and computer) resources, we would have run simulations as described in Section 6.4, preferably with better spatial and temporal resolution. Below we describe possible analyses that could come from such fine-grained toy-model experiments.

- Our attempt to decrease the width of the wall (simulation 6) could have been planned more carefully. Quantities like $\langle q^2 \rangle$ diverge at approximately $\tau = \tau_i + \mathfrak{D}$, as shown in Fig. D.1. This corresponds to the time when massless particles at initially at the middle wall, propagating in the z -direction, would reach the opposite wall. Had we done it again, we would have run the same simulation with better spatial resolution. This could have given insight to the dependence on the wall width in the wall evolution and in turn the gravitational waves.
- Better spatial resolution would allow for smaller initial perturbation amplitude, and thereby help us understand if the discrepancy between the thin-wall approximation and the full theory is due to the perturbation being too large.
- With higher-frequency perturbations, e.g. $p = 4k_\#$, we would only have to simulate over half the time as simulation 1 did, to see similar evolution. Finer grids would resolve such sinus waves.

Varying the physics. There are several other simulation designs that might help isolate important artefacts from the not-so important features. We list a few of these ideas.

- We could look at already-formed walls for which $\check{\chi} \approx 1$ and $\sigma \approx \sigma_\infty$ to see if and how the time-dependence of the surface tension affects the wall displacement field and metric tensor perturbations. Constant surface tension allows cleaner expressions as well as model-independence.
- If we change the “nature” of the wall perturbation from a sine to a cosine, this might help in understanding the unpredicted imaginary component of the gravitational waves discussed in Section 6.3.2. We performed some tentative studies doing exactly this, and saw that the trend was alternating real and imaginary modes, arranged oppositely from the Jacobi–Anger expansion (see Appendix C.4.1). This is what we expect, but more careful studies should have been made.
- Testing different amplitudes ε_* and scales p would give insight to the discussion about the validity of the thin-wall approximation. We saw that ε^{NG} becomes the same function when plotted over t_ω and divided by ε_* , and that this did not hold for ε^ϕ . For example, if we

perform simulation 3 with $\varepsilon_* = 0.06L_\#$, we would have got one of three possible results, if put in context with Fig. 6.5, which could help reduce the number of possible explanations:

1. Overlap with simulation 3 (and naturally also 1, 4 and 7). This might be an indication that the simulation setups in 2 and 5 are not valid either due to bad spatial resolution, self-interactions or interactions with the opposite wall.
 2. $\Delta\varepsilon$ smaller than for simulation 3, but follows a similar pattern. In this scenario, one can interpret discrepancy to be related to inter-kink forces unaccounted for in the thin-wall approximation.
 3. $\Delta\varepsilon$ larger than for, or otherwise different from, simulation 3. This would be unfortunate and unpredicted.
- For fun, we could run a simulation were we let $\kappa > 0$, to get an idea of the impact having non-degenerate vacua.

7.3 Limitations and possibilities

We have analysed the results and discussed possible methods of verification and complementary analyses. Now, let us review the mathematical framework as it stands, in order to get an idea of the applicability. We consider three steps that are not completely independent, but describe a certain order of things.

Step one: Choose a background spacetime, particularly a conformally flat four-dimensional manifold, with conformal factor $a \propto \tau^\alpha$, where $\tau = x^0$ is the conformal time. **Prototype:** Set $\alpha = 2$ to get matter domination.

Step two: Invoke a (first-order) phase transition at $\tau = \tau_*$, and a scalar boson ϕ responsible for said phase transition. Choose a scalar-field or scalar-tensor theory with a suitable symmetry-breaking (effective) potential $V_{\text{eff}}(\phi)$. **Prototype:** Specify that ϕ is the (a)symmetron field, and consider $\kappa = 0$ (symmetron).

Step three: Consider a topological defect that is the product of the aforementioned symmetry break. The defect with vanishing thickness possess dynamics derived from the Nambu–Goto action. Add a perturbation to the wall normal coordinate. We find the TT-part of the corresponding stress–energy tensor and consider this as a source of gravitational waves. **Prototype:** We consider the domain wall scenario, specifically a planar wall. The equation of motion for this perturbation is expended into eigenvalues and solved thereafter. We use this as input to the Nambu–Goto SE tensor, which in turn source tensor perturbations.

For this to be of any use in the quest for analytical estimations of gravitational waves that we discussed in the introduction, there has to be a certain level of analytical solvability for the resulting equations. In our prototype, we got pure analytical expressions up to the defect’s SE tensor in Fourier space. We need therefore only one numerical integration to compute the Fourier-space tensor perturbations for our prototype, which is quite neat.

7.3.1 Improvements

For the convenience of the reader, we present a short discussion of possible paths of generalisation of our approach to deal with more diverse physical systems.

Generalisation

With the above elaboration, we comprise the steps in the following “hierarchy”:

1. Background: four-dimensional spacetime
 - (a) Metric $g_{\mu\nu} = a^2(\tau)\eta_{\mu\nu}$
 - (b) Scale factor $a \propto \tau^\alpha$
 - (c) Matter domination, i.e. $\alpha = 2$
2. Phase transition: Scalar-field theory
 - (a) Asymmetron potential
 - (b) Symmetron potential
3. Topological defect: vanishing thickness
 - (a) Domain wall of vanishing thickness
 - (b) Planar wall
 - (c) Wall position trivial, consider small perturbation to wall normal coordinate
 - (d) Choose $\epsilon = \varepsilon(\tau) \sin(py)$

Generalisation from Item 1c to 1b should be uncomplicated. Considering N spatial dimensions is straight-forward, at least if the topological defect is of codimension one (with $D = N - 1$ spatial dimensions).

It would have been interesting to study the effect of non-degenerate vacua, e.g. the asymmetron (Item 2b to 2a). Our symmetron results suggest that minor changes in ϕ_\pm —the limits of the integral on the surface tension—do not drastically alter the overall behaviour of the perturbation on the wall. One can imagine that a similar expression for σ would hold for the asymmetron as well. Then there is just the matter of a non-zero vacuum energy difference $v = v_+ - v_-$, but this will also generally be time-dependent, $v = V(\phi_+) - V(\phi_-)$. In Minkowski spacetime and the limit where σ and v are constants, the solution to the equation of motion corresponding to our setup is the hyperbola [26], and we should expect the solution in the conformally related flat, FLRW ambient spacetime to inhabit similar features.

We mention that to solve the equation of motion for the (unperturbed) wall normal coordinate would remove the restriction that $\varepsilon_* \ll \tau_*$ (Item 3c to 3a). We address Item 3d below.

Different wall perturbation

As our working example, we chose the simplest solution to the equation of motion for the wall perturbation, namely $\epsilon = \varepsilon(\tau) \sin py$. This way, we kept the number of perturbation parameters to a minimum. This is naturally highly unlikely in real life. In Appendix C.4.2 we address the situation where the wall perturbation has more complex nature, and not simply the sinus from before. We saw that for only two eigenvalues, the xx -component of the stress–energy tensor becomes an infinite sum (Eq. (C.34)). This result is regrettable, but not necessarily catastrophic. It is perhaps possible to make use of some identities to simplify I_s , such Eq. (A.12), but time limitations make us have to leave this for now. To get the full picture, one would have to consider I_a as well, and keep in mind that the TT-projection we did before (Section 4.4.2) was a result of the single Dirac delta, which gave $I_a \propto I_s$ (Eq. (C.24b)). If proven that this blows up, there is reason to believe that the simplified analysis (Appendix C.3.1) does not hold either.

Now, we have performed the same naive operation as in Appendix C.3 where we extract a summation from an integral, without necessarily fulfilling the criteria for the commutation of these operators. Contributing factor to this confusion might have to do with differences to how one should interpret distributions versus functions, but these technicalities lie beyond the scope of this thesis.

7.4 Open questions

What it means for the gravitational waves to have any other perturbation $\epsilon = \epsilon(\tau) \sin(py + \varphi)$ remains unclear. A starting point for such an analysis was provided in Appendix C.4.2.

Varying symmetron parameters, or scalar-field theory as such, was the original wish, but other analyses was prioritised. Exactly how the gravitational waves can constrain the symmetron model is not discussed in this thesis.

We have seen how the time-dependence of the surface tension affects the dynamics of the wall. After some time, when the derivative of the surface tension goes to zero, the equation of motion is Eq. (4.23), with initial conditions from the first part of the evolution. The gravitational-wave dynamics are a little more intricate, and we have not studied the impact of letting σ vary with time. If it should turn out that this initial evolution of ϵ does not really affect the gravitational-wave signature, then maybe using time-dependent σ is an unnecessary complication. We could then adjust the initial conditions in Eq. (4.42) and use the simpler solution $\epsilon(s) = s^{-5/2} Z_{-5/2}(\omega s)$, where the constants are determined after evaluating ϵ^{NG} at some time point $s \gtrsim s_{\text{sow}}$ (see Section 4.3.1).

In summary, we have seen that there are still many paths to continue our work, in particular better understanding the gravitational radiation, which might help to establish at last a direct connection between symmetron domain walls and emitted gravitational waves.

Summary

Chapter 8

Conclusion and Outlook

We propose a semi-analytical formula for gravitational waves from two-dimensional topological defects in an FLRW universe, using differential geometry and classical field theory. To this end, we study the Nambu–Goto dynamics of planar domain walls, and solve analytically the equation of motion for domain walls *during* a symmetron phase transition in a matter-dominated universe. We have not found this solution in other literature. We find that the evolution of this solution, ε^{NG} , scales as the initial amplitude ε_* , and is not dependent on symmetron parameters. The damping in the equation of motion is determined by the *model* of phase transition, which in our case is the described symmetron effective potential. Model- and parameter-dependence can still be probed by gravitational waves from this phenomenon.

We have performed a number of periodic-box simulations to test this framework. Flat domain walls separated by $\mathfrak{D} = L_{\#}/2$, where $L_{\#}$ is the periodic length on the 3-torus, are created in a matter-dominated FLRW universe at initial scale factor $a_* = 0.33$. Between the eight experiments in Table 5.1 (0–7), we vary box side length $L_{\#}$ (4), number of lattice points $N_{\#}$ (3, 5), initial redshift \mathfrak{z}_i (4, 7), asymptotic wall width δ_{∞} (6),¹ initial perturbation amplitude $\varepsilon_*/L_{\#}$ (0, 2, 5) and perturbation scale $p/k_{\#}$ (0, 5).² In the following, results from simulation 6 are discarded (see Appendix D.1 for details). We also exclude simulation 0, as the comparison is trivial.

The evolution of the wall displacement field resulting from simulations is dependent on the initial amplitude ε_* , which refutes the thin-wall prediction (provided $\varepsilon_* \ll \tau_*$). The difference ($\Delta\varepsilon = |\varepsilon^{\text{NG}} - \varepsilon^{\phi}|$) between simulated wall position ε^{ϕ} and theoretical prediction ε^{NG} is maximally $(8 \pm 3)\%$ of the initial amplitude ε_* , and the average offset is $(16 \pm 5)\%$. Between simulations 1, 3–5 and 7, which all obey $\varepsilon_* < \mathfrak{D}/5 = 0.1L_{\#}$, the corresponding measures read $\max(\Delta\varepsilon) \in [13 \pm 2]\varepsilon_*$ and $\langle \Delta\varepsilon \rangle \in [7 \pm 1]\varepsilon_*$, respectively.

We present only qualitative comparative analyses on the subject of spin-2 perturbations. As such, validations of the gravitational-wave calculations are inconclusive. Toy-model simulation results show patterns in the gravitational signature that are directly connected to the nature of the wall displacement field, but the exact relations are unclear. The error $\Delta\varepsilon$ propagating from the difference in wall positions is significant for the gravitational-wave modes, and we therefore use the simulated wall position as input to the formula Eq. (5.19) for the comparison.

We know that stochastic scalar-field fluctuations can themselves source gravitational waves [36], and we can isolate the defect-sourced waves by minimising this effect. We present a protocol that tweaks the symmetron initial conditions to our advantage and gives more parameter flexibility in deterministic toy-model simulations.

¹Which is to say we vary symmetron mass scale μ , or Compton wavelength L_C .

²Scale p is irrelevant in simulation 0 as $\varepsilon_* = 0$.

The results overall are intriguing, and show promise of future analytical estimations of gravitational waves from topological defects, which is the main motivation for this thesis [52]. The time-varying surface tension is effectively an additional damping in the equation of motion for the wall displacement field, and during a symmetron phase transition, there exist explicit solutions to this equation for idealised universes. Completing the framework with novel comparative analyses—both qualitative and quantitative—can potentially elucidate the dependence on symmetron parameters systematically. This would open a window of dynamical ranges and parameter spaces that simulations alone cannot encompass.

To summarise, we provide the necessary background concerning GR and topological defects. The general dynamics of topological defects are studied, and perturbative domain-wall dynamics in expanding spacetimes are explicitly solved. The analytical solution to domain-wall perturbations during a symmetron phase transition is, to the best of our knowledge, not found in other literature. This solution is put in context with the full symmetry-breaking field-theory, and evaluated in simulations using `AsGRD`. We perform comparative analyses of the symmetron field, wall position and gravitational waves in the thin-wall theory and in full-theory simulations. From our results, one can argue that the Nambu–Goto framework provides valuable analytical insights to domain-wall dynamics also when the surface tension is time-dependent. We have laid a solid foundation for complementary simulations with `AsGRD` using tweaked symmetron initial conditions and continued gravitational-wave analysis.

A substantial amount of work remains if we ever want to compare this to actual gravitational-wave observations. We have not investigated the particular implications for future experiments in this thesis, but other literature [17, 23, 32, 33, 44, 46] support the hypothesis that domain wall signatures can be probed and constrained.

Bibliography

- [1] Abbott, B. P., Abbott, R., Abbott, T. D., et al. 2016, Physical Review Letters, 116, 061102
- [2] Adamek, J., Daverio, D., Durrer, R., & Kunz, M. 2016, Nature Physics, 12, 346
- [3] Adamek, J., Daverio, D., Durrer, R., & Kunz, M. 2016, Journal of Cosmology and Astroparticle Physics, 2016, 053
- [4] Afzal, A., Agazie, G., Anumarlapudi, A., et al. 2023, The Astrophysical Journal, 951, L11
- [5] Agazie, G., Anumarlapudi, A., Archibald, A. M., et al. 2023, The Astrophysical Journal, 951, L8
- [6] Amr, M. 2019, Nuclear Physics B, 945, 114648
- [7] Babichev, E., Gorbunov, D., Ramazanov, S., Samanta, R., & Vikman, A. 2023, NANOGrav Spectral Index $\gamma=3$ from Melting Domain Walls
- [8] Blanco-Pillado, J. J., Jiménez-Aguilar, D., Queiruga, J. M., & Urrestilla, J. 2023, Journal of Cosmology and Astroparticle Physics, 2023, 011
- [9] Braden, J., Bond, J. R., & Mersini-Houghton, L. 2015, Journal of Cosmology and Astroparticle Physics, 2015, 048
- [10] Burrage, C., March, B., & Naik, A. P. 2024, Journal of Cosmology and Astroparticle Physics, 2024, 004
- [11] Carroll, S. M. 2019, Spacetime and Geometry: An Introduction to General Relativity (Cambridge University Press)
- [12] Chen, N., Li, T., & Wu, Y. 2020, The Gravitational Waves from the Collapsing Domain Walls in the Complex Singlet Model
- [13] Christiansen, Ø. 2024, Doctoral thesis
- [14] Christiansen, Ø., Adamek, J., Hassani, F., & Mota, D. F. 2024, Gravitational Waves from Dark Domain Walls
- [15] Christiansen, Ø., Hassani, F., Jalilvand, M., & Mota, D. F. 2023, Journal of Cosmology and Astroparticle Physics, 2023, 009
- [16] Christiansen, Ø., Hassani, F., & Mota, D. F. 2024, Astronomy and Astrophysics, 689, A6
- [17] Clements, K., Elder, B., Hackermueller, L., Fromhold, M., & Burrage, C. 2023, Detecting Dark Domain Walls

Bibliography

- [18] Cutting, D., Escartin, E. G., Hindmarsh, M., & Weir, D. J. 2021, Physical Review D, 103, 023531
- [19] Dąbrowski, M. P., Garecki, J., & Blaschke, D. B. 2009, Annalen der Physik, 521, 13
- [20] Daverio, D., Hindmarsh, M., & Bevis, N. 2016, Latfield2: A C++ Library for Classical Lattice Field Theory
- [21] Dodelson, S. & Schmidt, F. 2020, Modern Cosmology
- [22] Dufaux, J. F., Bergman, A., Felder, G. N., Kofman, L., & Uzan, J.-P. 2007, Physical Review D, 76, 123517
- [23] Ferreira, R. Z., Notari, A., Pujolàs, O., & Rompineve, F. 2023, Journal of Cosmology and Astroparticle Physics, 2023, 001
- [24] Feynman, R. P. 1995, Feynman Lectures on Gravitation (Reading, Mass: Addison-Wesley)
- [25] Fumeron, S. & Berche, B. 2023, European Physical Journal Special Topics, 232, 1813
- [26] Garriga, J. & Vilenkin, A. 1991, Physical Review D, 44, 1007
- [27] Gleiser, M. & Roberts, R. 1998, Physical Review Letters, 81, 5497
- [28] Guven, J. 1993, Physical Review D, 48, 5562
- [29] Hagala, R., Llinares, C., & Mota, D. F. 2017, Physical Review Letters, 118, 101301
- [30] Hinterbichler, K. & Khoury, J. 2010, Physical Review Letters, 104, 231301
- [31] Hinterbichler, K., Khoury, J., Levy, A., & Matas, A. 2011, Physical Review D, 84, 103521
- [32] Hiramatsu, T., Kawasaki, M., & Saikawa, K. 2010, Journal of Cosmology and Astroparticle Physics, 2010, 032
- [33] Hiramatsu, T., Kawasaki, M., & Saikawa, K. 2014, Journal of Cosmology and Astroparticle Physics, 2014, 031
- [34] Ishibashi, A. & Ishihara, H. 1999, Physical Review D, 60, 124016
- [35] Jokela, N., Kajantie, K., & Sarkkinen, M. 2022, Physical Review D, 106, 064022
- [36] Kawasaki, M. & Saikawa, K. 2011, Journal of Cosmology and Astroparticle Physics, 2011, 008
- [37] Kolb, E. W. 1990, Frontiers in Physics, Vol. 69, The Early Universe (Redwood City, Calif: Addison-Wesley)
- [38] Kosowsky, A., Turner, M. S., & Watkins, R. 1992, Physical Review D, 45, 4514
- [39] Lancaster, T. & Blundell, S. J. 2014, Quantum Field Theory for the Gifted Amateur, 1st edn. (Oxford: University Press)
- [40] Li, X.-F. 2023, Probing the High Temperature Symmetry Breaking with Gravitational Waves from Domain Walls
- [41] Llinares, C. & Pogosian, L. 2014, Physical Review D, 90, 124041

- [42] Maggiore, M. 2007, Gravitational Waves. Vol. 1: Theory and Experiments (Oxford University Press)
- [43] Maggiore, M. 2018, Gravitational Waves. Vol. 2: Astrophysics and Cosmology (Oxford University Press)
- [44] Nakayama, K., Takahashi, F., & Yokozaki, N. 2017, Physics Letters B, 770, 500
- [45] Paraskevas, E. A. & Perivolaropoulos, L. 2023, Universe, 9, 317
- [46] Paul, A., Mukhopadhyay, U., & Majumdar, D. 2021, Journal of High Energy Physics, 2021, 223
- [47] Perivolaropoulos, L. & Skara, F. 2022, Physical Review D, 106, 043528
- [48] Peskin, M. E. & Schroeder, D. V. 1995, An Introduction to Quantum Field Theory (Reading, USA: Addison-Wesley)
- [49] Peyravi, M., Riazi, N., & Lobo, F. S. N. 2017, Physical Review D, 95, 064047
- [50] Press, W. H., Ryden, B. S., & Spergel, D. N. 1989, The Astrophysical Journal, 347, 590
- [51] Ramazanov, S., Babichev, E., Gorbunov, D., & Vikman, A. 2022, Physical Review D, 105, 063530
- [52] Saikawa, K. 2017, Universe, 3, 40
- [53] The Sage Developers. 2023, SageMath, the Sage Mathematics Software System (Version 10.1)
- [54] Vachaspati, T. 2006, Kinks and Domain Walls: An Introduction to Classical and Quantum Solitons (Cambridge: Cambridge University Press)
- [55] Vilenkin, A. & Shellard, E. P. S. 1994, Cosmic Strings and Other Topological Defects

Bibliography

Appendices

Appendix A

Cylinder Functions

We will in the following define the first and second kinds of the (regular) Bessel functions, spherical Bessel functions and Riccati–Bessel functions, collectively denoted Z , z and R , respectively. The second kinds are also called the Neumann, spherical Neumann and Riccati–Neumann functions. Conventions are shown in Table A.1, and we use $\nu \in \mathbb{C}$ and $n \in \mathbb{Z}$ to denote the order.

Type	Combination	1st kind	2nd kind	i th kind
Bessel functions	Z_ν	J_ν	Y_ν	$Z_\nu^{(i)}(x)$
Spherical Bessel functions	z_n	j_n	y_n	$z_n^{(i)}(x) = \sqrt{\pi/(2x)} \cdot Z_{n+1/2}^{(i)}(x)$
Riccati–Bessel functions	R_n	S_n	C_n	$R_n^{(i)}(x) = -(-1)^i x \cdot z_n^{(i)}(x)$

Table A.1: Types of Bessel functions and conventions. Here, $\nu \in \mathbb{C}$ and $n \in \mathbb{Z}$ are constants, and $x \in \mathbb{C}$ is a variable. Linear combinations of the first and second kinds are denoted in the second column. Subscripts mean order, and parenthesised superscripts refer to kind.

The general solution to Bessel's differential equation ($' \equiv d/dx$)

$$x^2 y'' + xy' + (x^2 - \nu^2)y = 0 \quad \Rightarrow \quad y(x) = Z_\nu(x); \quad (\text{A.1})$$

is a linear combination of the (regular) ν th-order **Bessel** (first kind, J_ν) and **Neumann** (second kind, Y_ν) **functions**.

A convenient rewriting of this reads

$$x^2 y'' + x(1 - 2a)y' + [(bcx^c)^2 + (a^2 - \nu^2 c^2)]y = 0 \quad \Rightarrow \quad y(x) = x^a Z_\nu(bx^c). \quad (\text{A.2})$$

A variation of this is the spherical Bessel's equation. The general solution to the spherical Bessel's equation

$$x^2 y'' + 2xy' + (x^2 - n(n+1))y = 0 \quad \Rightarrow \quad y(x) = z_n(x); \quad (\text{A.3})$$

is a linear combination of the n th-order **spherical Bessel** (first kind, j_n) and **Neumann** (second kind, y_n) **functions**. Another special case is the general solution to

$$x^2 y'' + (x^2 - n(n+1))y = 0 \quad \Rightarrow \quad y(x) = R_n(x); \quad (\text{A.4})$$

a linear combination of the n th-order **Riccati–Bessel** (first kind, S_n) and **Riccati–Neumann** (second kind, C_n) **functions**.

A.1 Explicit formulas

A.1.1 Integer order

Bessel functions of integer order, the Z_n 's are given by

$$J_n(x) = \frac{1}{\pi} \int_0^\pi dy \cos(ny - x \sin y) \quad (\text{A.5a})$$

and

$$Y_n(x) = \lim_{\nu \rightarrow n} Y_\nu(x), \quad (\text{A.5b})$$

where

$$Y_\nu(x) = \frac{J_\nu(x) \cos \pi\nu - J_{-\nu}(x)}{\sin \pi\nu}; \quad \nu \notin \mathbb{Z}. \quad (\text{A.5c})$$

Furthermore,

$$Z_{-n}(x) = (-1)^n Z_n(x). \quad (\text{A.6})$$

A.1.2 Half-integer order

If $\nu = n + \frac{1}{2}$, we have $Z_{n+1/2}(x) = \sqrt{2x/\pi} z_n(x)$ where

$$j_n(x) = +x^n \left(-\frac{1}{x} \frac{d}{dx} \right)^n \left(\frac{\sin x}{x} \right), \quad (\text{A.7a})$$

$$y_n(x) = -x^n \left(-\frac{1}{x} \frac{d}{dx} \right)^n \left(\frac{\cos x}{x} \right), \quad (\text{A.7b})$$

are the spherical Bessel functions. Observe that

$$j_n(x) = (-1)^n y_{-(n+1)}(x), \quad (\text{A.8a})$$

$$y_n(x) = (-1)^{n+1} j_{-(n+1)}(x). \quad (\text{A.8b})$$

$$(\text{A.8c})$$

We also have the Riccati–Bessel functions

$$S_n(x) = +x j_n(x) = +\sqrt{\frac{\pi x}{2}} J_{n+1/2}(x), \quad (\text{A.9a})$$

$$C_n(x) = -x y_n(x) = -\sqrt{\frac{\pi x}{2}} Y_{n+1/2}(x). \quad (\text{A.9b})$$

Note that $S_0(x) = \sin x$ and $C_0(x) = \cos x$.

A.2 Properties

A.2.1 Some notable identities

We list some notable recurrence relations:

$$\frac{2\nu}{x} Z_\nu(x) = Z_{\nu-1}(x) + Z_{\nu+1}(x), \quad (\text{A.10a})$$

$$2Z'_\nu(x) = Z_{\nu-1}(x) - Z_{\nu+1}(x), \quad (\text{A.10b})$$

$$Z'_\nu(x) = Z_{\nu-1}(x) - \frac{\nu}{x} Z_\nu(x), \quad (\text{A.10c})$$

$$(x^\nu Z_\nu(x))' = x^\nu Z_{\nu-1}(x), \quad (\text{A.10d})$$

$$z'_n(x) = \frac{n}{x} z_n(x) - z_{n+1}(x). \quad (\text{A.10e})$$

The **Jacobi–Anger expansion** reads

$$e^{ia \sin bx} = \sum_{n=-\infty}^{\infty} J_n(a) e^{inbx}, \quad (\text{A.11a})$$

$$e^{ia \cos bx} = \sum_{n=-\infty}^{\infty} i^n J_n(a) e^{inbx}. \quad (\text{A.11b})$$

Bessel functions obey the relation

$$\sum_{m \in \mathbb{Z}} J_m(x) J_{n \mp m}(y) = J_n(\pm x + y). \quad (\text{A.12})$$

A.2.2 Asymptotic behaviour

For large real arguments $x \gg 1$, the Bessel functions approach

$$\lim_{x \rightarrow \infty} J_\nu(x) = \sqrt{\frac{2}{\pi x}} \cos(x - \nu\pi/2 - \pi/4), \quad (\text{A.13a})$$

$$\lim_{x \rightarrow \infty} Y_\nu(x) = \sqrt{\frac{2}{\pi x}} \sin(x - \nu\pi/2 - \pi/4). \quad (\text{A.13b})$$

Appendix A. Cylinder Functions

Appendix B

Stable Symmetron

We go through the steps leading to the solution of the asymptotic equation for the symmetron field Eq. (5.5) with the least possible oscillations around the asymptotic true minima χ_{\pm} . We follow Section 5.1.2, and recall that the normal picture in the expanding universe has

$$\chi_w(a, z - z_w) = \chi_{\pm} \tanh\left(\frac{a\chi_{\pm}(z - z_w)}{2L_c}\right). \quad (\text{B.1})$$

B.1 Idealised path

We rewrite Eq. (5.5) in terms of the time coordinate $\chi_+ = \sqrt{1 - v}$,

$$\frac{d^2\check{\chi}}{d\chi_+^2} - \frac{1}{\chi_+(1 - \chi_+^2)} \frac{d\check{\chi}}{d\chi_+} + m_*^2 \frac{\chi_+^2(\check{\chi}^2 - \chi_+^2)}{(1 - \chi_+^2)^3} \check{\chi} = 0, \quad (\text{B.2})$$

where

$$m_* = \frac{2\mu}{3\mathcal{H}_*(1 + \mathfrak{z}_*)} = \frac{\sqrt{2}a_*^{3/2}}{3\xi_*}. \quad (\text{B.3})$$

The idea is to use this solution as boundary conditions for χ :

$$\chi|_{z \rightarrow \pm\infty} = \pm\check{\chi} \quad \wedge \quad \dot{\chi}|_{z \rightarrow \pm\infty} = \pm\dot{\check{\chi}}. \quad (\text{B.4})$$

We solve in two regimes, each solution expanded around (I) $\chi_+ = 0$ and (II) $\chi_+ = 1$:

$$\check{\chi}^{(\text{I})} = \chi_* + \frac{C}{2}\chi_+^2 + \frac{C - \chi_*^3 m_*^2}{8}\chi_+^4, \quad (\text{B.5a})$$

$$\check{\chi}^{(\text{II})} = \chi_+ + \frac{8(3 - m_*^2)}{m_*^4}(\chi_+ - 1)^3 + \frac{1440 - 636m_*^2 + 41m_*^4}{2m_*^6}(\chi_+ - 1)^4. \quad (\text{B.5b})$$

We determine χ_* and C by matching these expressions at χ_+^{match} , i.e. solving

$$\begin{aligned} \check{\chi}^{(\text{I})}|_{\chi_+ = \chi_+^{\text{match}}} &= \check{\chi}^{(\text{II})}|_{\chi_+ = \chi_+^{\text{match}}} \\ \frac{d\check{\chi}^{(\text{I})}}{d\chi_+}|_{\chi_+ = \chi_+^{\text{match}}} &= \frac{d\check{\chi}^{(\text{II})}}{d\chi_+}|_{\chi_+ = \chi_+^{\text{match}}} \end{aligned} \quad (\text{B.6})$$

To find a suitable χ_+^{match} , we actually also match the solutions for the second derivative. The initial conditions best suited for the smallest oscillations possible are given by

$$\check{\chi} = \check{\chi}^{\text{ideal}} \equiv \begin{cases} \check{\chi}^{(\text{I})} & \text{if } \chi_+ \leq \chi_+^{\text{match}}, \\ \check{\chi}^{(\text{II})} & \text{if } \chi_+ \geq \chi_+^{\text{match}}. \end{cases} \quad (\text{B.7})$$

With the help of *SageMath* [53], we find these constants for any given m_* . Solving this for the fiducial symmetron parameters (Table 5.1, e.g. simulation 1) $m_* \simeq 268.36$, we get $\chi_* \simeq 0.09656$, $C \simeq 5.837$ and $\chi_+^{\text{match}} \simeq 0.2568$. This is demonstrated in Fig. B.1.

We update the domain wall profile

$$\chi_w = \check{\chi} \tanh\left(\frac{a\check{\chi}(z - z_w)}{2L_c}\right) \quad (\text{B.8})$$

and in turn the surface tension and thickness

$$\sigma_w = \sigma_\infty \frac{1}{2} (3\chi_+^2 - \check{\chi}^2) \check{\chi} \quad \text{and} \quad a\delta_w = \frac{\delta_\infty}{\check{\chi}}, \quad (\text{B.9})$$

where the latter is shown Appendix C.1.1. Note that both of these affect the thin-wall analysis in Chapter 4. We propose $\check{\chi} = \check{\chi}|_{\text{opt.}}$.

Optimal vs. idealised path

We distinguish between what we call the idealised path and the optimal path. The former, $\check{\chi}^{\text{ideal}}$, is given by Eq. (B.7), and the latter is the numerical solution to the asymptotic equation Eq. (5.5) with initial conditions $\check{\chi}^{\text{ideal}}$. They are generally marginally different, except at SSB, when $\chi_+ = 0$. Figure B.1 demonstrates this for simulations 1 and 7 in Table 5.1, that were initiated at different times.

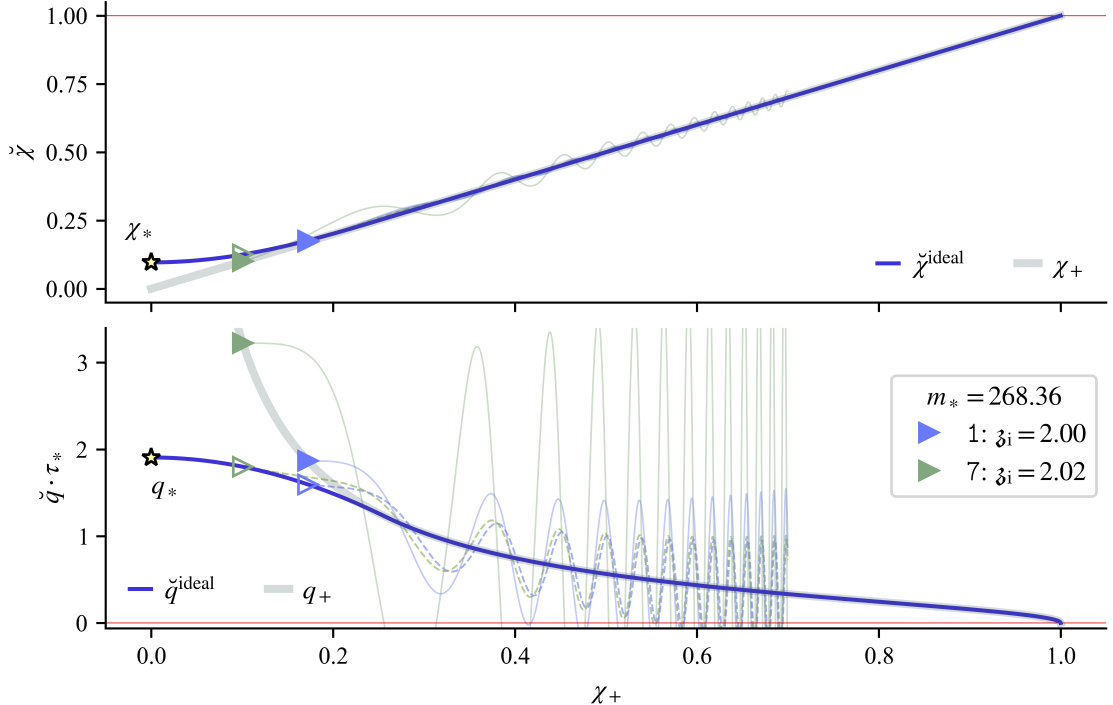


Figure B.1: The asymptotic symmetron field $\check{\chi}$ and the derivative $\check{q} = a^2 \dot{\check{\chi}}$ with different initial conditions. The horizontal axis is $\chi_+ = \sqrt{1 - v}$. The thin, solid lines show the solutions with initial conditions used in simulations (χ_+ and $q_+ = a^2 \dot{\check{\chi}}_+$) and the dashed lines show solutions with optimised initial conditions ($\check{\chi}^{\text{ideal}}$ and $\check{q}^{\text{ideal}} = a^2 \dot{\check{\chi}}^{\text{ideal}}$).

B.2 Field initialisation

At SSB $\check{\chi} = \chi_*$ and $\check{q} = q_* = a_*^2 3C/\tau_*$. To get the most precise initial configuration, we need to determine the full fields χ and q at $a = a_i \gtrsim a_*$. Note that $\dot{\epsilon} \neq 0$ in general. Define $u_w = a\check{\chi}(z - z_w)/2L_c$. Now,

$$\chi_{w\#} = \check{\chi} \tanh u_w, \quad (\text{B.10a})$$

$$a^{-2}\tau_* q_{w\#} = \check{\chi}' \tanh u_w + \check{\chi} u'_w \operatorname{sech}^2 u_w, \quad (\text{B.10b})$$

where

$$\check{\chi}' = \chi'_+ \frac{d\check{\chi}}{d\chi_+}, \quad (\text{B.10c})$$

$$2L_c u'_w = [a'\check{\chi} + a\check{\chi}'](z - z_w) - a\check{\chi} z'_w, \quad (\text{B.10d})$$

and $z'_w = \epsilon' \mathcal{E}$. Similar configuration, $\bar{\chi}_{w\#}$ and $\bar{q}_{w\#}$, is used for the unperturbed anti-wall by substituting $u_w, z_w \rightarrow \bar{u}_w, \bar{z}_w$ and swapping signs. Note that $\bar{z}'_w = 0$.

To assign values to χ and q , we can go through the lattice coordination-wise, “pick” the nearest wall and evaluate the aforementioned expressions at $\tau = \tau_i$. The product scheme (Eq. (3.4)) works as well.

Appendix B. Stable Symmetron

Appendix C

Symmetron Walls in Expanding Space-time

We present a gathered set of calculations for symmetron, planar domain walls in expanding spacetime. From Section 4.3 we have the FLRW spacetime \mathcal{M} with metric $g_{\mu\nu} = a^2 \eta_{\mu\nu}$ and Cartesian comoving coordinates $x^\mu = (\tau, \mathbf{x}) = (\tau, x, y, z)$. Embedded in this is a hypersurface Σ with induced metric γ_{ab} and coordinates ξ^a , $a = 0, 1, 2$. The hypersurface represents our domain wall, and the induced metric is

$$\gamma_{ab} = g_{\mu\nu} \partial_a X^\mu \partial_b X^\nu, \quad (\text{C.1})$$

with determinant

$$\gamma \equiv \det(\gamma_{ab}) = \tilde{\epsilon}^{abc} \gamma_{a0} \gamma_{b1} \gamma_{c2}, \quad (\text{C.2})$$

where $\tilde{\epsilon}$ is the Levi-Civita symbol (Eq. (7)), giving $\sqrt{-g} \sim a \sqrt{-\gamma}$. Additionally, we define $\hat{\gamma}_{ab} \equiv a^{-2} \gamma_{ab}$, such that $\gamma = a^6 \hat{\gamma}$.

Consider the covariant action, proportional to the area swept by the worldsheet,

$$S = \int_{\mathcal{M}} d^4x \sqrt{-g} \hat{\mathcal{L}}|_{\text{wall}} = \underbrace{\int_{\partial\mathcal{M}} dx_\perp a T_0^0}_{-\sigma} \int_{\Sigma} d^3\xi \sqrt{-\gamma} = -\sigma \int d^3\xi a^3 \sqrt{\hat{\gamma}}, \quad (\text{C.3})$$

where x_\perp represents the comoving coordinate perpendicular to Σ . We choose $\xi^a = (\tau, x, y)$ and let $z = z_w = z_0 + \epsilon(\xi^a)$ describe the position of the wall, where z_0 is a constant and ϵ is a linear perturbation.

We use the symmetron effective potential

$$V_{\text{eff}}(\phi = \phi_\infty \chi) = \phi_\infty^4 \cdot \frac{\lambda}{4} \chi^2 [\chi^2 - 2\chi_+^2], \quad (\text{C.4})$$

where $\chi_+ = \sqrt{1 - v}$ and $\phi_\infty = \mu / \sqrt{\lambda}$.

C.1 Surface tension

We identified the surface tension σ in Eq. (C.3), resulting in $\sigma = a \int_{\mathbb{R}} dz \rho(z)$. We use the quintessence action (Eq. (3.8)) to find [41]

$$\rho = \frac{1}{2a^2} (\dot{\phi}^2 - (\nabla\phi)^2) - V(\phi), \quad (\text{C.5})$$

and use this as an estimate for the energy contained in the wall. In the quasi-static limit, we find

$$\sigma_w = \frac{\phi_\infty^2}{2} a \int_{-\infty}^{\infty} dz \left\{ \frac{(\nabla \chi_w)^2}{a^2} + \frac{\mu^2}{4} (\chi_w^4 - \chi_+^4 - 2(\chi_w^2 - \chi_+^2)) \right\}, \quad (C.6)$$

where χ_w is given by Eq. (5.3). The resulting surface energy density is

$$\sigma_w = \frac{2\sqrt{2}\mu^3}{3\lambda} \chi_+^3. \quad (C.7)$$

Note that this is the same in both the Jordan and Einstein frame, as $A^{-4}(\phi) = 1$ [41].

Christiansen et al. [14] states that the surface tension of a thin domain wall is

$$\sigma_w \simeq \int_{\phi_-}^{\phi_+} d\phi \sqrt{2V_{\text{eff}}(\phi) - 2V_{\text{eff}}(\phi_\pm)}, \quad (C.8)$$

which for the effective symmetron potential Eq. (C.4) reduces to

$$\sigma_w \simeq \sqrt{\frac{\lambda}{2}} \int_{\phi_-}^{\phi_+} d\phi (\phi_+^2 - \phi^2) = \frac{4}{3} \sqrt{\frac{\lambda}{2}} \phi_+^3, \quad (C.9)$$

where $\phi_\pm = \pm\phi_\infty \sqrt{1-\nu}$. We see that Eqs. (C.7) and (C.9) are identical.

C.1.1 Adjusting the limits

If the asymptotic scalar field values are not tracking ϕ_\pm well, as the situation in Appendix B, we approximate the surface tension by Eq. (C.8) with the substitution $\phi_\pm \rightarrow \pm\check{\phi} = \pm\phi_\infty\check{\chi}$, i.e.

$$\sigma_w \simeq \sqrt{\frac{\lambda}{2}} \int_{-\check{\phi}}^{\check{\phi}} d\phi (\phi_+^2 - \phi^2) = \frac{\sigma_\infty}{2} (3\chi_+^2 - \check{\chi}^2)\check{\chi}, \quad (C.10)$$

where $\sigma_\infty = 2\mu^3\sqrt{2}/(3\lambda)$.

C.2 Wall dynamics

As in Section 4.2, we vary the Nambu–Goto action (Eqs. (4.19) and (C.3)), only now we include σ inside the integral: $S_{\text{NG}} = -\int_\Sigma d^3\xi \sqrt{-\gamma} \sigma$. We use $\hat{\gamma}_{ab} = a^{-2}\gamma_{ab}$ and find that the determinant is given by

$$\sqrt{-\hat{\gamma}} = \sqrt{1 + \eta_{ab}\partial^a\epsilon\partial_b\epsilon} = 1 + \frac{1}{2}\eta_{ab}\partial^a\epsilon\partial_b\epsilon + \mathcal{O}(\epsilon^3), \quad (C.11)$$

where ϵ is the wall displacement variable. We vary the action with respect to small changes in ϵ , giving

$$\begin{aligned} -\frac{\delta S_{\text{NG}}}{\delta \epsilon} \delta\epsilon &= \int_\Sigma d^3\xi \beta^3 \frac{1}{2} [\eta_{ab}\partial^a\epsilon\partial_b(\delta\epsilon)] \cdot 2 \\ &= \int d^3\xi [-\beta^3 \eta_{ab}\partial^a\partial_b\epsilon + \beta^3 3(\partial_0\beta/\beta)\partial_0\epsilon] \delta\epsilon, \end{aligned} \quad (C.12)$$

where $\beta^3 \equiv \sigma a^3$. In the last line, we used $\partial_a\epsilon\partial_a(\delta\epsilon) = \partial_a(\partial_a\epsilon \cdot \delta\epsilon) - \partial_a\partial_a\epsilon \cdot \delta\epsilon$, where the under-bar signifies that it is not a summation, and cancelled vanishing surface terms. We get

$$\partial_\tau^2\epsilon + 3(\partial_\tau\beta/\beta)\partial_\tau\epsilon - (\partial_x^2 + \partial_y^2)\epsilon = 0. \quad (C.13)$$

C.2.1 Full solution

In matter-dominated universe, Eq. (C.13) has solutions that are a superposition of $\varepsilon(\tau)\mathcal{E}(x, y)$ where

$$\varepsilon'' + \left(\frac{6}{s} + \frac{9}{2s(s^6 - 1)} \right) \varepsilon' + \omega^2 \varepsilon = 0 \quad (\text{C.14})$$

and $\tau_*^2(\partial_x^2 + \partial_y^2)\mathcal{E} = -\omega^2$. In Section 4.3 we obtained a solution in two regimes, one of these in terms of coefficients $A(\omega)$ and $B(\omega)$. For reference, we give the coefficients A and B in Eq. (4.38), obtained by matching solutions at $s = s_{\text{sow}} = 1 + \omega^{-1}$.

First, we define

$$D \triangleq \sqrt{2/\pi} \left(\omega^9 + 4\omega^8 + 6\omega^7 + 4\omega^6 + \omega^5 \right) \sqrt{\omega + 1} \\ \times \left[\frac{6\omega^5 + 15\omega^4 + 20\omega^3 + 15\omega^2 + 6\omega + 1}{\omega^6} \right]^{(1/4)}. \quad (\text{C.15a})$$

With

$$P_1 \triangleq 336\omega^9 + 1608\omega^8 + 1051\omega^7 - 6407\omega^6 - 17850\omega^5 \\ - 22050\omega^4 - 15162\omega^3 - 5766\omega^2 - 1036\omega - 46 \quad (\text{C.15b})$$

and

$$P_2 \triangleq 84\omega^9 + 1641\omega^8 + 7036\omega^7 + 12708\omega^6 + 11202\omega^5 \\ + 3120\omega^4 - 2490\omega^3 - 2292\omega^2 - 604\omega - 30, \quad (\text{C.15c})$$

we have

$$A(\omega) = -\frac{P_1 \cos(\omega + 1) - P_2 \sin(\omega + 1)}{D}, \quad (\text{C.15d})$$

$$B(\omega) = -\frac{P_2 \cos(\omega + 1) + P_1 \sin(\omega + 1)}{D}. \quad (\text{C.15e})$$

Now, Eq. (4.40) with Eq. (C.15) gives a completely analytical solution to Eq. (4.32).

C.3 Stress–energy tensor

The variation of Eq. (C.3) gives Eq. (4.15), for which we require

$$\frac{\delta \sqrt{-\gamma}}{\delta g_{\mu\nu}} = \frac{-1}{2\sqrt{-\gamma}} \frac{\delta \gamma}{\delta g_{\mu\nu}} = \frac{-a^4}{2\sqrt{-\gamma}} \frac{\delta \hat{\gamma}}{\delta \eta_{\mu\nu}}. \quad (\text{C.16})$$

To leading order in ϵ , we get

$$\frac{\delta \hat{\gamma}}{\delta \eta_{ab}} = -\eta^{ab}, \quad \frac{\delta \hat{\gamma}}{\delta \eta_{a3}} = -\partial^a \epsilon, \quad \frac{\delta \hat{\gamma}}{\delta \eta_{33}} = 0. \quad (\text{C.17})$$

Inserted into Eq. (4.15), we get $W^{\mu\nu} = T^{\mu\nu}|_{\text{NG}} + \mathcal{O}(\epsilon^2)$, i.e.

$$W^{\mu\nu}(\tau, x) = \frac{\sigma \delta(z - z_w)}{a^3} \frac{\delta \hat{\gamma}}{\delta \eta_{\mu\nu}}. \quad (\text{C.18})$$

Note that this holds for any first-order perturbation $\epsilon(\tau, x, y)$.

C.3.1 Fourier-space SE tensor

We let $\epsilon = \epsilon(\tau, y)$. Following Section 4.4.2, we look at Eq. (4.46) for $\mathcal{E}(y) = \sin py$ in $\epsilon = \epsilon(\tau)\mathcal{E}(y)$. The trick is to identify the Jacobi–Anger expansion, Eq. (A.13a),

$$f(x) \triangleq e^{ia \sin bx} = \sum_{n=-\infty}^{\infty} J_n(a) e^{inbx}. \quad (\text{C.19})$$

We postulate that the Fourier transform $\tilde{f}(\omega) \triangleq \int dx \sum_n F_n(x; \omega)$ is

$$\begin{aligned} \tilde{f}(\omega) &= \sum_n J_n(a) \int dx e^{i(\omega+nb)x} \\ &= 2\pi \sum_n J_n(a) \delta(\omega + nb). \end{aligned} \quad (\text{C.20})$$

We assumed that the integration and summation operators commute, which is known to be true for $\int dx \sum_n |F_n(x)| < \infty$ (Fubini’s theorem).¹ For

$$g(x) \triangleq cb \cos bx \cdot f(x) = \frac{1}{2} cb (e^{ibx} + e^{-ibx}) f(x), \quad (\text{C.21})$$

we find:

$$\begin{aligned} \tilde{g}(\omega) &= \frac{cb}{2} \sum_n J_n(a) \int dx [e^{i(\omega+(n+1)b)x} + e^{i(\omega+(n-1)b)x}] \\ &= \pi cb \sum_n [J_{n+1}(a) + J_{n-1}(a)] \delta(\omega + nb) \\ &= \frac{2\pi cb}{a} \sum_n n J_n(a) \delta(\omega + nb), \end{aligned} \quad (\text{C.22})$$

where in the last line we use Eq. (A.10a).

The non-vanishing SE-tensor components in Eq. (4.45) read

$$\begin{aligned} \tilde{W}_{ab} &= -a\sigma_w \eta_{ab} \cdot 2\pi \delta(k_x) \mathcal{D}_w I_s, \\ \tilde{W}_{iz} &= -a\sigma_w \delta_{iy} \cdot 2\pi \delta(k_x) \mathcal{D}_w I_a, \end{aligned} \quad (\text{C.23})$$

where the expressions in Eq. (4.46) are

$$I_s = 2\pi \sum_n J_n(k_z \epsilon) \delta(k_y + np), \quad (\text{C.24a})$$

$$I_a = 2\pi \frac{p}{k_z} \sum_n n J_n(k_z \epsilon) \delta(k_y + np) = -\frac{k_y}{k_z} I_s. \quad (\text{C.24b})$$

C.3.2 Spin-2 projection

We consider a symmetric 3×3 tensor S_{ij} with momentum $\mathbf{k} = (0, n_2, n_3)k$. Projected onto the TT gauge, the 11-component reads

$$S_{11}^{\text{TT}} = \Lambda_{11}^{ij} S_{ij} = \frac{1}{2} [S_{11} + 2n_2 n_3 S_{23} - n_3^2 S_{22} - n_2^2 S_{33}], \quad (\text{C.25})$$

¹It is not obvious that this holds, on the contrary; $\int dx \sum_n |F_n(x)| = \sum_n |J_n(a)| \int dx \not< \infty$. Still, Mathematica proposes the same solution to this problem, and we need to keep in mind that we are working with distributions and not functions.

where we used the projector in Eq. (10) and $n_2^2 + n_3^2 = 1$. We find that the linear polarisation basis is defined through the polarisation tensors

$$e_{ij}^+ = \begin{pmatrix} 1 & 0 & 0 \\ 0 & -n_3^2 & n_2 n_3 \\ 0 & n_2 n_3 & -n_2^2 \end{pmatrix}, \quad e_{ij}^\times = \begin{pmatrix} 0 & n_3 & -n_2 \\ -n_3 & 0 & 0 \\ n_2 & 0 & 0 \end{pmatrix}, \quad (\text{C.26})$$

such that $S_{ij}^{\text{TT}} = \sum_{P=+, \times} S_P e_{ij}^P$. This gives $S_+ = S_{11}^{\text{TT}}$.

Following Section 4.4, we have $\tilde{W}_{11} = \tilde{W}_{22}$ for the SE tensor in Eq. (C.23), which by using Eq. (C.25) yields

$$\tilde{W}_+ = \frac{1}{2} [n_2^2 \tilde{W}_{11} + 2n_2 n_3 \tilde{W}_{23}] \quad (\text{C.27})$$

With Eq. (C.24) we get the plus-polarised SE tensor

$$\tilde{W}_+ = -\frac{n_2^2}{2} \tilde{W}_{11}. \quad (\text{C.28})$$

C.4 Stress–energy tensor: alternative scenarios

In this section, we consider the Fourier-transformed stress–energy tensor when $\epsilon = \epsilon(\tau, y)$, but not necessarily $\epsilon(\tau) \sin py$ as in Appendix C.3.1.

C.4.1 Cosine case

Consider $\epsilon = \epsilon(\tau) \cos py = \epsilon(\tau) \sin(py + \pi/2)$. We get the same result as in Appendix C.3.1, only with a prefactor i^ℓ where $\ell = k_y/p$. This prefactor can be seen from Eq. (A.11b).

C.4.2 General case

We take a look at a scenario in which the solution to Eq. (4.23) is

$$\epsilon = \sum_k \epsilon_k = \sum_k \varepsilon_k \sin(p_k y); \quad p_k = \pi k / L, \quad (\text{C.29})$$

where L is some length scale. We let a_k be weights such that $\sum_k |a_k| = \varepsilon_*$ and $\varepsilon_k = a_k \varepsilon(\tau; p_k) / \varepsilon(\tau_*; p_k)$, where $\varepsilon(\tau; p_k)$ solves Eq. (4.32) for $p = p_k$. Following Section 4.4.2, the xx -component of the stress–energy tensor goes as

$$\tilde{W}_{xx} \sim \delta(k_x) I_s = \delta(k_x) \int dy e^{ik_z \sum_k \epsilon_k} e^{ik_y y}. \quad (\text{C.30})$$

By the same argumentation as in Appendix C.3.1, we get

$$I_s = 2\pi \sum_{n_1} J_{n_1}(k_z \varepsilon_1) \sum_{n_2} J_{n_2}(k_z \varepsilon_2) \sum_{n_3} J_{n_3}(k_z \varepsilon_3) \cdots \times \delta(k_y + \pi[1n_1 + 2n_2 + 3n_3 + \dots] / L) \quad (\text{C.31})$$

where $n_k \in \mathbb{Z}$. We use the property $J_n(0) = \delta_{n0}$ to check that this reduces to Eq. (C.24a) when there is only one nonzero weight (e.g. $a_1 = \varepsilon_*$). More compactly, we can write the contribution as

$$I_s = 2\pi \sum_{n_1, n_2, n_3, \dots} J_{n_1}^1 J_{n_2}^2 J_{n_3}^3 \cdots \times \delta(k_y + p_1 \sum_k k n_k) \quad (\text{C.32})$$

where we defined $J_n^k \triangleq J_n(k_z \varepsilon_k)$.

Example. Now say a_1 and a_3 are the only non-zero weights. The expression becomes

$$\sum_{n_1, n_3} J_{n_1}^1 J_{n_3}^3 \times \delta(k_y + p_1[n_1 + 3n_3]). \quad (\text{C.33})$$

This means that for modes say $k_y = -10p_1$, the term contributes to the source with $J_{10}^1 J_0^3 + J_6^1 J_1^3 + J_4^1 J_2^3 + J_1^1 J_3^3 + J_{16}^1 J_{-2}^3 + \dots$, i.e. an infinite series of factors $J_{n_1}^1 J_{n_3}^3$ for combinations $n_1 + 3n_3 = 10$, $n_k \in \mathbb{Z}$. Thus,

$$I_s = 2\pi \delta(k_y + Np_1) \sum_{m \in \mathbb{Z}} J_{N-3m}^1 J_m^3; \quad N = n_1 + 3n_3 \quad (\text{C.34})$$

for this setup.

Appendix D

Miscellanea

D.1 Simulation 6

Simulation 6 is identical to simulation 1, except for a change in the scaled Compton wavelength from $\xi_* = 3.33 \times 10^{-4}$ to $\xi_* = 10^{-4}$ (see Table 5.1). The Compton wavelength now is $L_C = \xi_* / H_0 \approx 0.30 \text{ Mpc}/\text{h}$, way smaller than the spatial resolution $\Delta_\# \simeq 1.3 \text{ Mpc}/\text{h}$. Figure D.1

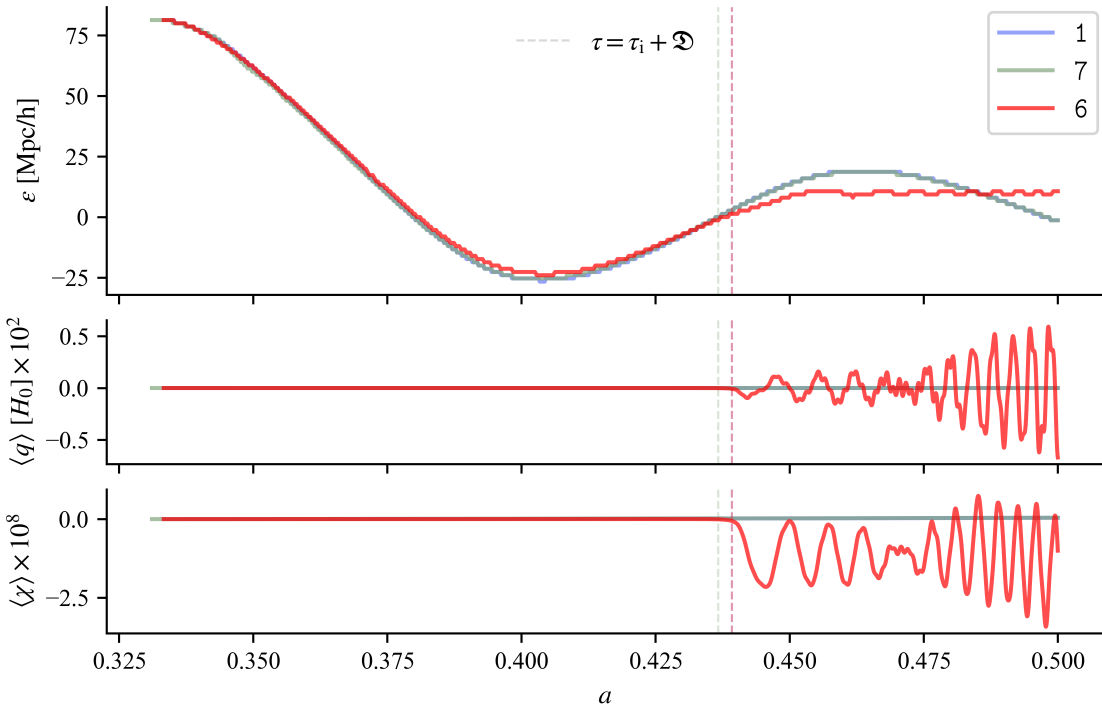


Figure D.1: Simulation results from simulations 1, 7 and 6, as functions of scale factor a . *Top panel:* The wall position ϵ^ϕ . *Bottom panels:* Spatially averaged values of the scalar fields χ and $q = a^2 \dot{\chi}$.

demonstrates how simulation 6 “fails” after a time period corresponding to $\Delta\tau/L_\# = 1/2$, i.e. conformal time equal half the box length. Results from simulations 1 and 7 are shown for comparison. Massless particles propagating in the z -direction will have travelled the distance corresponding to the separation between the walls between a_i and the vertical dashed line in Fig. D.1. The fact that $\langle q \rangle$ blow up here is most likely not a coincidence, but rather an unfortunate collision of information at any of the walls.

D.2 On the continuous/discrete Fourier-comparison

One thing we simply did not have the time or space to do, was to go into detail about how the gravitational waves were computed in AsGRD, and how this might affect the way we interpret the components of \tilde{h}_+ . In doing this analysis properly, we might have gained insight on the fact that $\tilde{h}_+^{\mathfrak{I}} \sim \tilde{h}_+^\phi$ and $\tilde{h}_+^{\mathfrak{R}} \not\sim \tilde{h}_+^\phi$, following the notation from Sections 5.2 and 5.3. On the other hand, we have [3]

$$\tilde{h}_{ij}^{\text{new}}(\tilde{\mathbf{n}}) = e^{-i\pi(\tilde{\mathbf{n}}_i + \tilde{\mathbf{n}}_j)/N_\#} \tilde{h}_{ij}(\tilde{\mathbf{n}}), \quad (\text{D.1})$$

which for $\tilde{\mathbf{n}}_1 = \mathbf{u} = 0$ gives

$$\tilde{h}_{11}^{\text{new}}(0, \mathbf{v}, \mathbf{w}) = \tilde{h}_{11}(0, \mathbf{v}, \mathbf{w}). \quad (\text{D.2})$$

We only considered this component in our analysis, so it should not be affected by this.

Still, definitions of lattice derivatives, momenta and TT-projection operator. We can test if

$$\tilde{h}_{ij}(\tilde{\mathbf{n}}) = \Lambda_{ij}^{kl}(\mathbf{k}k_\#) \tilde{h}_{kl}(\tilde{\mathbf{n}}), \quad (\text{D.3})$$

which is true for any TT-projected tensor. From Eq. (C.25) we have

$$\tilde{h}_{11}(0, \mathbf{v}, \mathbf{w}) = \frac{1}{2\tilde{\mathbf{n}}^2} [\tilde{\mathbf{n}}^2 \tilde{h}_{11} + 2\mathbf{v}\mathbf{w}\tilde{h}_{23} - \mathbf{w}^2\tilde{h}_{22} - \mathbf{v}^2\tilde{h}_{33}] (0, \mathbf{v}, \mathbf{w}), \quad \tilde{\mathbf{n}}^2 = \mathbf{v}^2 + \mathbf{w}^2; \quad (\text{D.4})$$

which naively implies

$$\begin{aligned} \tilde{h}_{11}^{\text{new}} &= \frac{1}{2\tilde{\mathbf{n}}^2} [\tilde{\mathbf{n}}^2 \tilde{h}_{11}^{\text{new}} + 2\mathbf{v}\mathbf{w}\tilde{h}_{23}^{\text{new}} - \mathbf{w}^2\tilde{h}_{22}^{\text{new}} - \mathbf{v}^2\tilde{h}_{33}^{\text{new}}] \\ &= \frac{1}{2\tilde{\mathbf{n}}^2} [\tilde{\mathbf{n}}^2 \tilde{h}_{11} + 2e^{-i\pi(\mathbf{v}+\mathbf{w})/N_\#} \mathbf{v}\mathbf{w}\tilde{h}_{23} - e^{-i\pi 2\mathbf{w}/N_\#} \mathbf{w}^2\tilde{h}_{22} - e^{-i\pi 2\mathbf{v}/N_\#} \mathbf{v}^2\tilde{h}_{33}^{\text{new}}] \end{aligned} \quad (\text{D.5})$$

for $\tilde{\mathbf{n}} = (0, \mathbf{v}, \mathbf{w})$. We leave this here.